Mass Transport in Nanoporous Materials: New Insights from Micro-Imaging by Interference Microscopy

Von der Fakultät für Physik und Geowissenschaften

der Universität Leipzig

genehmigte

DISSERTATION

zur Erlangung des akademischen Grades

doctor rerum naturalium

Dr. rer. nat.,

vorgelegt

von Diplomphysiker Tomas Binder,
geboren am 26. Januar 1984 in Großenhain.

Gutachter: Prof. Dr. Jörg Kärger, Universität Leipzig
Prof. Dr. Gero Vogl, Universität Wien

Tag der Verleihung: 14. Oktober 2013

Abstract

Binder, Tomas
Mass Transport in Nanoporous Materials:
New Insights from Micro-Imaging by Interference Microscopy

Universität Leipzig, Dissertation, 2013
91 pages, 125 references, 12 tables, 51 figures

This thesis presents the recent progress of diffusion measurements in nanoporous host systems by micro-imaging. Interference microscopy is applied as a powerful tool to record transient, intracrystalline concentration profiles of different sorbate species in the porous framework of two different zeolites, viz. ZSM-5 (MFI) and ZSM-58 (DDR). These profiles, yielding high temporal and spatial resolutions of about 10 s and 0.45 µm, follow the change of the refractive index of the host-guest system during uptake and release of certain guest molecules. With the thus accessible changes of concentration and particle fluxes, mass transport parameters, such as intracrystalline diffusivity and surface permeability, can be obtained by the use of the very fundamental equations on diffusion.

Additionally, in two examples of never before performed types of experiments, further insights into challenging fields of host-guest interactions are provided: The well known phase transition in MFI type zeolites covering high benzene loadings is investigated in a single crystal study, allowing to follow the change of the sorbate phase in great detail. Furthermore, in DDR zeolites, a new way of data analysis facilitates to study the uptake and release of binary mixtures. Here, from the two-dimension profiles obtained by interference microscopy, the local concentrations of the sorbate species could be retrieved by using the so-called *ideal adsorbed solution theory*.

Contents

Nomenclature

α	surface permeability (in sec. 3.2)
α	polarizability (in sec. 3.3)
α_n	n^{th} root of J_0 (in sec. 4.1)
A	surface area
c, θ	(intracrystalline) concentration, loading
$c_{\text{max}}, c_{\text{eq}}$	maximum or equilibrium concentration
c_{norm}	normalized concentration
c_{surf}	boundary concentration
d_p	pore diameter
D	diffusion coefficient
D_{T}	transport diffusivity
$\mathcal{D}$	self-diffusivity
$\boldsymbol{j}$	particle flux density
J_i	Bessel function of order i
k	factor of proportionality between Δc and $\Delta(\Delta\varphi)$
l	thickness of a thin surface layer
$L_{X,Y,Z}$	crystal length in (x, y, z) direction
λ	wave length
m	uptake
M_1	first statistical moment of molecular uptake
n	refractive index
N	particle number
φ	phase angle
$\Delta\varphi^{(L)}$	phase difference (after crystal thickness L)
$\Delta(\Delta\varphi)$	change of phase difference (in time)
p	pressure
r	distance from the crystal center or symmetry axis
R	(crystal or particle) radius
σ_C	critical molecular diameter
t	time
$t_{1/2}$	time of half-filled crystal
V	volume
x, y, z	spatial directions
X, Y, Z	crystal directions (in sec. 3.1)

1. Introduction

In the last decades, mass transport in nanoporous materials has been identified as the key point in numerous applications of chemical industry. The underlying process of particle fluxes under the confinement of a porous host system is the irregular and omnipresent motion of small particles, referred to as diffusion. Honoring the first, detailed description by Brown in 1828 [1], it is also called Brownian motion. Most remarkably, this observation, and as well the formulation of the fundamental diffusion equations for a certain concentration gradient by Fick in 1855 [2], were made long before the atomistic models, such as the Dalton hypothesis on atomic theory [3], were commonly accepted or experimentally proven.

The combination of both, erratic movement of small particles in equilibrium (Brown) and mass transport opposing the direction of a concentration gradient (Fick), was described via a thermodynamic approach by Einstein in 1905 in one of his famous seminal papers of this very year [4, 5]. Additionally, this correlation of the diffusion coefficient and the mean square displacement, was found by Smoluchowski in 1906 by following a different, kinetic approach of the interactions and collisions between particles [6].

With the rise of synthetic zeolites, for the first time synthesized by Barrer in 1948 [7], and the growing number of their applications in chemical processes, diffusion in micro-, meso- and macroporous materials increasingly attracted attention in industry and academia [8]. Correlated to the mass transport parameters, also material characterization regarding accessible surface areas or pore widths distributions was continuously in the focus of research, starting from the fundamental BET model on surface areas in 1938 [9]. Together with classical zeolites, various types of new, nanoporous materials are investigated in terms of adsorption properties [10, 11], among them porous glasses, metal-organic frameworks (MOFs) and periodic mesoporous organosilicas (PMOs).

However, considerations of diffusion are by far not limited to the movement of molecules in porous frameworks. The basic mathematical equations also apply in many other contexts, especially if there is a certain kind of gradient. This includes the migration of animals, men and ideas [12, 13], but also human travel and spreading of diseases [14, 15]. Even the circulation of bills around the US and the whole world can be followed [16], with their trajectories being remarkably similar to those of small particles, yet revealing length scales of hundreds or thousands of kilometers.

The requirements of measuring diffusion in much shorter distances, i.e. in the micrometer range, are certainly demanding. However, only microscopic techniques facilitate deeper insights into the elementary steps of mass transport in porous host systems and, thus, advance the understanding of these processes.

Especially precious are the so-called methods of micro-imaging, by which concentration profiles of sorbate molecules in zeolites or MOFs are obtained in high resolutions. They particularly include confocal fluorescence microscopy [17], IR microscopy [18, 19] and interference microscopy [20–22], the latter being in the center of this work.

After further introducing porous materials and their fields of application (sec. 2.1), diffusion under confinement (sec. 2.2) and methods of micro-imaging (sec. 2.3), six main topics are addressed within this thesis. Sec. 3, dealing with zeolite ZSM-5 of framework type MFI, is dedicated to the study of orientation-dependent guest diffusion (sec. 3.1), the nature of surface barriers (sec. 3.2) and the phase transition of benzene at high loadings (sec. 3.3). Investigations on zeolite ZSM-58 of framework type DDR are carried out regarding new ways of analyzing concentration profiles of cylindrical symmetry (sec. 4.1), a comparison of different small hydrocarbons and varying samples (sec. 4.2), and novel approaches to retrieve two-component concentration profiles for adsorption and desorption of binary mixtures (sec. 4.3).

The aim of this work, to gain new insights into mass transport phenomena in nanoporous materials by means of interference microscopy, has clearly only been made possible by the development of the device over the past few years and by the input of the messages of other techniques. Both are gratefully acknowledged.

2. Fundamentals of Experiment and Theory

The experimental and theoretical fundamentals of this PhD work concern the type and specific properties of the applied microporous material, namely *zeolites* [23], the omnipresent movement of particles referred to as *diffusion* [1], in general and particularly under the confinement by a porous matrix [8], and finally the experimental methods applied to study these processes, viz. *interference microscopy* (IFM) and *IR microscopy* (IRM). The following three subsections 2.1, 2.2 and 2.3 will address these topics briefly and provide references to the appropriate textbooks and publications. This shortening was chosen due to the intention of focusing on the authors own work presented in sections 3 and 4, namely the application of micro-imaging techniques to gain information on the adsorption and desorption behavior by recording and analyzing transient intracrystalline concentration profiles of high spatial and temporal resolution. However, as this work presents types of experiment never performed before, such as the spatially resolved observation of phase transitions in the benzene-MFI system in sec. 3.3 and the recording of species-dependent concentration profiles during mixture adsorption in sec. 4.3, at least a small background on the systems and measuring techniques is needed.

2.1. Porous Materials and Fields of Application

Porous materials considered in this work are crystalline or amorphous solids with a porous structure of either channels or a combination of larger cages connected by narrow windows. This porosity may be highly ordered or randomly distributed in a one-, two- or three-dimensional way. There is a broad variety of materials available matching this requirement, ranging from zeolites [23], porous glasses or active carbons to the recently developed metal-organic-frameworks (MOFs) [24]. The major interest on these porous solids is due to their tremendous (inner) surface leading to large adsorption capacities for gaseous species and high catalytic activities. In addition, one may observe size exclusion effects when the size of pores matches those of the molecules to be adsorbed.

Following these considerations, three major fields of application have developed in the last decades: catalysis [25], gas storage [26] and separation [27]. However, from the approximately 200 known framework types of zeolites [28] only less than ten found their way to large scale industrial application. In the case of MOFs this discrepancy is even larger as the combination of metal cluster and organic linkers allows numerous theoretically predicted or experimentally obtained structures, which unfortunately often reveal poor stability with respect to mechanical stress or severe working conditions like high temperatures and disturbing impurities. In addition, the cost effectiveness has to be taken into account when planning the upscaling from lab scale (grams) to pilot plant (kilograms) and commercial high throughput processes (tons). One of the most commonly used type of nanoporous material, *zeolite A*, is schematically shown in fig. 1.

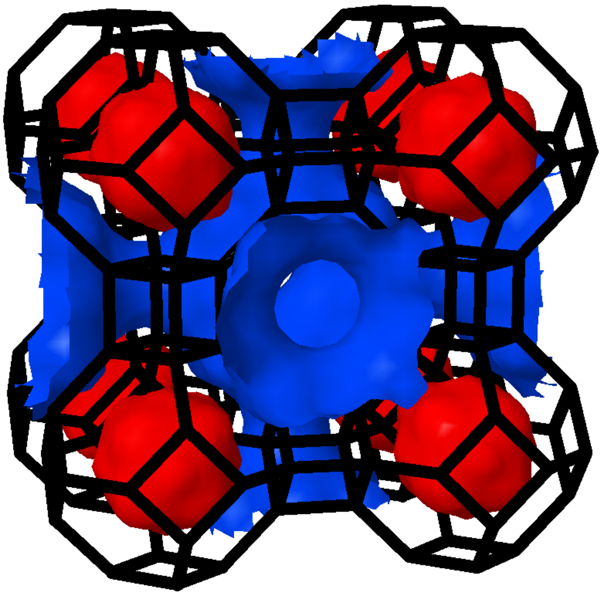

Figure 1: Structure of zeolite A (framework type LTA) with eight sodalite cages in red and the channels leading to the central alpha cage in blue.

While in the research group of Interface Physics at the Physics department of the University of Leipzig the whole variety of porous materials is covered, the present study focuses on the intracrystalline diffusion in two different framework types of zeolites, namely ZSM-5 and ZSM-58. In general, zeolites are highly ordered microporous crystals occurring both naturally and as the product of synthesis in either laboratory or industry. Their chemical composition comprises silicon, aluminum and oxygen, often with additional counter ions like Na^+, K^+, Ca^{2+} or Mg^{2+}. Depending on the desired purpose, the size of synthetic zeolite crystals ranges from less than one to several tens or hundreds micrometer. While the commercially available material, e.g. for catalysis, is shaped to pellets with or without the use of binder materials, fundamental research with respect to crystal properties and transport behavior of certain sorbate species is usually performed using pure powder or even single crystals. The latter is true for investigations by means of micro-imaging, which requires only very little sample material but a certain degree of crystal quality with respect to their optical properties and homogeneity of size and shape. The hot topic of interest is the intracrystalline diffusion of sorbate species, which may, in principle, also be investigated by pulsed field gradient nuclear magnetic resonance (PFG NMR) [29, 30], zero length column (ZLC) [31] or frequency response (FR) [32, 33]. However, direct insights into the intracrystalline concentration of those guest molecules and their variation with time is only made possible by the introduction of the micro-imaging techniques interference microscopy (IFM) and IR microscopy (IRM) in Leipzig within the last decade [19,34]. Like a magnifying glass, both methods, especially when applied complementary, provide never before seen insights into intracrystalline transport phenomena.

2.2. Diffusion under Confinement

These transport processes are a result of the omnipresent Brownian motion of small particles [1], referred to as diffusion. This irregular movement, in our case of small hydrocarbon molecules, occurs statistically distributed in all directions of the three-dimensional space due to the thermal energy of the material. The most fundamental equations describing diffusion were formulated by Adolf Fick more than 150 years ago [2]:

$$\boldsymbol{j}_x = -D\frac{\partial c}{\partial x} \tag{1}$$

$$\frac{\partial c}{\partial t} = \frac{\partial}{\partial x}\left(D\frac{\partial c}{\partial x}\right) = D\frac{\partial^2 c}{\partial x^2} \tag{2}$$

They state a certain concentration gradient $\frac{\partial c}{\partial x}$ of the species under study to result in a particle flux $\boldsymbol{j}_x$ trying to compensate this very gradient in eq. (1). As a factor of proportionality, the diffusion coefficient D is introduced. In the absence of catalytic conversion, mass conservation is implied, which then leads immediately to eq. (2) describing the change of concentration in time. The second equation results under the simplifying assumption that the diffusivity does not vary with varying concentration. In this case, the change of concentration with time is seen to be proportional to its second spatial derivative $\frac{\partial^2 c}{\partial x^2}$. Depending on the physical conditions under which the experiments are performed, one may specify the diffusion coefficient as D_T, the transport diffusivity, or $\mathcal{D}$, the self-diffusivity. The latter is applied to systems in equilibrium, where the concentration gradient in eq. (1) is only artificially introduced via certain labeling of the particles and the overall mass transport is zero. In non-equilibrium systems, as it is the case for adsorption and desorption processes, the factor of proportionality in the Fick's equations is the transport diffusivity D_T determining the kinetics of the mobile species during the mass transport to reach equilibrium concentration. For comparing self- and transport diffusivity when obtained by different techniques one may benefit from the convenient situation of very low concentration. In this case both diffusivities, D_T and $\mathcal{D}$, are found to coincide.

However, in the very case of diffusion under confinement by a non-ideal porous host system, deviations of the real structure from ideal crystalline structure have in addition to be considered. The thus resulting transport resistances are found and well known to occur - though often unattended - in many systems ranging from lab experiments to applications of industrial scale. These resistances or barriers one may find with varying strength and nature, e.g. as barriers of inner and outer surfaces or blocked pores in the bulk zeolite. However, even the opposite effect is reported when straight channels are unintentionally interconnected or cracks within the crystal serve as diffusion highways. Contrary to computer simulations of transport processes during adsorption and desorption, all experimental techniques provide an *apparent diffusivity* which is often found to be, in first approximation and assuming high crystal quality, the combined effect of fast intracrystalline diffusion D_{intra} and hindering surface barriers resulting from low surface permeabilities α. It is the very benefit of micro-imaging techniques as described in sec. 2.3 to gain information on both, D_{intra} and α.

molecule / zeolite	**(critical) diameter**
methane	$\sigma_C = 0.34\,\text{nm}$
ethylene	$\sigma_C = 0.35\,\text{nm}$
ethane	$\sigma_C = 0.37\,\text{nm}$
propylene	$\sigma_C = 0.43\,\text{nm}$
ZSM-5	$d_p = 0.45\,\text{nm}$
ZSM-58	$d_p = 0.37\,\text{nm}$

Table 1: Comparison of critical diameters σ_C of molecules applied in sec. 4 and pore widths d_p of the investigated zeolites. Critical molecular diameters are obtained from the diameter of the smallest cylinder circumscribing the molecules' most favorable equilibrium conformation (following ref. [35], an effective hydrogen diameter of 0.166 nm is assumed).

Another issue to be addressed is the question of pore widths and molecule sizes. It is clear that, as soon as the diameter of channels or windows approaches those of the species being adsorbed, strong effects of the molecular size on the diffusivity are expected. However, both pore diameter and molecule size should not be understood as rigid openings and solid spheres, respectively. Even though zeolite structures are considered not to be quite flexible (especially when compared to MOFs where this behavior can be much more explicit), the distances usually given in nanometers or angstrom are always obtained by using certain models in theoretical calculations or experimental data processing. By its very nature, however, atoms and molecules consist of dense cores and spacious shells of electrons with the latter being described in quantum mechanics by probability density functions. The question on where to set the cut off for determining molecule sizes is by far not trivial. Hence, we may expect measurable uptake even in cases where the molecule is not expected to fit into the porous host system while it is unquestionable that diffusion coefficients may cover a broad range over several orders of magnitude when the dimension of sorbate molecules approaches and exceeds those of the pores and channels. Varying literature data for the very same molecule sizes are the outcome of this issue [8, 36]. In the following sections of this work, the critical molecular diameter σ_C, i.e. the diameter of the smallest cylinder that can circumscribe the molecule in its most favorable equilibrium conformation using an effective hydrogen diameter of 0.166 nm [35] is used as one option among others [37]. A brief comparison of the thus derived molecule sizes with pore openings of the investigated zeolites is given by tab. 1.

2.3. Methods of Micro-Imaging: Interference and IR Microscopy

Resulting from the broad variety of scientific research areas, in which diffusion plays a key role to the processes under investigation, there exist as well numerous measuring techniques to access diffusivities in various systems. Profiling techniques make use of the fundamental equations of diffusion and mass transport, viz. Fick's first and second law as given by eqs. (1) and (2), to access diffusivities via the recording of concentration profiles. This has been demonstrated for both fluids [38, 39] and solids [40]. Furthermore, since the introduction of pulsed field gradient nuclear magnetic resonance (PFG NMR, [41, 42]), the probability distribution of displacements of guest molecules, referred to as *propagator*, has directly been accessible [43]. The thus derived imaging techniques of magnetic resonance imaging (MRI) and diffusion tensor imaging (DTI or diffusion MRI) have doubtlessly proven their importance in and strong benefits to medical applications.

Even though there is still a broad variety of experimental methods to address diffusivities of the host-guest system consisting of a rigid zeolite framework and a mobile gaseous species, the applicable options of obtaining intracrystalline concentration profiles are rather limited. Colleagues from Utrecht, the

Netherlands, impressively demonstrated the use of confocal fluorescence microscopy to record concentrations - even three-dimensionally - of certain fluorescent species [17]. This, however, yields insights into the various structure types of zeolite ZSM-5 rather than the mobility of smaller molecules. Unambiguously, only interference microscopy (IFM) and IR microscopy (IRM), referred to as methods of micro-imaging, can provide such information.

With IFM being in the center of the present work, only this technique is going to be described in detail. Complementary IR data are shown in sec. 4.3.4, where the single element detector is applied to study the uptake of two different species in a mixture. The possibility of recording spatially resolved IR profiles, i.e. 128 × 128 full IR spectra, is not exploited within this study. Presently, there are two other PhD works in preparation investigating, among other topics, the interplay of catalysis and diffusion during chemical reactions in nanoporous host systems by IR imaging [44, 45].

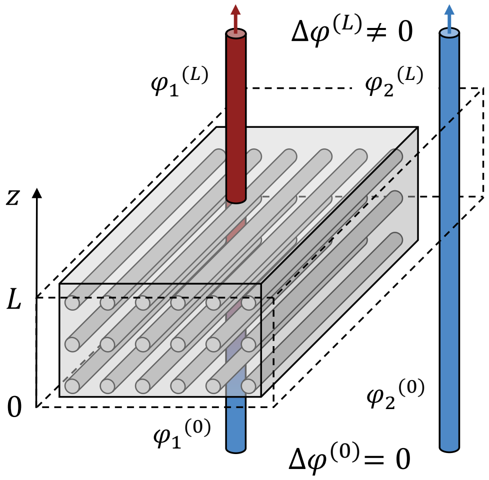

Figure 2: Appearance of a phase difference $\Delta\varphi$ between the two light beams discussed in fig. 3. The crystal under investigation (here: one-dimensional straight pores) clearly has a different refractive index n compared to that of the surrounding gas phase. Therefore, the initial agreement of $\varphi_1^{(0)}$ and $\varphi_2^{(0)}$ before the light beams pass the crystal of thickness L in z-direction is abolished leading afterwards to the previously mentioned phase difference $\Delta\varphi$. A subsequent phase shifter (not shown, see fig. 3) causes a tunable increase of the phase difference at the moment of superposition.

The experimental setup of interference microscopy, as introduced and modified within the last 15 years by Schemmert [20–22], Kortunov [46–48], Tzoulaki [49–51] and Hibbe [34, 52, 53], comprises the microscope itself, a *Jenamap p* *dyn* with an interferometer of the Mach-Zehnder type manufactured by Carl Zeiss GmbH, a CCD camera, currently a Photometrics *SenSys KAF 0400*, and the vacuum system providing either vacuum for desorption or constant gas phase pressure for adsorption. Both, microscope and camera, are connected to a commercial personal computer controlling the picture recording and microscope settings (phase shifter, see fig. 3). The sample, only several dozens or hundreds of zeolite single crystals, is placed in a plain optical cell under the microscope having the only opening connected to the vacuum system. A single crystal is then illuminated by monochromatic light with a wavelength λ of about 589 nm, with the light passing through the crystal and the surrounding gas phase as indicated in fig. 2.

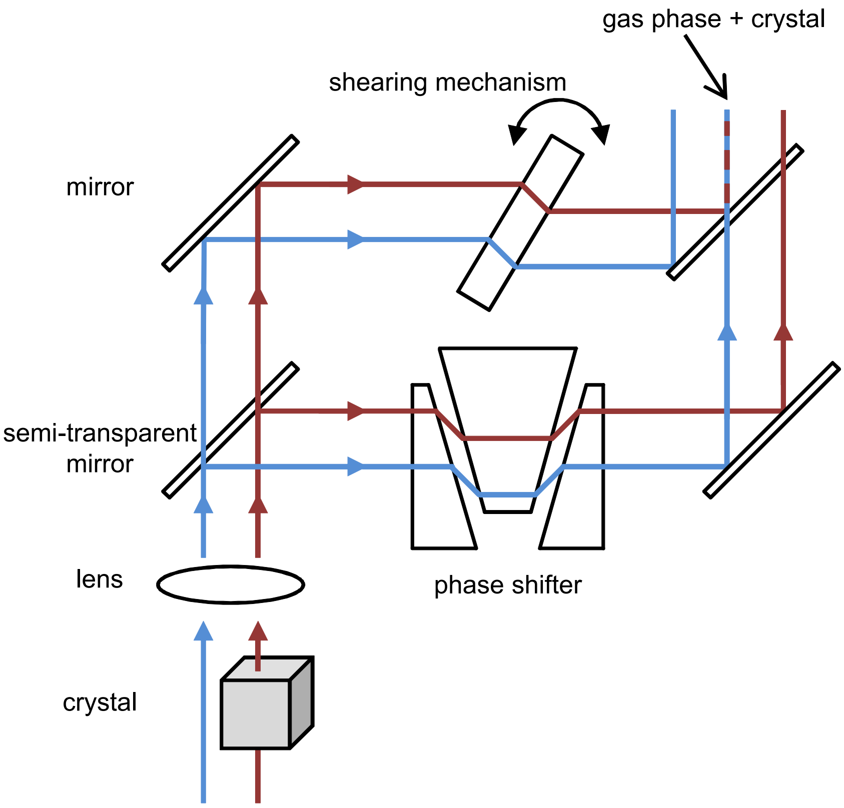

Figure 3: Interference optics and generation of the interference picture by superposition of one light beam passing the porous crystal (red) and one passing the surrounding gas phase (blue). The lateral shift of both beams (or images) is induced by a rotatable glass plate, referred to as shearing mechanism, while the phase shifter only changes the phase difference of both light beams (see fig. 2).

Regarding the phases of the two indicated beams, it is clear, that the difference of phase φ equals zero before entering the sample, but has changed to a certain phase difference $\Delta\varphi^{(L)}$ on leaving the sample. Even though this phase difference's absolute value remains unknown, its variation in time may be determined by analyzing the interference pattern created by both light beams in fig. 2. The superposition to create the interference image involves a shearing mechanism and phase shifter as shown in fig. 3, with the latter being controlled by the personal computer. Within a short period of time, in which the sorbate concentration should ideally not change in the whole crystal, five interference images at different positions of the phase shifter are recorded and used to calculate one profile of intracrystalline concentration. In fact, this calculation is not based on the attenuation of light intensity when passing through the crystal, but on the change of the previously introduced phase difference $\Delta\varphi^{(L)}$. During adsorption or desorption, initiated by stepwise variation of the external pressure, the refractive index of the host-guest system n is going to change depending on the number of molecules currently adsorbed within the porous material. In first approximation, proportionality between the change of local concentration of sorbate molecules $\Delta c(x, y, z, t)$ and the change of the local refractive index $\Delta n(x, y, z, t)$ is assumed, both depending on the certain position inside the three-dimensional crystal (x, y, z) and time t. The change of the phase difference as the quantity to be measured is, finally, found to be proportional to the change of the optical path length of the light beam passing through the crystal compared to that passing through the surrounding gas phase:

$$\Delta(\Delta\varphi^{(L)}(x, y, t)) \propto \int_0^L \Delta n(x, y, z, t)\mathrm{d}z \propto \int_0^L \Delta c(x, y, z, t)\mathrm{d}z. \qquad (3)$$

The drawback of this determination is obviously the lack of knowledge of concentrations $c(x, y, z, t)$ in true units, only relative numbers may be obtained. Furthermore, by integrating along the observation direction z, all information on the concentration distribution or mass transport in this direction is lost. This, however, may be overcome when studying two-dimensional systems with uniformly distributed sorbate molecules in z-direction where diffusion only occurs in the x-y-plane perpendicular to it, as it is the case for zeolite ZSM-58 investigated in sec. 4.

All experiments shown in this work were carried out at room temperature. However, with recent modifications to the vacuum system and optical cell, also measurements up to 100 °C are feasible [53], e.g. to obtain activation energies of diffusion. The resolutions in time and space attainable by IFM are about 15 s and 0.5 µm, respectively. Further information on the measuring principles and recent findings beyond those presented in this work may be found in refs. [21, 54, 55].

3. Zeolite ZSM-5 (MFI)

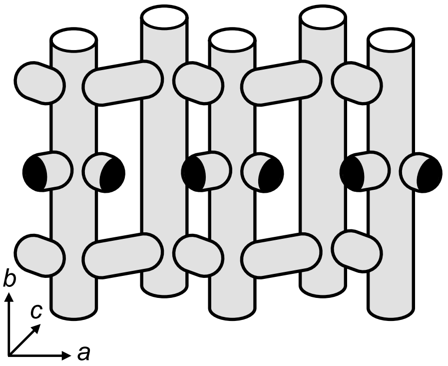

Figure 4: Straight and zig-zag channels of framework type MFI.

Zeolite ZSM-5 is one of the few zeolites being applied in large industrial scale, e.g. for catalytic cracking in petroleum chemistry. The first descriptions of synthetic MFI type zeolites originates from Kokotailo [56] and Flanigen [57], both published in *Nature* 1978. Following the classification of the International Zeolite Association [28], zeolite framework type MFI consists of five-membered oxygen rings as building blocks for the three-dimension configuration as shown in fig. 5. Depending on the desired properties and synthesis procedures, MFI type zeolites may occur in the all-silica form, in this case referred to as silicalite-1, or with a certain amount of aluminum and, hence, a well defined ratio of SiO_2/AlO_2 typically ranging from 20 to 30. The latter case, more generally referred to as ZSM-5, reveals a notable density of cations, leading to preferable behavior with respect to chemical reactions and catalysis. However, the structure of both, silicalite-1 and ZSM-5, is essentially the same.

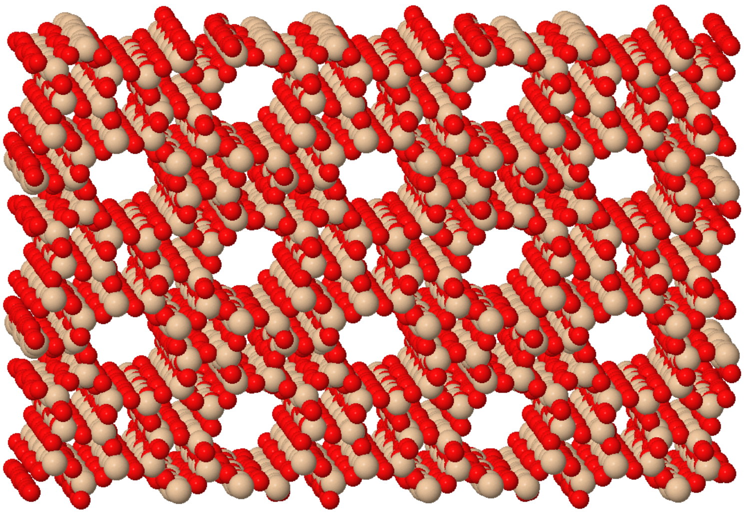

Figure 5: Structure of framework type MFI (depending on the aluminum content referred to as ZSM-5 or silicalite-1) along y-direction with silicon (or aluminum) in ocher and oxygen in red. The volume shown corresponds to approximately 14 unit cells.

Regarding mass transport and diffusion of sorbate molecules, the porous structure of MFI type zeolites consists of straight and zig-zag channels, both being circumscribed by ten-membered oxygen rings of about 0.6 nm diameter (fig. 4). An indication of the straight channels is also given by fig. 5 with the zig-zag channels running perpendicular and forming intersections. In the third direction of space (referred to as *c*-direction in fig. 4), diffusion may be somewhat slower as molecules need to hop rather than following a certain channel [58,59]. The thus obtainable diffusion anisotropy, as investigated in ref. [60], is also addressed in subsequent sec. 3.1 of this work.

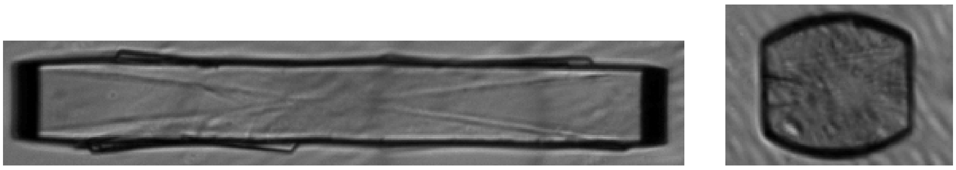
(a) (b)

Figure 6: Pictures of silicalite-1 crystals under study:
(a) coffin-shaped crystals with a size of $25 \times 25 \times 185\,\mu m^3$ and
(b) rounded boat shaped crystal with a size of $40 \times 28 \times 40\,\mu m^3$.

The IFM diffusion studies in this work were carried out using silicalite-1 crystals shown in fig. 6a and 6b, provided by Wolfgang Schmidt, Max-Planck-Institut für Kohlenforschung, Mülheim, Germany, and by Laurent Gueudré, former coworker from the University of Leipzig, having performed silicalite-1 synthesis previously at IFP Energies nouvelles, Lyon, France, respectively. It is well known from literature and previous IFM studies that, in a crystallographic sense, MFI type zeolites do often not appear as true single crystals, rather than comprising a twinned structure with varying crystal shape. Among other optical methods, including the use of polarized light [61] or fluorescent molecules [17], also IFM has been applied to study those intergrowth effects and potential inner surface barriers or accelerated diffusion pathways [62]. Furthermore, also the influence of crystal defects, such as cracks, which dramatically increase the uptake or release rates during adsorption and desorption, has been studied in great detail [46]. In addition, surface barriers are well known, yet often unattended, for zeolite and MOF crystals, leading to discrepancies between the diffusivities resulting for ideal crystal structure, as applied in computer simulations, and real structures accessible for the experimentalists. Regarding MFI type zeolites, surface barriers remain challenging as shown by the results in sec. 3.2, where new questions arise after previously performed IFM and IRM studies on silicalite-1 crystals being either free of surface barriers [49] or having intentionally created barriers on crystal fragments [50,63] and whole individual crystals [64].

3.1. Orientation-Dependent Guest Diffusion

As one of the few drawbacks, diffusion measurement by interference microscopy yield, as mentioned in sec. 2.3, the integral or average over the sorbate concentrations in the direction of observation (see eq. (3)) rather than the local concentrations themselves. Having a non-ideal host system with mass transport occurring in three dimensions, it is challenging to calculate, from these integral values, the true local concentrations $c(x, y, z, t)$. When applied to two-dimensional systems, as shown for zeolite ZSM-58 in sec. 4, this problem is immediately solved as soon as molecular movement is only allowed in the x-y-plane perpendicular to the observation direction. However, many porous host systems feature a 3D network of pores or channels, as it is true for zeolite framework type MFI. As shown in the following and recently published in [60], we succeeded, for the first time, in measuring diffusion by means of interference microscopy in three different orientations of an individual crystal by taking advantage of the rounded boat shape shown in fig. 6b. This shape allows positioning of the crystal on three different side faces. The synthesis of these crystals, performed by our former coworker Laurent Gueudré, followed the recipe given in ref. [65]. It is only this very crystal shape, referred to as *rounded boat*, which allows positioning of an individual crystal on all possible side faces (fig. 7b). However, for tracing diffusion anisotropy also with respect to the directions of the straight and zig-zag-channels, the crystal under study is in addition required to be a real single crystal, i.e. it should not be of the twinned structure, known to generally occur for the coffin-shaped MFI samples.

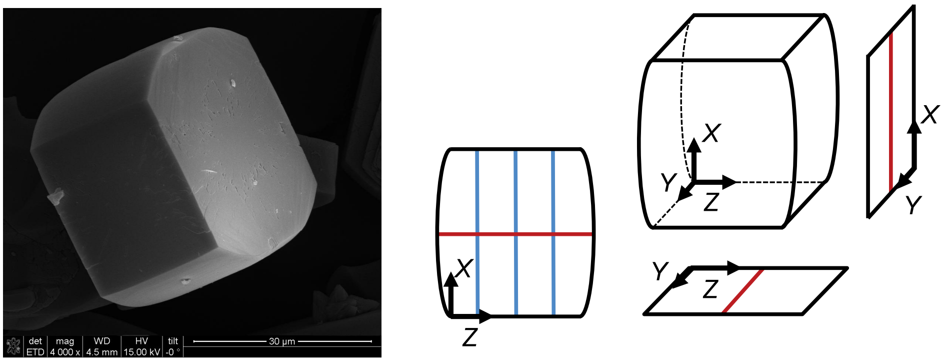

(a) (b)

Figure 7: SEM picture of *rounded boat* shaped silicalite-1 (a) and schematics on the three different observation directions (b) perpendicular to the X-Z-plane (left), the Y-Z-plane (bottom) and the Y-X-plane (right). Red and blue lines in (b) represent the directions of one-dimensional profiles in figs. 8 and 9, respectively. The mean crystal size is about $40 \times 28 \times 40\,\mu\mathrm{m}^3$.

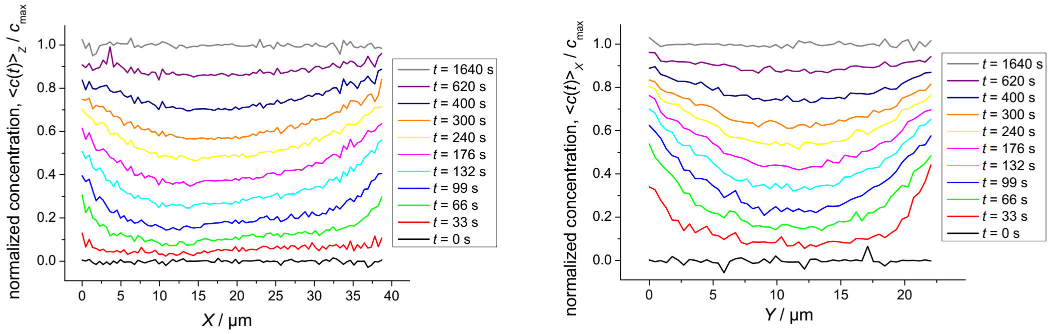

(a) $C_Z(X, Y = \text{const.})$ (b) $C_X(Y, Z = \text{const.})$

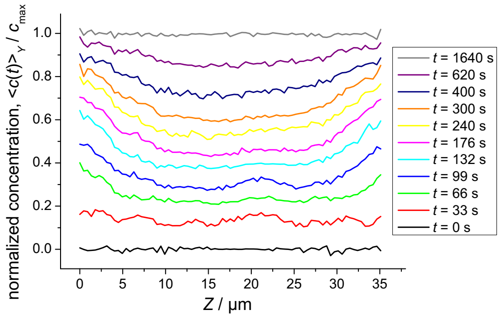

(c) $C_Y(Z, X = \text{const.})$

Figure 8: One-dimensional concentration profiles of 2-methyl-butane uptake in silicalite-1 following a pressure step from 0 to 1 mbar. The index i in C_i indicates the direction of observation and, therefore, the direction of concentration averaging. The profiles are presented along the red lines given in fig. 7b.

The experimental challenge of flipping a certain individual crystal within the optical cell is rather demanding and time consuming. At each crystal position, the exact pressure step for adsorption and desorption has to be reproduced for obtaining comparable results with respect to the IFM concentration profiles. In addition to the most instable position at the X-Y-face (see fig. 7), also effects of light diffraction and scattering at the curved crystal faces, and the varying crystal thickness in observation direction result in most demanding experimental conditions. In fig. 7b, capital letters (X, Y, Z) for the crystal directions are introduced to avoid confusion with either the spatial directions within the optical cell of the interference microscope (x, y, z) in fig. 2 and eq. (3), or the crystallographic directions of straight and zig-zag channels (a, b, c) in fig. 4. Finally, the concentration integrals are recorded as

$$C_X(Y, Z) \propto \int_{X=0}^{X=L_X} c(Y, Z, t)\mathrm{d}X, \tag{4}$$

where $C_X(Y,Z)$ represents the mean concentration $\langle c(Y,Z)\rangle_X$ at time t averaged in X direction over the whole crystal thickness L_X. After flipping the crystal to the other faces, $C_Y(X,Z)$ and $C_Z(X,Y)$ are obtained accordingly. The thus derived concentration profiles, presented as one-dimensional cuts along the red lines indicated in fig. 7b, are shown in fig. 8.

Even though the profiles presented in fig. 8 might seem unspectacular, the now available data basis is amazingly broad. For the first time, an individual crystal of zeolite framework type MFI is measured in all three possible orientations following the very same uptake process, namely the adsorption of 2-methyl-butane after an increase of the surrounding gas phase pressure from 0 to 1 mbar. Thereby, from each two-dimensional concentration profile $C_Z(X,Y)$, $C_X(Y,Z)$ and $C_Y(X,Z)$, corresponding to the three orientations shown in fig. 7b, one-dimensional cuts in two perpendicular directions can be obtained. By further analysis of these profiles, for the first time, a very detailed picture of the mass transport in a microporous crystal can be drawn, hence, providing information on diffusivities, surface permeabilities and possible anisotropic behavior.

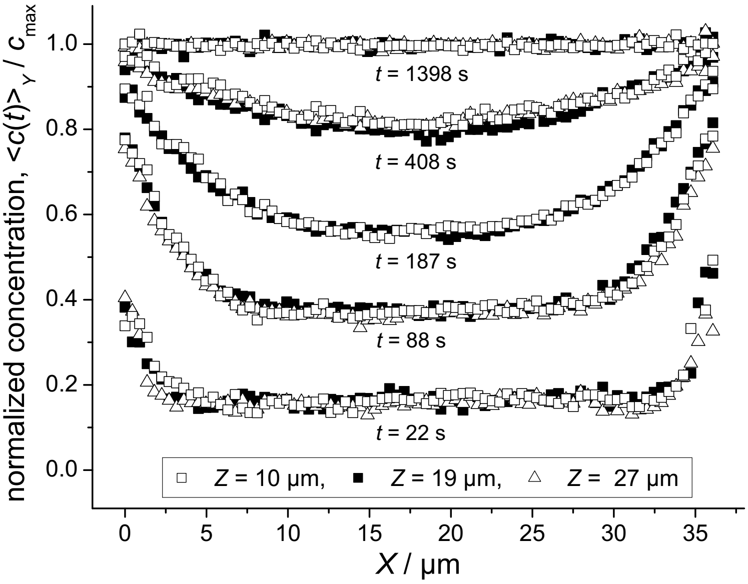

Figure 9: Proof of coincidence of crystal's Z and crystallographic c axis. One-dimensional concentration profiles, again after the 0 to 1 mbar pressure increase of 2-methyl-butane, in X direction at three different positions Z (□, ■ and △) as indicated by blue lines in fig. 7b. The agreement of the presented profiles suggests a notably reduced mass transport in Z direction, which has to be associated, therefore, with the c direction of the MFI framework (see fig. 4).

At this time, it is still unclear if the crystal under study can be referred to as a perfect single crystal, i.e. with the crystallographic axes (a, b, c) of fig. 4

running along certain crystal axes (X, Y, Z) homogeneously within the whole crystal. This would allow to study, in detail, the diffusion anisotropy in the directions of straight and zig-zag channels. As a first step, from fig. 9, the third direction c, in which mass transport is expected to be notably hindered, is found to coincide with the crystals Z axis. This conclusion is drawn from the coincidence of profiles in X direction at different positions Z, which, clearly, indicates a lack of diffusion pathways in this direction of the individual crystal. The self-evident explanation of this finding is that, for this type of rounded boat like silicalite-1 crystal, the straight and zig-zag channels are running in X- and Y-direction and, therefore, the crystal's Z-direction is in agreement with the c-direction of the MFI framework (see figs. 4 and 7b).

To further check whether the MFI type crystals are structurally coherent or not, a more quantitative determination of the transport parameters, i.e. diffusivities and surface permeabilities, is required. The method of choice is, in the following, to look for a best fit between experimentally-obtained concentration profiles and corresponding solutions of the underlaying diffusion equations. The numerical calculations are based on the general solution of the diffusion equation (Fick's 2^{nd} law, eq. (2)) [66], applied to a model crystal of identical size and using the previous finding of essentially no mass transport detectable in Z direction. The exemplary relations in crystal X direction are

$$\dot{c}(X,Y,Z,t) = \frac{\partial}{\partial X}\left(D_X \frac{\partial}{\partial X} c(X,Y,Z,t)\right) \tag{5}$$

and

$$D_X \frac{\partial}{\partial X} c(X,Y,Z,t)_{X=0(L_X)} = \alpha_X \left(c(X=0(L_X),Y,Z,t) - c_{\max}\right). \tag{6}$$

Here, the transport parameters are introduced as D_X, denoting the diffusivity in crystal X direction, and α_X, referred to as surface permeability, which is assumed to be identical at both crystal faces at $X = 0$ and $X = L_X$, respectively. In that sense, the surface permeability α is defined as the ratio of observed flux through a certain crystal face (here the Y-Z-face) as given by the left-hand side of eq. (6), and the difference of *real* intracrystalline sorbate concentration $c(X = 0(L_X), Y, Z, t)$ compared to the maximum or equilibrium concentration $c_{\max}$. Further explanations, details and examples of this concept on surface barriers, mathematically introduced in [66], may be found in refs. [8, 52, 67–69] and subsequently in sec. 3.2 of this work.

In addition to surface permeabilities deviating from the ideal case (of $\alpha = \infty$), also concentration dependence of the transport parameter D and α has to be considered. Hence, adapted from the so-called Fujita model [66, 70], the relations

$$D(c) = \frac{D_{c=0}}{1 - a \cdot c}, \quad \alpha(c) = \frac{\alpha_{c=0}}{1 - b \cdot c} \tag{7}$$

are introduced, with concentration c increasing from 0 to 1 relative units during adsorption, and a and b as parameters determining the strength of concentration-dependence of D and α. In principle, other relations of $D(c)$ and $\alpha(c)$ are applicable as well [60]. In the case of desorption experiments, usually the profiles are fitted as $1 - c_{\text{norm}}$, leading, in the case of no concentration dependence of D and α, to coincidence of adsorption and desorption profiles taken at the same time t after the start of the sorption process.

Using this set of tools and equations, a systematic variation of in total four fitting parameters $(D_{c=0}, \alpha_{c=0}, a, b)$ is performed by numerical calculations simultaneously for a set of 10 to 15 profiles taken at different times, if applicable combining both adsorption and desorption profiles in X and Y directions. These profiles were taken as one-dimensional cuts from the X-Z- and the Y-Z-profile, respectively, to ensure that any differences of the thus obtained diffusivities, if found at all, is not correlated to the second dimension of the former two-dimensional profile. Fig. 10 provides an overview about the thus derived agreement of experimental and calculated profiles for 2-methyl-butane in silicalite-1. The obtained transport parameters are summarized in tab. 2.

	pressure (mbar)	**direction**	**D** ($\text{m}^2\,\text{s}^{-1}$)	**α** ($\text{m}\,\text{s}^{-1}$)
methyl-butane	Ads, 0-1	X, Y	2.4×10^{-13}	1.5×10^{-7}
	Des, 1-0	X, Y	2.6×10^{-13}	5.0×10^{-8}
4M2P	Des, 1-0	X	4.4×10^{-13}	1.9×10^{-8}
	Des, 1-0	Y	5.2×10^{-13}	1.3×10^{-8}

Table 2: Parameters of mass transport in rounded boat shaped silicalite-1 crystals obtained by full profile fitting of IFM concentrations profiles for 2-methyl-butane and 4-methyl-2-pentyne (4M2P).

When fitting the experimental profiles of 2-methyl-butane, essentially no improvement to the fit quality could be found when choosing different diffusivities in X- and Y-direction. Hence, for both adsorption and desorption the values of D_X and D_Y were set to be identical, which, as an immediate consequence, leads to the conclusion that no diffusion anisotropy could be found for both directions of the crystal.

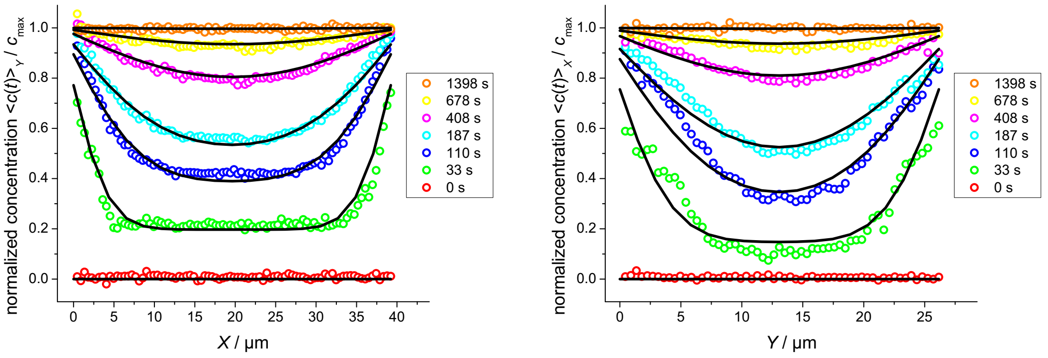

(a)

(b)

Figure 10: Determination of D and α for 2-methyl-butane in silicalite-1. The opened symbols represent experimental concentration profiles after a pressure increase from 0 to 1 mbar. Black lines show the calculated profiles following eqs. (5)-(7) as best fits to the experimental data. The thus derived transport parameters are in both directions $D = 2.4 \times 10^{-13}\,\mathrm{m^2 s^{-1}}$ and $\alpha = 1.5 \times 10^{-7}\,\mathrm{m\,s^{-1}}$. Differences in profile shape are only due to different crystal lengths L_X and L_Y.

To verify this finding, the concentration profiles in different crystal orientations were also measured and compared to calculated profiles for another sorbate species, viz. 4-methyl-2-pentyne (4M2P). For the diffusion of this more rod-like molecule, investigations by Rees and Song using frequency response suggest a much more pronounced diffusion anisotropy in MFI type zeolites [32,33]. More precisely, due to its very shape, the 4M2P molecules are expected to move much faster in the straight channels rather than the zig-zag ones. For this reason, when trying to find best possible agreement of calculated and experimentally measured profiles, D_X and D_Y are explicitly allowed to differ from each other. However, as shown in tab. 2, best agreement was obtained for diffusivities differing only within the range of uncertainty of about 20 %.

Summing up the results of these investigations, also the rounded boat shaped crystals of zeolite framework type MFI did not provide any sign of diffusion anisotropy in X- and Y-directions. Just as for the well-known coffin-shaped crystals, the crystallographic c-axis is found to coincide with the crystal Z dimension (with essentially no diffusion / mass transport in this direction). However, also here the existence of intergrowth and twinned structure is strongly suggested by the absence of significant differences between D_X and D_Y. Only a 90° rotation of the crystal's subunits [8,17] can explain the diffusivities found in this study, which in are in good agreement with data reported for the coffin-shaped silicalite-1 crystals [49].

3.2. Exploring the Nature of Surface Barriers

The kinetics of mass transport in nanoporous materials, such as zeolites and MOFs, is one of the key parameters for their industrial applications, e.g. in catalysis or separation. The former requires reactant molecules to diffuse to the active sites of the host material and product molecules to leave the porous system, while the latter is limited by fluxes through layers of the applied material. Doubtlessly, these transport phenomena are not only ruled by the intracrystalline diffusivities of the sorbate molecules, but to a significant extent also by transport resistances, in the case of inner or outer interfaces referred to as surface barriers.

For a broad variety of materials, such as zeolite framework types MFI, MOR, LTA or FER, surface barriers are known to give rise to notable discrepancies of diffusion measurements, if the applied and compared measuring techniques do not take these deviations from real structure into account [8]. Especially the observation times, and associated with it the mean square displacement of sorbate molecules, are determining the way how surface barriers may manifest in experimental data. In macroscopic measurements, e.g. gravimetric uptake experiments, the obtained kinetics are based on both intracrystalline diffusivities and interparticle transport resistances. In contrast, with microscopic methods, like nuclear magnetic resonance, surface barriers might not even be detectable, if sorbate molecules do not reach the particle surface during time of observation. It is the very benefit of micro-imaging by interference microscopy, to directly gain information on either of the rate determining transport parameters, D and α, following fig. 11 and eq. (8) on page 20.

Literature, including (yet not limited to) the previous work of coworkers from Leipzig, reveals several most intriguing examples of such surface barriers. Among them are aging effects of MFI zeolites and MOF crystals [50, 69, 71], comparison of barriers of mordenite zeolites by microscopic and macroscopic techniques [72], fundamental studies on MOF Zn(tbip) revealing almost total blockage of crystal surface [52, 68, 73] and its conformation by MD simulations [74], and finally also artificially created surface layers on MFI or LTA type zeolites either decreasing or even enhancing the uptake rate [64, 75–77]. In the following, a remarkable effect of surface barrier growth on coffin-shaped silicalite-1 crystals (fig. 6a) is studied in detail trying to elucidate the underlying process, which so far is assumed to be a formation of additional layers from residual water molecules acting as transport resistance for the probe molecule [50]. This view was based on the observation that the employment of a water trap consisting of small zeolite 3A spheres provides highly reproducible experimental conditions with respect to uptake rates, while otherwise, in the case of no water trap being applied, there is a notable growth of surface barriers.

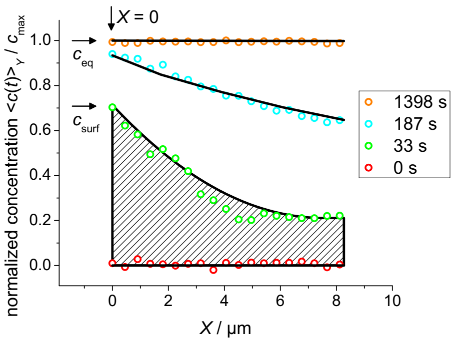

Figure 11: Determination of α.

The quantitative analysis of surface barriers by means of interference microscopy is based on surface permeabilities α, as above defined in eq. (6) following ref. [66]. It is noteworthy, that this approach towards the surface permeability α of a nanoporous crystal, sometimes also referred to as surface rate coefficient k_s [8], is differing from the definition of membrane permeability. Written slightly different, eq. (6) immediately leads to the concept of obtaining α from IFM concentrations profiles:

$$\boldsymbol{j}_{\text{surf}} = \alpha \left(c_{\text{surf}} - c_{\text{eq}} \right). \tag{8}$$

Here, $\boldsymbol{j}_{\text{surf}}$ denotes the particle flux density through the surface of a nanoporous crystal, and c_{surf} and c_{eq} correspond to the surface concentration and equilibrium (or maximum) concentration, respectively. From fig. 11, which displays an enlarged section of fig. 10a showing one-dimensional concentration profiles of 2-methyl-butane in silicalite-1 in X-direction, c_{surf} and c_{eq} may immediately be found. In addition, the time intervall Δt between two subsequent profiles and the integral $\int \Delta c \, \mathrm{d}X$, indicated as shaded a area for the profile at $t = 33\,\mathrm{s}$, are easily seen to determine the flux $\boldsymbol{j}_{\text{surf}}$ through the surface: In the case of MFI type zeolites (both rounded boat and coffin-shaped), there is no flux in Z-direction and profiles in X-direction are identical at different positions Z (fig. 9 on page 15). Hence, assuming a crystal size of $L_X \times L_Y \times L_Z$, the particle flux density into a *crystal slice* in the X-Y-plane of thickness d_Z is

$$\boldsymbol{j}_{\text{surf}} = \frac{\Delta N}{A \, \Delta t} = \frac{\int \Delta c \, \mathrm{d}V}{A \, \Delta t} = \frac{L_Y \, \cancel{\mathrm{d}_Z} \int_{X=0}^{X=L_X} \Delta c \, \mathrm{d}X}{2(L_Y + L_X) \, \cancel{\mathrm{d}_Z} \, \Delta t}, \tag{9}$$

with the particle number N and the relevant surface for mass transport calculated as $A = 2(L_Y + L_X) d_Z$. Fortunately, the unknown factor of proportionality for the IFM concentration profiles (given in arbitrary units or normalized to the equilibrium concentration) does not forbid α to be obtained in true units, as this factor is identical for c_{surf}, c_{eq} and Δc in eqs. (8) and (9), respectively.

Via this direct approach, surface permeabilities for adsorption of 2-methyl-butane in rounded boat shaped MFI crystals (figs. 10a and 11), following a pressure step from 0 to 1 mbar, are calculated as $(2 \text{ to } 4) \times 10^{-7}\,\mathrm{m\,s^{-1}}$ for the concentration profiles at different times t and, hence, different surface concentrations c_{surf}, ranging from 0.7 to 1. This is in perfect agreement with the data obtained by full profile fitting as shown in tab. 2 on page 17, where α at $c_{\mathrm{surf}} = 0$ is found to be $1.5 \times 10^{-7}\,\mathrm{m\,s^{-1}}$.

After this description of the calculation of surface permeabilities of nanoporous crystals from IFM concentration profiles and the quantitative validation with data from sec. 3.1, a very peculiar observation of growing surface barriers of coffin-shaped MFI type zeolites is reported. In previous studies by IR and IFM micro-imaging, using isobutane as probe molecule, the sample was modified by surface silanation, i.e. by synthesizing additional layers of trimethyl-, triethyl- and tripropylchlorosilanes onto the outer surface, to tune the uptake rate in a well defined way [64]. In addition, the (untreated) samples were found to be strongly sensitive to residual water molecules, leading to surface barriers continuously increasing with the number of adsorption-desorption cycles [50].

The chain of arguments leading to the latter hypothesis is based on the fact that, when a small amount of zeolite 3A pellets are placed at the tube of the optical cell just before the sample itself, the formation of surface barriers is prohibited. These 3A zeolites are referred to as a *water trap*, as their mean pore diameter is about 0.3 nm, which only allows very small species, like water, to be absorbed. However, if the water trap is omitted, the kinetics of isobutane adsorption slowly decreases. Regarding the very tiny amount of zeolite sample that is usually placed within the optical cell during IFM experiments, and by knowing that the vacuum pressure does not drop below 1×10^{-3} mbar, the assumption of a thin water layer to be formed at the outer crystal surface from residual water molecules seems reasonable, especially as the terminal silanol groups might act quite hydrophilic. Then, this water layer could, depending on its thickness, lead to notable transport resistances for the uptake of isobutane.

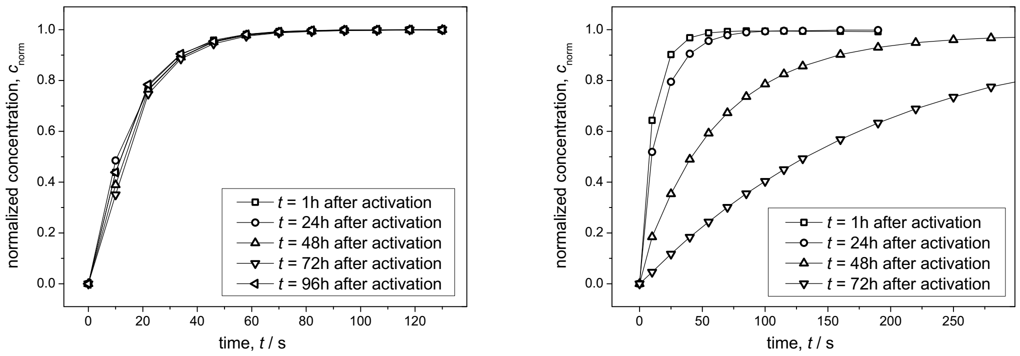

(a) with water trap

(b) without water trap

Figure 12: Comparison of isobutane (iC4) uptake curves with (a) and without (b) water trap, following a pressure step from 0 to 1 mbar, corresponding to a loading of about 2.8 molecules per unit cell.

Fig. 12 nicely pictures the impact of the 3A water trap on the reproducibility of transient isobutane adsorption in an individual MFI type zeolite crystal. While there is no difference found for the kinetics of this repeated experiment in fig. 12a, fig. 12b clearly shows that, by omitting the water trap, the overall uptake rate is dramatically decreased. All experiments were carried out using the very same crystal and with leaving the sample under vacuum pressure with the vacuum pump running after the cycle of adsorption and desorption. As a remarkable feature, when heated up under vacuum to a temperature of about 300 °C (referred to as activation), all previously formed surface barriers are removed and the uptake rate is as fast as known from the first experiments. This demonstrates that the ongoing processes at the crystal surface are reversible and, hence, cannot be caused by severe structural defects or collapse of the framework, as these damages would not be repaired by simply activating the sample. This result of growing surface barriers with waiting time was reproduced using several crystals from this unmodified batch of coffin-shaped silicalite-1 crystals and, in addition, from the modified samples having seen surface silanation as described in ref. [64].

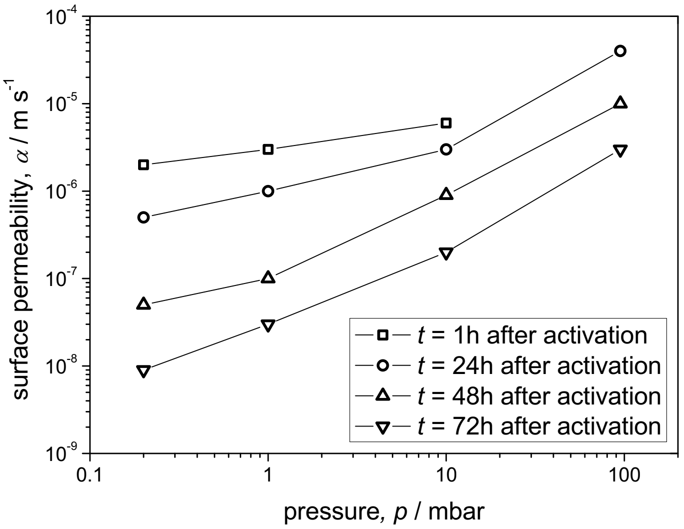

Figure 13: Growing surface barriers characterized by surface permeabilities following several pressure steps of isobutane from 0 to 95 mbar.

At this time, from fig. 12, only integral uptake curves are analyzed. They are very easily calculated by simply integrating (or summing up) the whole two-dimensional concentration profile obtained by means of interference microscopy. However, the profiles provide even more information, especially quantitative information on the surface permeability as described previously in this section. To really proof there is a dramatical decrease of the surface permeability, rather than a decrease of the intracrystalline diffusivity, and to check, additionally, a broader range of sorbate concentration, the following sequence of pressure steps was applied immediately after activation and on three subsequent days: 0 → 0.2 → 1 → 10 → 95 → 0 mbar. The thus derived surface permeabilities are shown in fig. 13.

The result of this study is impressive: It reveals surface permeability covering a range of almost four orders of magnitude comparing the different experiments. Both trends of this representation, i.e. decreasing surface permeabilities in time and increasing values at higher gas phase pressures, support the concept of small water layers to be formed. First, with only very few residual water molecules being present (while the vacuum pump is working), it is reasonable for the water layer to slowly grow in time, which causes the increasing transport resistance for the non-polar probe molecule isobutane. Secondly, the approximately linear relation between α and the gas phase pressure p at a certain time t after activation can be correlated with the solubility of isobutane in the water layer. The proportionality of α and p may be rationalized by implying a thin layer of thickness l at the outer surface characterized by a strongly hindered diffusivity D_{barr}. This was the usual model of choice in previous studies of surface barriers, such as in refs. [52, 78, 79]. Following Fick's first law (eq. (1)), the molecular flux through this barrier is

$$\boldsymbol{j} = D_{\mathrm{barr}} \frac{c_{\mathrm{eq}} - c_{\mathrm{surf}}}{l}, \tag{10}$$

which, when compared to the definition of surface permeabilities in eq. (8), leads to the relation

$$\alpha = \frac{D_{\mathrm{barr}}}{l}. \tag{11}$$

Now, in the case of thin water layers, D_{barr} has to be replaced by the diffusivity of the mobile species within this layer, reduced by the ratio of equilibrium concentrations in this layer and in the zeolite [8]:

$$\alpha = \frac{D_{\mathrm{iC4,\,aq}}}{l} \frac{c_{\mathrm{eq,\,aq}}}{c_{\mathrm{eq,\,MFI}}}. \tag{12}$$

For the given pressure range up to 100 mbar, the hardly water-soluble isobutane follows the Henry regime, hence, $c_{\mathrm{eq,\,aq}} \propto p$. Finally, with an isobutane isotherm in MFI type zeolites taken from literature [80], the above mentioned relation $\alpha \propto p$ is found, perfectly matching the experimental results of fig. 13. Furthermore, eq. (12) allows a rough estimation on the thickness l of the water layer. Assuming a diffusivity of isobutane in water of $D_{\mathrm{iC4,\,aq}} = 1.0 \times 10^{-9}\,\mathrm{m^2 s^{-1}}$ as given in the literature [81], the water layer width is indeed found to increase from about 0.2 nm, which would also be the range of uncertainty, at day zero to 1 nm 24 hours later.

However, with the experimental finding attained with the very plain set of experiments shown in fig. 14, our knowledge about the origin of this type of barriers is seen to be still rather limited. Again, an individual crystal of the very same silicalite-1 sample was probed with respect to the kinetics of isobutane uptake at several instances of time after thermal activation (black bars in fig. 14a). In this case, however, between resting times in vacuum, the sample was additionally exposed to a mild water atmosphere of about 20 mbar (shaded area in fig. 14a). Following the previously described theory of formation of water layers leading to transport resistances for isobutane, this water exposure should dramatically increase the crystal's surface barrier. However, the exact opposite is found: after resting times of 19 h and 28 h in water vapor prior to the uptake experiments shown as filled symbols in fig. 14, the surface barrier does not increase at all. In contrast, the presence of a mild water atmosphere is found to even prevent surface changes as the uptake curves are ideally matching the ones taken before water exposure. Only when vacuum is applied (prior to the uptake experiments shown as open symbols), the overall process of isobutane adsorption is slowed down.

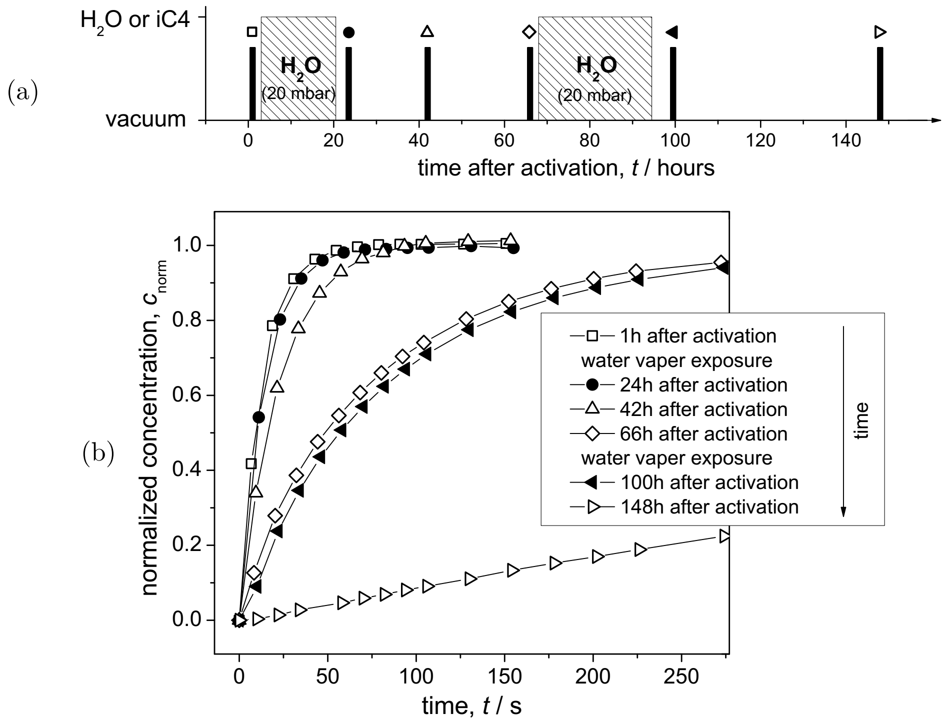

Figure 14: Uptake curves of isobutane (iC4) in one and the same silicalite-1 crystal after periods of water vapor exposure (shaded area in (a) and filled symbols for the subsequent iC4 uptake curve in (b)) and resting times in vacuum (open symbols for the subsequent iC4 uptake). Prior to the cycle of isobutane adsorption and desorption, the water atmosphere has been carefully removed.

This new finding is quite challenging, especially when seen together with all indications and experimental evidences described previously. Without being able to ultimately explain the mechanisms behind this story, so far only two working hypothesis are left: First, the crystal's surface, in particular the terminal silanol groups, might adopt an instable conformation upon thermal activation with a slow process of relaxation and reorientation following afterwards. This might lead to an increasing number of (partially) blocked entrances to the porous network. However, considering the cross-check from fig. 12 by applying or omitting a 3A water trap, the explanation of surface reorientation seems unlikely. In the end, pore blockage at the crystal surface might also be caused by traces of larger molecules, e.g. from vacuum grease. In that case, every atmosphere present (water, isobutane, etc.) could prevent those bulkier molecules from attaching to the surface and, thus, from forming surface barriers. Zeolite 3A particles placed before the sample itself would then also act as a trap for larger molecules, even if they do not enter the small 3A pores and only attach to the outer surface of the 3A pellets. However, at the time being, this puzzle remains unsolved.

3.3. Phase Transition Induced by Adsorption of Benzene

The last topic concerning zeolites of framework typ MFI, here the aluminum-free, coffin-shaped silicalite-1, has attracted lots of attention and already seen numerous publications. This special interest on phase transitions and framework effects of adsorbed aromatic hydrocarbons might result from two very fundamental observations: First, upon adsorption of species like *p*-xylene or benzene, with only the latter being in the focus of this IFM investigations, the zeolite host system undergoes certain changes in symmetry. Secondly, remarkable steps in the isotherm of these species reveal very strong changes in the sorbate-sorbate interactions associated with the formation of clusters and ordered phases of the adsorbed molecules.

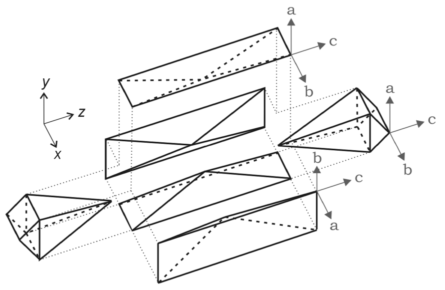

Figure 15: Orientations of six silicalite-1 subunits.

In general, zeolites are described as quite stable structures, remaining unaffected by thermal or mechanical stress. This is necessary for e.g. forming pellets at high mechanical pressures or for certain applications running at elevated temperatures. The recently discovered class of highly porous metal-organic frameworks (MOFs) [24] is, in contrast, known to be limited in their application, as their sample stability is generally inferior to that of zeolites. On the other hand, there are also options to benefit from the flexibility of MOF structures in certain applications for gas storage or separation, e.g. by exploiting the so-called *gate opening effect* in zeolite imidazolate framework ZIF-7 [82, 83] or MOF MIL-53, which shows *breathing behavior* under CO_2 adsorption [84] and, despite its large porosity, is also highly compressible [85].

It is, therefore, quite interesting that, also in the case of zeolites, structural changes are well-documented. Early reports on symmetry changes of the MFI framework under benzene and *p*-xylene adsorption are found in refs. [86, 87], in which powder X-ray analysis reveals three different symmetry forms depending on the amount adsorbed:

notation	**space group**	**appearance**
ORTHO	orthorhombic, $Pnma$	as-synthesized ZSM-5
MONO	monoclinic, $P2_i/n$	H-ZSM-5 (calcined)
PARA	orthorhombic, $P2_12_12_1$	*p*-xylene/H-ZSM-5 complex

Table 3: Symmetry forms of MFI type zeolites following the notation of ref. [87].

Furthermore, also temperature, aluminum content and extra-framework matter are found to influence framework symmetry [86]. It is noteworthy, that the here described MFI symmetry transformations are reversible and lead to only small changes in distances, angles and pore shapes. However, these small deviations might result in dramatic changes for the adsorbed species, especially for benzene in (aluminum-free) silicalite-1 [88].

Further literature data cover a broad range of experimental methods [89–95] and computational approaches [80, 92, 96] to gain insight into this striking field of host-guest interactions. Among these studies are reports on highly ordered adsorbate phases [89, 92], diffusion anisotropy [90, 95], distinctive isotherm steps at certain loadings [91, 93], crystal size expansion [94] and, additionally, cross-checks of those findings by Monte Carlo simulations [80, 96].

Despite this large number of reports available in the literature, micro-imaging by interference microscopy has turned out to provide an approach to gain a completely new type of insight into sorbate-induced phase transitions in nanoporous host-guest systems, referring to changes in both the framework and the state of the guest molecules. However, the experimental conditions turned out to be quite challenging. This is not only due to the strict requirements for temperature and pressure, both strongly influencing the strength and kinetics of the observable transition, but also due to notable differences between different crystals of the same sample. Additionally, differences in the time scales of the processes occurring after one pressure step and the comparably large signal changes (accompanied by a loss of picture contrast) entail numerous re-runs of certain experiments and additional time-consuming data treatment. The measurement to be described in the following were performed using silicalite-1 crystals of $25 \times 25 \times 185\,\mu m^3$ size as shown in fig. 6a following benzene pressure steps from 0 to 90 mbar at room temperature.

A very first consideration for IFM experiments of this system involves the question, whether the proportionality between the IFM signal (based on changing optical path lengths in observation direction) and the intracrystalline concentration as given by eq. (3) on page 10 still holds for changes in the framework and guest ordering. For clarifying this issue and, besides, for elucidating the range of loading (in terms of molecules per unit cell), in fig. 16 IFM single crystal isotherms are correlated with literature data obtained by gravimetric uptake experiments.

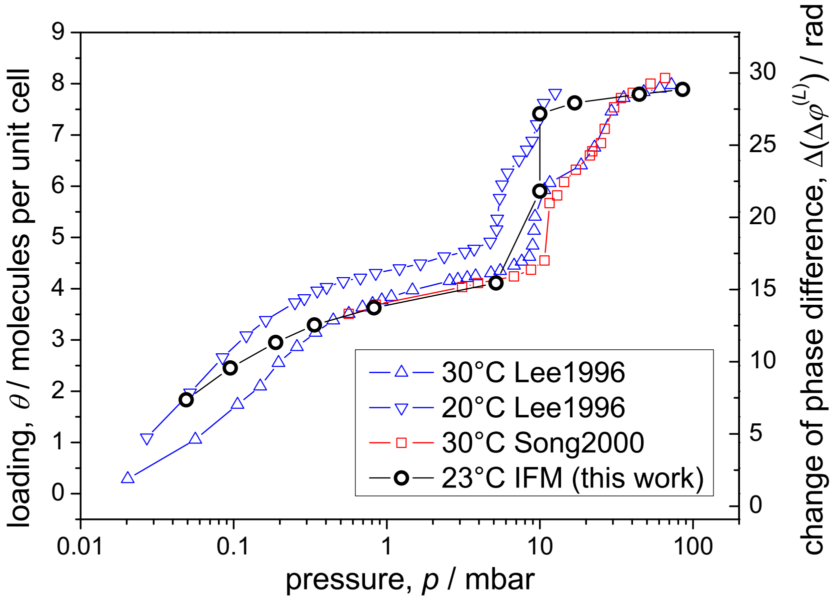

Figure 16: Comparison of benzene isotherms in silicalite-1 obtained by single crystal interference microscopy ($\Delta(\Delta\varphi^{(L)})$ scale, right) with literature data using gravimetric uptake (θ scale, left) [91, 93]. The measurement was repeated and confirmed for different crystals and, in addition, by means of IR microscopy.

The good agreement found between IFM isotherms and those from literature confirms that it is essentially the increase of sorbate concentration, rather than changes of framework symmetry, which is responsible for the obtained changes in the phase difference $\Delta(\Delta\varphi^{(L)})$. Furthermore, as predicted in the literature, by increasing the gas phase pressure the step-like behavior with potential phase transitions occurs at a loading of four molecules per unit cell. This region of interest is now further addressed by analyzing the transient concentrations profiles following a pressure increase from 5.0 to 10.0 mbar, corresponding to an increase of loading from 3.9 to 7.7 molecules per unit cell.

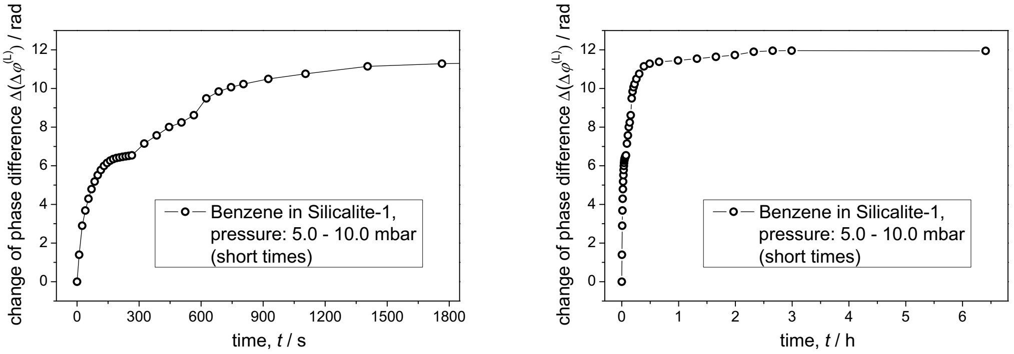

(a) short times

(b) long times

Figure 17: Uptake curve of benzene in silicalite-1 following a pressure step of 5.0 to 10.0 mbar, corresponding to an increase of loading from 3.9 to 7.7 molecules per unit cell.

Fig. 17 shows the integral uptake curve of this single crystal experiment for a time span of in total six hours (fig. 17b, right) and, for better visualization, the first 1800 s enlarged (fig. 17a, left). The scale of the IFM signal has deliberately not been normalized to range from 0 to 1 as it is important to recollect that IFM does not measure concentrations directly but via the change of optical path length. A signal change of $\Delta(\Delta\varphi^{(L)}) = 2\pi \approx 6.28$ rad corresponds to a change of optical path length (crystal thickness in observation direction $\times \Delta n$) of one wavelength, i.e. 589 nm.

The single crystal under investigation shows two separate steps of adsorption in its integral uptake curve, the first one during the first 300 s, the second one starting right after and taking about three hours with no further changes in the following three hours. This second step is characterized by a strong increase during 30 min and a slower change within the next 2.5 h. From comparison with gravimetric uptake isotherms (fig. 16), the corresponding loadings are approximately 3.9, 6.2 and 7.8 molecules per unit cell at the beginning, after the first step at $t = 300$ s and in equilibrium, respectively. The colored maps of IFM signal (commonly referred to as concentration profile) are shown in figs. 18 and 19, revealing two completely different processes without any further changes in the external conditions.

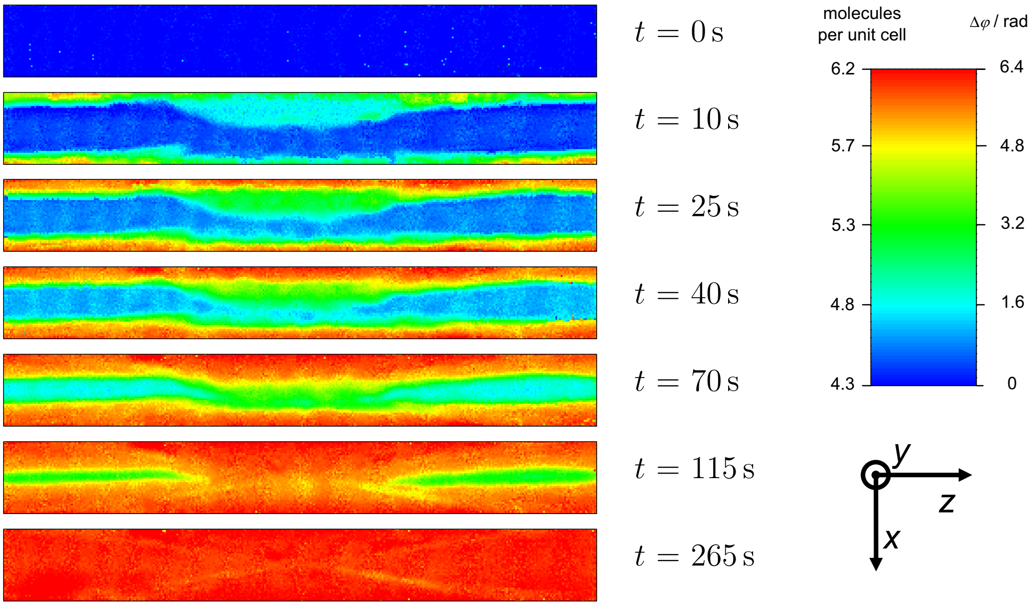

Figure 18: Two-dimensional maps of the IFM signal $\Delta(\Delta\varphi^{(L)})$, being proportional to the overall loading, following the first 265 s of adsorption of benzene in silicalite-1 after increasing the gas phase pressure from 5.0 to 10 mbar. Crystal size is appr. $25 \times 25 \times 185\,\mu\mathrm{m}^3$.

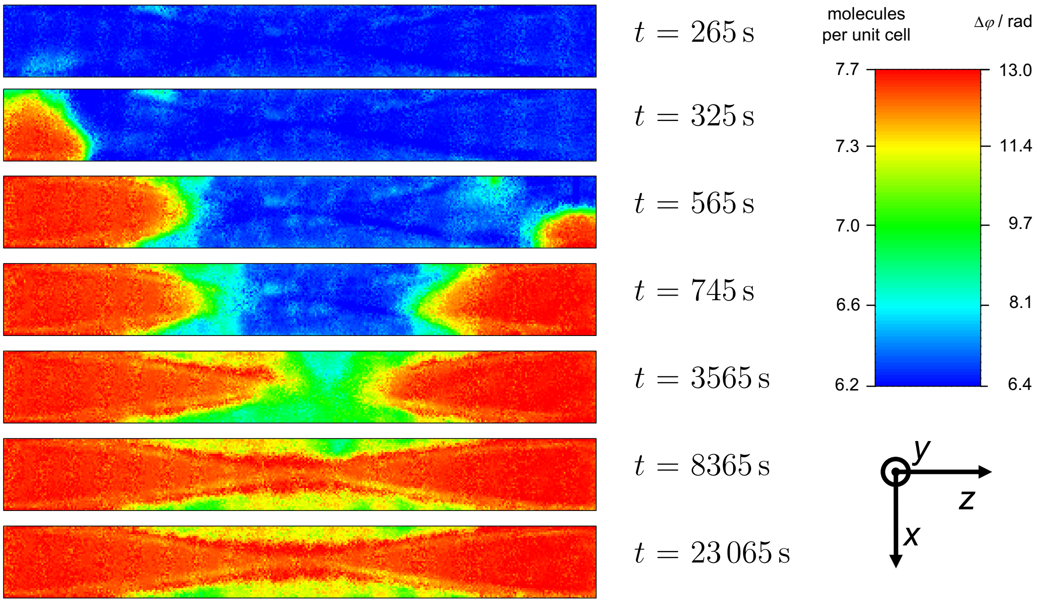

Figure 19: Continued maps of IFM signal $\Delta(\Delta\varphi^{(L)})$ for longer times following the phase transition of the sorbate phase. Note, the legend color was changed for better visualization.

The evidence provided by the experimental data shown in figs. 18 and 19 and the integral uptake curve in fig. 17 may be summarized as follows:

(1) There is no additional change of pressure or any other variation in the external experimental conditions between step one and two.

(2) Step two occurs over a much longer timescale than step one and deviates distinctly from a single exponential behavior.

(3) The diffusion front of step one runs along the crystal's x-direction and, most probably, also in observation direction (y). This is the expected, *normal* behavior for mass transport in a coffin-shaped silicalite-1 crystal, as observed with various guest species, including isobutane as presented in the study of surface barriers in sec. 3.2.

(4) In step one, there are indications for a small crack at the upper side face leading to slightly faster uptake at the top center region of the crystal.

(5) The *front* of step two is seen to move, counterintuitively, in the z-direction, in which no channels are running and mass transport is therefore by at least on order of magnitude slower than in the x- or y-direction.

(6) The equilibrium profile ($t = 23\,065\,\mathrm{s}$) shows a remarkably inhomogeneous distribution in the phase changes.

The discussion of those findings is challenging, however, based on the evidence so far reported in the literature, the following picture can be drawn:

After having increased the benzene gas phase pressure beyond 5 mbar, the threshold loading of four molecules per unit cell is passed and phase transitions are expected to occur for both, the sorbate phase in terms of relocating, reorientating and clustering, and the sorbent material in terms of symmetry changes and angle or distance distortions. However, as found by the comparison with isotherms of gravimetric measurements, which, according to their working principle, are unaffected by framework changes and only measure true loadings, the change of the IFM signal in both steps of the experiment following the pressure increase from 5.0 to 10 mbar have to be linked to changes in the intracrystalline concentration rather than to variations in the refractive index of the host material.

As a most remarkable finding, the phase transition of benzene, connected with a rapid increase of the pore filling from 6.2 to 7.8 molecules per unit cell, is progressing along the crystal's longitudinal z-axis, which is, for all six subunits (fig. 15), identical to the c-direction of the MFI framework. The exceptional kinetics of this process is based on the observation that these phase transitions are seen to not occur simultaneously on the right and left end of the crystal.

For the first time, also, the finally obtained IFM equilibrium profiles (as shown for $t = 23\,065\,\mathrm{s}$ in fig. 19) are found to reveal inhomogeneities. However, it is not the benzene concentration being irregularly distributed, it is the effect of a highly oriented sorbate phase, which breaks the so far assumed proportionality of change of optical density and concentration (eq. (3) on page 10). As two out of six subunits of the coffin-shaped silicalite-1 crystal are rotated by 90° (fig. 15), also the well aligned benzene molecules are rotated within the porous system. An estimate, based on the polarizability α of benzene molecules depending on their orientation, gives the following values for the refractive indices:

polarizability	**refractive index**
$\alpha\ = 10.3 \times 10^{-30}\,\mathrm{m}^3 \times 4\pi\epsilon_0$	$n\ = 1.50$
$\alpha_\perp = 6.7 \times 10^{-30}\,\mathrm{m}^3 \times 4\pi\epsilon_0$	$n_\perp = 1.30$
$\alpha_\parallel = 12.8 \times 10^{-30}\,\mathrm{m}^3 \times 4\pi\epsilon_0$	$n_\parallel = 1.64$

Table 4: Refractive index of benzene in the free liquid (first row) and polarizabilities α, $\alpha_\perp$ and $\alpha_\parallel$ from ref. [97]. For a highly ordered benzene phase, the refractive indices $n_\perp$ and $n_\parallel$ are calculated by using the Clausius-Mossotti equation (see appendix A.3.3).

From tab. 4, the difference of $n_\perp$ and $n_\parallel$, divided by the refractive index n of the randomly distributed bulk phase of benzene, is about 0.23. Assuming that only benzene molecules beyond four molecules per unit cell loose their rotational degree of freedom and form a new, oriented phase, this should lead to differences in the IFM signals for differently oriented subunits of $12.0\,\mathrm{rad} \times 0.23 = 2.8\,\mathrm{rad}$, where 12.0 rad is the averaged IFM signal of the whole profile of this pressure step from 5.0 to 10 mbar. This number of approximately 2.8 rad is in perfect agreement with the experimentally observed difference of the IFM signal in the equilibrium profile of step two shown in fig. 19 ($t = 23\,065\,\mathrm{s}$), where the dark red areas are in the range of $(13.0 \pm 0.3)\,\mathrm{rad}$ and the green-yellow parts at $(10.5 \pm 0.5)\,\mathrm{rad}$. This agreement demonstrates that, except for the four molecules per unit cell remaining in the intersections and being randomly rotated there, additional benzene molecules are forming a highly ordered phase with a positioning in parallel to observation direction at the four central subunits, perpendicular to the path of light beam in the two rotated subunits. As indicated by so-called solid docking simulations in ref. [98], at higher loadings benzene molecules are pushed from the intersections to the straight channel segments with their plane being perpendicular to the channel direction.

To cross-check the possible interplay of phase transition for the benzene molecules adsorbed and the framework symmetry changes, additional XRD experiments were performed using the same silicalite-1 sample. For this purpose, two samples were prepared in tiny glass capillaries: the first one with empty crystals, the second one after increasing the benzene gas phase pressure to 20.0 mbar. Both capillaries were sealed by melting. The benzene-loaded sample had been measured at different times after the first contact with benzene, namely after 4 hours, 12 hours, 18 hours and two days. The diffractograms confirm the symmetry change from monoclinic to orthorhombic (fig. 20) upon comparison with the simulated patterns, where, however, the first two measurements are seen to yield a kind of intermediate between empty and filled phases. The timescale of framework changes is, therefore, found to be in the range of 12 hours, during which the phase transition of the sorbate should be finished much faster (especially regarding the larger pressure step). This suggests that the change in framework symmetry is a consequence of the high sorbate loading but should not be influencing the previously described behavior of the orientation process of benzene.

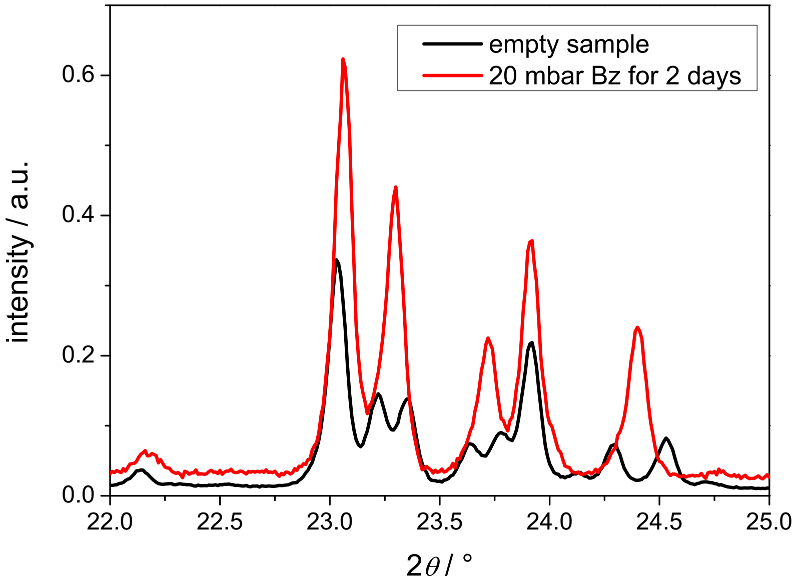

Figure 20: Structural analysis of empty and benzene-loaded silicalite-1 by XRD. The samples were prepared in the IFM lab in tiny glass capillaries, one sealed (by melting) immediately after activation and evacuation, the second sealed after setting the gas phase pressure to 20.0 mbar.

Remarkably, the diffusivity of benzene in silicalite-1 changes dramatically, namely by more than two orders of magnitude, above a loading of about four molecules per unit cell (fig. 21). Until this concentration is reached, transport diffusivity is found to be stable at $D = 1.5 \times 10^{-14}\,\mathrm{m^2s^{-1}}$. As a rough estimation, for higher concentrations close to eight molecules per unit cell, the transport diffusivity is larger than $D = 4 \times 10^{-12}\,\mathrm{m^2s^{-1}}$, which is, for the actual crystal size, the upper limit obtainable by IFM. The intermediate value at $p = 10\,\mathrm{mbar}$ results from analyzing step one of the phase transition experiment explained in detail before. The corresponding uptake times are approximately 2 hours at low loadings, 300 s during the phase transition step and about 10 s close to pore filling. This enhancement of mass transport, also confirmed by IR uptake experiments (see appendix A.3.3), may be assumed to result from a much higher mobility of the benzene clusters being formed at high loadings [98].

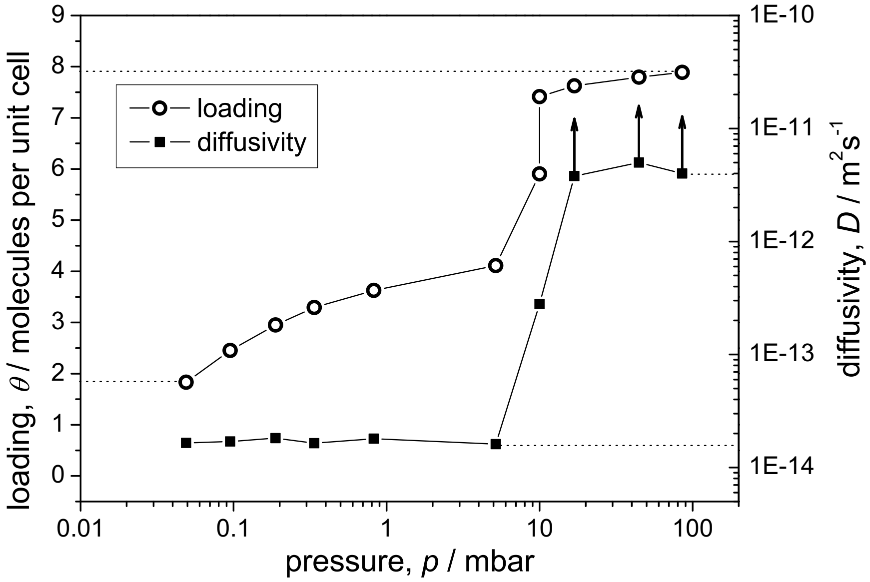

Figure 21: Diffusivities of benzene in silicalite-1 obtained from the integral uptake curves. The three values at highest loadings (close to eight molecules per unit cell) indicate only the lower limit of the true D values. At these loadings, already more than 95 % of the final uptake is reached within the initial 10 s (which is the temporal resolution of IFM).

This section on phase transition of benzene in silicalite-1 demonstrates how interference microscopy yields new insights into the details of mass transfer processes [99], which are unattainable by other experimental methods. The high spatial and temporal resolution of IFM allows an in-depth study of the formation of an ordered and oriented sorbate phase. It could be shown that, by using the different refractive indices for aligned benzene molecules, the picture of MFI subunits rotated by 90° is confirmed by high pressure equilibrium maps of IFM signal. The suggested scenario of phase transitions, as used for an interpretation of the observed inference patterns, is confirmed by accompanying XRD experiments and the diffusion coefficients resulting from molecular uptake.

4. Zeolite ZSM-58 (DDR)

The second host system to be studied in the present work is zeolite ZSM-58 of framework type DDR [28]. The first description of its synthesis was given by H. Gies in 1986 [100] and in a US patent of Exxon in 1987 [101]. Shortly after, template-free synthesis of zeolite ZSM-58 was found [102]. Building blocks of the DDR framework, [SiO_4] tetrahedra, form pseudohexagonal layers, which are stacked in an ABCABC sequence. The connections between these layers are created by additional [SiO_4] tetrahedra, forming six-membered rings of about 0.26 nm diameter [100]. Within the individual layers, 19-hedron cages with a diameter of 0.77 nm are built and interconnected by eight-membered rings with diameters of 0.36 to 0.44 nm. Due to this small window size dictating the rate of mass transfer of the sorbate species, DDR zeolites are investigated with respect to applications in separation [35, 103–105], e.g. of light olefins and paraffins [106–108] or CO_2 and methane [109–112]. However, by benefiting from its shape selective behavior, DDR zeolite also offers catalytic properties in the methanol to olefins (MTO) process [113].

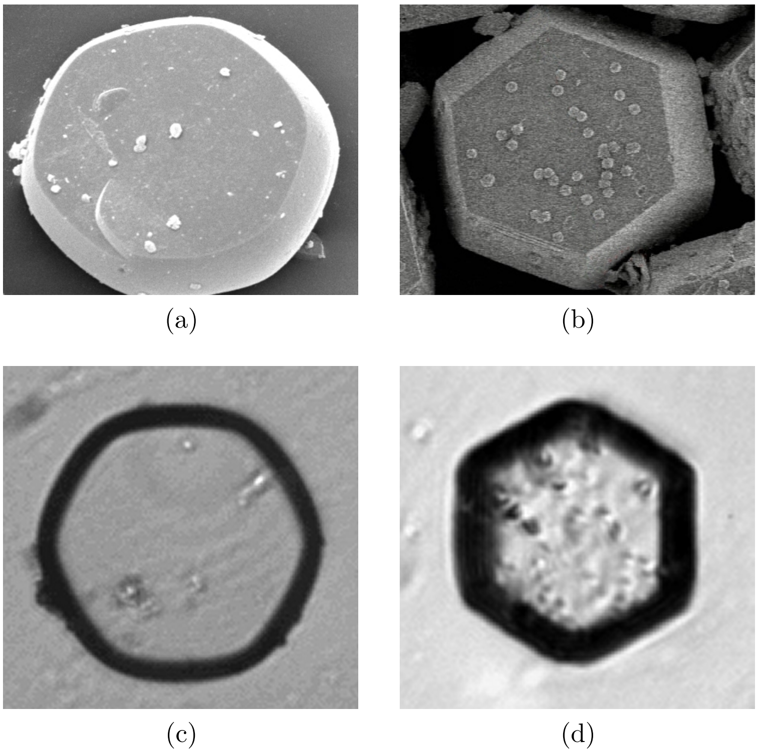
(a) (b)

(c) (d)

Figure 22: Pictures of two different zeolite ZSM-58 samples, DDR-I (a,c) and DDR-II (b,d), taken by SEM (a,b) and light transmission microscopy (c,d). Crystal diameters are 52 and 37 µm (tab. 5), respectively.

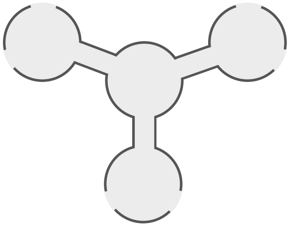

Figure 23: Sketch of cages and windows in DDR.

In terms of diffusion studies, the eight-membered ring zeolites posses the smallest channels or windows to be investigated in the family of zeolites, as their diameter is in the range of small hydrocarbons (see tab. 1 on page 6). The slightly smaller six-membered ring windows connecting the stacked layers are already too small to allow diffusion in this direction, resulting for DDR zeolites to be a two-dimensional system of cylindrical symmetry (fig. 23, cages and windows have diameters of 0.77 nm and 0.36 to 0.44 nm, respectively). With respect to diffusion studies by means of interference microscopy, hence, this material provides exceptional convenient experimental conditions: With the large top and bottom faces of the DDR crystals (fig. 22) being oriented perpendicular to the axis of radial symmetry, there is no mass transport to by expected in observation direction. Only perpendicular to it, within the x-y-plane, mass transport is occurring through the eight-membered ring windows. With only small deviations due to the hexagonal rather than circular crystal shape, concentration profiles reveal cylindrical symmetry, thus, allowing to average over areas of equal distance r from the crystal center and, hence, to significantly increase the signal-to-noise ratio. The methods of data analysis of two-dimensional concentration profiles of this cylindrical symmetry is further discussed in the subsequent sec. 4.1.

	DDR-I	**DDR-II**	**DDR-III**
Crystal size (μm)			
in radial direction ($2R$)	52	37	23
in axial direction (L)	14	20	13
Si/Al ratio	-	1662	950
BET (m^2/g)	375	-	365
surface	clean	speckled	clean

Table 5: Comparison of crystal properties of three different samples of DDR type zeolites. The crystal shape varies slightly from almost cylindrical (DDR-I, see fig. 22a) to hexagonal with side faces like truncated octahedron (DDR-II and DDR-III, fig. 22b). The sample notation is identical to refs. [114, 115] and slightly different from refs. [111, 116], where the here labeled DDR-III is referred to as DDR-I.

The results of detailed investigations on intracrystalline diffusion of small hydrocarbons in DDR zeolites are presented in sec. 4.2. As we were kindly provided three different DDR samples (tab. 5) showing different crystal sizes and being synthesized in different labs, in addition, a comparison of these materials in terms of mass transfer and diffusion is possible.

For the first time, in the concluding sec. 4.3, mixture adsorption has been investigated by means of interference microscopy. In contrast to IR imaging, where different sorbate species are distinguishable by their different IR bands, in this case of IFM studies, mixture analysis was only made possible by the huge difference of intracrystalline diffusivities of the mixture components, viz. ethane and CO_2.

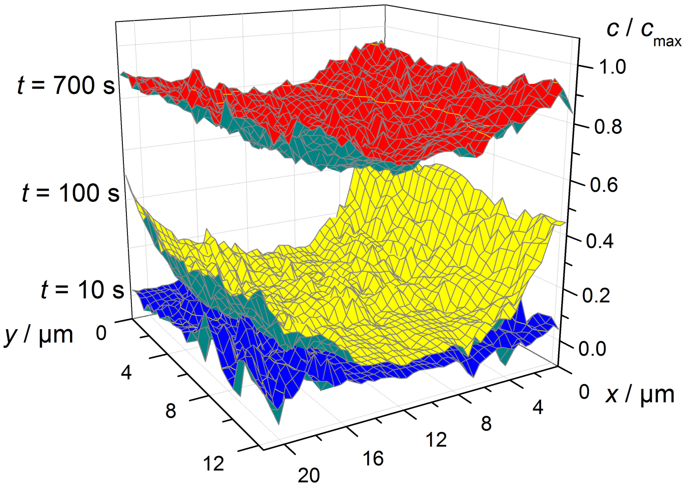

Figure 24: Two-dimensional concentration profiles of ethane in DDR-II taken at three different times t after increasing the gas phase pressure from 0 to 210 mbar. For better visibility, only the crystal's center part is shown.

4.1. Analyzing Concentration Profiles of Cylindrical Symmetry

Compared to the situation of MFI type zeolites presented in sec. 3, IFM data analysis offers new approaches towards intracrystalline diffusivities for DDR type zeolites by benefiting from the two-dimensional uptake of sorbate molecules. In non of the numerous experiments with the three DDR samples any indications for surface barriers were found, which is supported by reports in literature using ZLC [111, 116] and breakthrough experiments [107]. However, a quantitative determination of surface permeabilities α by means of IFM (as done for silicalite-1 in sec. 3.2) is hindered by the lack of knowledge about boundary or surface concentrations $c_{\text{surf}} = c(r = R)$. This results from the curved or tilted side faces of the DDR species (figs. 22a and 22b), which causes the outer crystal shell to appear as black areas in light transmission microscopy (figs. 22c and 22c). Actually, from the shape of concentration profiles and uptake curves, strong surface barriers can be excluded. Two-dimensional profiles, the basis of further investigations on diffusivities obtained by IFM, are shown by way of example in fig. 24 for ethane in DDR-II. The following methods of data treatment were published in ref. [114].

4.1.1. Fitting concentration profiles and uptake curves by solutions of the diffusion equation

Probably the most direct approach to obtain diffusivities from IFM experimental data is to follow the diffusion equation (Fick's 2nd law, eq. (2)). For the change of concentration c in time t, written in polar coordinates, one obtains

$$\frac{\partial c}{\partial t} = \frac{1}{r}\frac{\partial}{\partial r}\left(rD\frac{\partial c}{\partial r}\right) = D\frac{\partial^2 c}{\partial r^2} + \frac{\mathrm{d}D}{\mathrm{d}c}\left(\frac{\partial c}{\partial r}\right)^2 + \frac{D}{r}\frac{\partial c}{\partial r}, \tag{13}$$

where D and r denote the diffusivity and distance from the symmetry axis, respectively. Solutions for this equation are available for both time depending concentration profiles, $c(r,t)$, and the overall uptake curve, $\frac{m_t}{m_\infty}$, i.e. the loading m_t at time t divided by the equilibrium or saturation loading m_∞ [66]:

$$\frac{c(r,t)}{c_{\max}} = 1 - \frac{2}{R}\sum_{n=1}^{\infty}\frac{\exp[-D\alpha_n^2 t]J_0(r\alpha_n)}{\alpha_n J_1(R\alpha_n)}, \tag{14}$$

$$\frac{m_t}{m_\infty} = 1 - \sum_{n=1}^{\infty}\frac{4}{R^2\alpha_n^2}\exp(-D\alpha_n^2 t). \tag{15}$$

In eqs. (14) and (15), R is the radius of the cylindrically shaped crystal, J_i denotes the Bessel function of order i and the α_n are given as the n^{th} positive root of

$$J_0(R\alpha_n) = 0. \tag{16}$$

The just presented formulas do not include any concentration dependence of D, which is, however, to be expected for at least some of the sorbate species and pressure ranges. A strong indication of concentration-independent diffusivity is the agreement of adsorption and desorption profiles or uptake curves in terms of

$$\left(\frac{m_t}{m_\infty}\right)_{\text{ads}} = 1 - \left(\frac{m_t}{m_\infty}\right)_{\text{des}} \quad \text{and} \quad \left(\frac{c(r,t)}{c_{\max}}\right)_{\text{ads}} = 1 - \left(\frac{c(r,t)}{c_{\max}}\right)_{\text{des}}. \tag{17}$$

This could be found for methane in DDR, which, at the applied pressures below 1 bar, is only weakly adsorbed. As a result, the obtained IFM signals were quite weak and noisy, which could be notably improved by averaging the concentration profiles over areas of equal distance r from the symmetry axis (fig. 25).

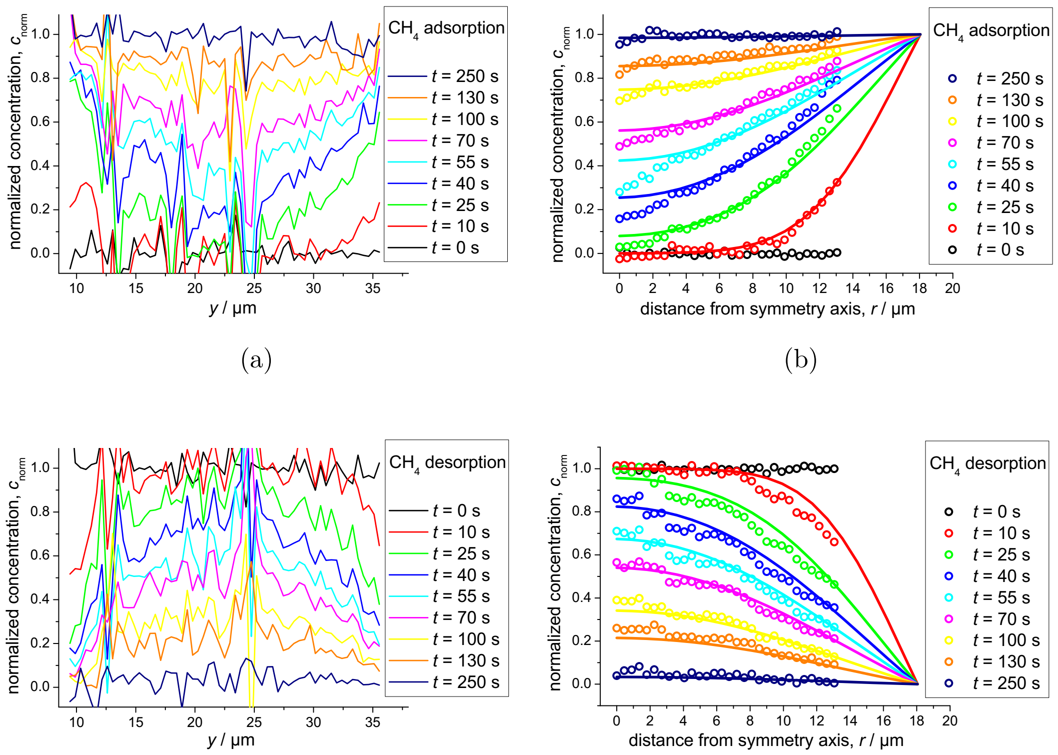

(a) (b)

(c) (d)

Figure 25: Averaging of concentration profiles of cylindrical symmetry: The raw and untreated concentration profiles for adsorption (0 to 800 mbar) and desorption (800 to 0 mbar) of methane in DDR-II (a, c) are significantly improved by averaging over areas of the same distance r from the crystal center (b, d).

In fig. 25, the experimental profiles miss data points of the outer 20 % of the crystal due to the unaccessible black areas shown in fig. 22d. However, the full profile fitting following eq. (14), represented by solid lines in fig. 25b and

25d, yields nice agreement with the concentration profiles averaged of identical distances r. Only the data at the crystal center (r close to 0) still exhibit notable scatter, as the number of data points to be averaged decreases with decreasing r. For methane in DDR-II, the thus obtained diffusivity is $D = 0.96 \times 10^{-12}\,\mathrm{m^2 s^{-1}}$ for both adsorption and desorption.

4.1.2. Short-time analysis by the Boltzmann-Matano approach

Even though the previously described fitting of profiles and uptake curves easily yields the desired diffusivity, so far, its concentration dependence is not addressed. If the overall uptake process is slow enough to obtain several concentration profiles at short times, i.e. before the diffusion front reaches the crystal center, the system can be assumed to experience diffusion as into a semi-infinite medium. This allows analysis by the Boltzmann-Matano approach described in refs. [34, 40, 66]. Here, all short-time concentration profiles are found to coincide when plotted against $x/\sqrt{t}$ rather than against just x (fig. 26a). The thus derived master curve yields the diffusivity D, which is, in the case of no concentration-dependence, found from the relation

$$\frac{c}{c_{\max}} = \operatorname{erfc}\left(\frac{x}{2\sqrt{Dt}}\right). \tag{18}$$

In addition, also master curves of systems with explicit concentration dependence of D can be analyzed and fitted (fig. 26d), especially when assuming $D(c)$ to follow the Fujita model [70]

$$D(c) = \frac{D_{c=0}}{1 - \lambda \cdot c}. \tag{19}$$

The very benefit of this approach, which, for all small hydrocarbons in DDR zeolites, provided satisfactory data for the $D(c)$ relation, is the (implicit) solution for $\frac{c}{c_{\max}}$ over $x/\sqrt{t}$ to be available from literature [70], allowing to obtain both parameters, $D_{c=0}$ and λ from this single master curve.

In addition, the concentration-dependent diffusivity is as well accessible from the direct Boltzmann-Matano approach [8, 34], i.e.

$$D(c) = -\frac{1}{2t}\frac{\mathrm{d}x}{\mathrm{d}c}\int_0^c x\,\mathrm{d}c, \tag{20}$$

with all quantities to be obtained directly from the IFM concentration profiles. Again, the approach is limited to short times t, i.e. to times before the diffusion front reaches the crystal center. Fig. 26 represents the feasibility of this approach for ethane in DDR-I.

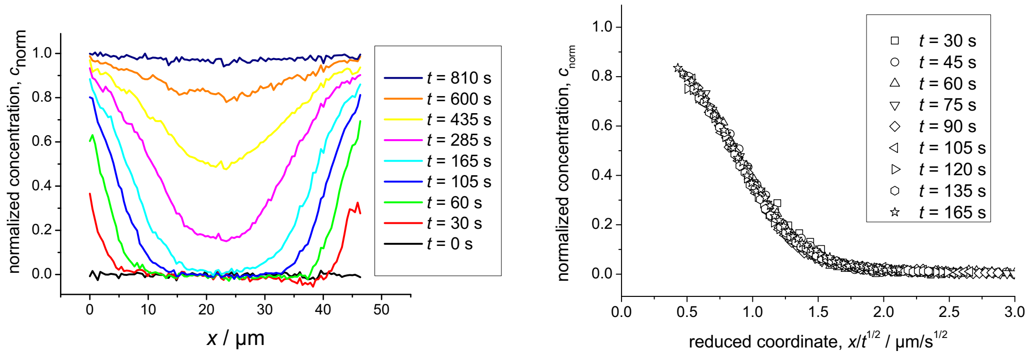

(a) 1D concentration profile

(b) master curve (short times)

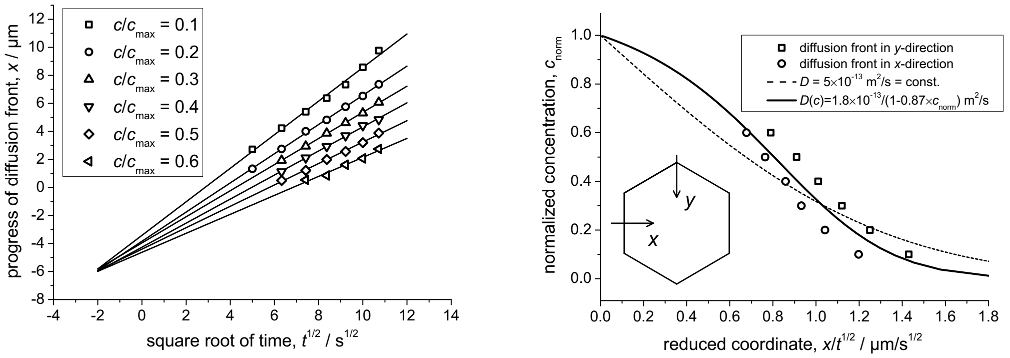

(c) progress of the diffusion front

(d) diffusion model

Figure 26: Short-time analysis of ethane in DDR-I using the Boltzmann-Matano-approach. IFM concentration profiles, as shown in (a), were obtained after increasing the gas phase pressure from 0 to 230 mbar. When plotted against $x/\sqrt{t}$, the profiles at short times are found to nicely coincide (b). The data points in (d) were obtained from the slope of linear fits in (c), where the progress of the diffusion front is followed.

The master curve shown in fig. 26b, obtained by plotting the concentration profiles against $x/\sqrt{t}$, can also be rebuilt by tracing the progress of the diffusion front (fig. 26c). For an ideal process and perfect experimental data, the linear fits of points of identical normalized concentration (0.1, 0.2, 0.3, 0.4, 0.5 and 0.6) are expected to intersect in the origin at $x = 0$ and $t = 0$. The finding of fig. 26c about the intersection to occur at $x = -6$ µm and $t = -4$ s is, however, neither surprising nor disturbing. It simply results from the already mentioned problems of measuring close to the crystal surface (obviously, fig. 26a is lacking this area) and from the fact that one concentration profile is calculated out of five different interference pictures recorded during a time interval of about 12 s. In this sense, an offset of about $x = -6$ µm and $t = -4$ s is quite reasonable. Fortunately, the linear regression is unaffected and, as shown in fig. 26d, leads to two curves (one for profiles in x-direction, the second for y-direction) These can nicely be used to obtain a concentration-dependent diffusivity $D(c)$ when compared to a calculated curve (solid line) in this c_{norm}-vs-$x/\sqrt{t}$ picture. In contrast, the theoretical curve for the concentration-independent diffusivity (dashed line in fig. 26d) is clearly not capable to represent the experimental data. From this investigation, for ethane in DDR-I, the diffusivity at zero loading and parameter λ are found to be $D_{c=0} = 1.8 \times 10^{-13}\,\mathrm{m^2 s^{-1}}$ and $\lambda = 0.87$, respectively, with the latter corresponding to an increase of D about a factor of eight in the observed range of intracrystalline concentration.

4.1.3. Center-line analysis

For the mid-time regime of an adsorption process in crystals of cylindrical symmetry, i.e. when the diffusion fronts have met in the crystal center and reveal a parabolic concentration profile, two approximations can be made with respect to the diffusion equation (13):

$$\left(\frac{\partial c}{\partial r}\right)\bigg|_{r=0} = 0 \quad \text{and} \quad c(r) = c_{r=0} + \frac{1}{2}\frac{\partial^2 c}{\partial r^2} r^2. \tag{21}$$

With the second term on the right-hand side of eq. (13) becoming negligible small, the simplified relation is found as

$$\frac{\partial c}{\partial t} = 2D\frac{\partial^2 c}{\partial r^2}. \tag{22}$$

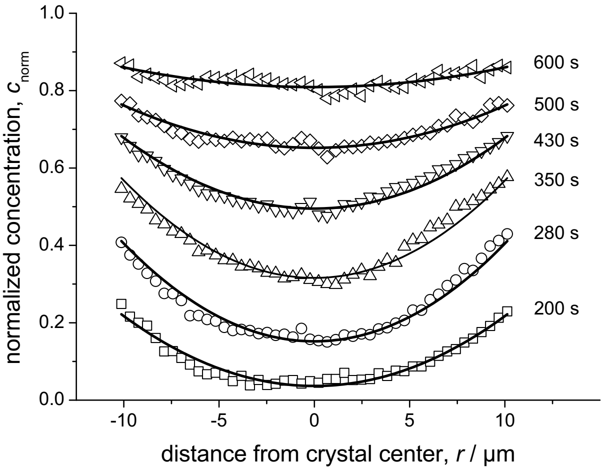

Figure 27: Center-line analysis of ethane in DDR-I. Only the center part of concentration profiles from fig. 26a are shown for the mid-time regime, i.e. when experimental profiles (opened symbols) reveal parabolic shape and can be fitted by $c(r) = c(0) + \alpha\, r^2$ (solid lines).

From eq. (22), with only two parameters, both to be obtained easily from IFM concentration profiles, the concentration-dependent diffusivity can be calculated. $\frac{\partial c}{\partial t}$ is found from the change of concentration at $r = 0$ in time and $\frac{\partial^2 c}{\partial r^2}$ from the parabolic fit of the profiles in that center region. The thus derived diffusivities are shown in fig. 28 as full stars, together with data obtained by methods previously described in secs. 4.1.1 and 4.1.2.

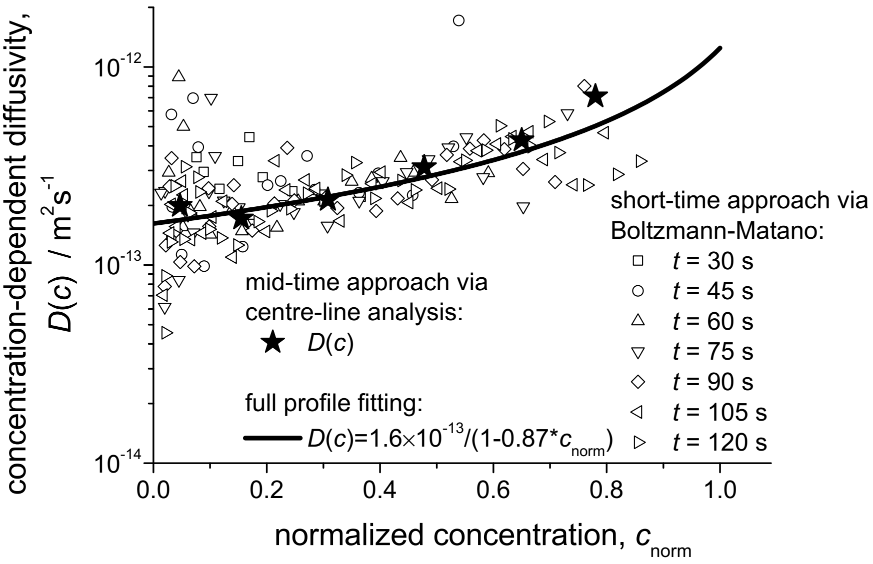

Figure 28: Proving coincidence of different methods to obtain $D(c)$. The opened and filled symbols result from the Boltzmann-Matano-approach by using eq. (20) and center-line analysis via eq. (22), respectively. The solid line is indeed no fit of these data points but an independent way of accessing $D(c)$, viz. by numerically fitting the concentration profiles using a concentration-dependent diffusivity.

From the good agreement of all three methods given in fig. 28, for ethane in DDR-I and the pressure step from 0 to 230 mbar, the diffusivity is found to be $D(c) = 1.6 \times 10^{-13}\,\mathrm{m^2 s^{-1}} \,/\, (1 - 0.87\, c_{\mathrm{norm}})$. In addition, this result proves the correctness of the different mathematical models applied and provides a useful toolbox for a more detailed comparison of diffusivities of different sorbate species in varying samples of DDR type zeolites.

For a very quick order of magnitude estimate of the overall diffusivity (without paying attention to its concentration-dependence), also in cases of pronounced $D(c)$ dependence the easily obtained uptake curve may be fitted using eq. (15). This yields, for the present example of ethane in DDR-I, $D = 2.5 \times 10^{-13}\,\mathrm{m^2 s^{-1}}$, which is still in reasonable good agreement with the more sophisticated and accurate ways of data processing.

4.1.4. Deviations from cylindrical symmetry

In the previous sections, any deviations from cylindrical symmetry of the DDR crystals were unattended. However, from fig. 22, a pronounced hexagonal crystal shape is found. The question arises, whether the concentration profiles are identical in x- and y-direction. A first indication of such differences is obtained by the short-time analysis, especially in fig. 26d, where the diffusion front of ethane in DDR-I seems to be faster (i.e. shifted to the right) in y-direction, compared to the x-direction. However, the differences were small and the overall diffusivity could be obtained by averaging over both directions. To check this behavior for different systems, fig. 29 provides the very same short-time analysis about the progress of diffusion fronts for ethane in DDR-II (fig. 29a) and propene in DDR-I (fig. 29b).

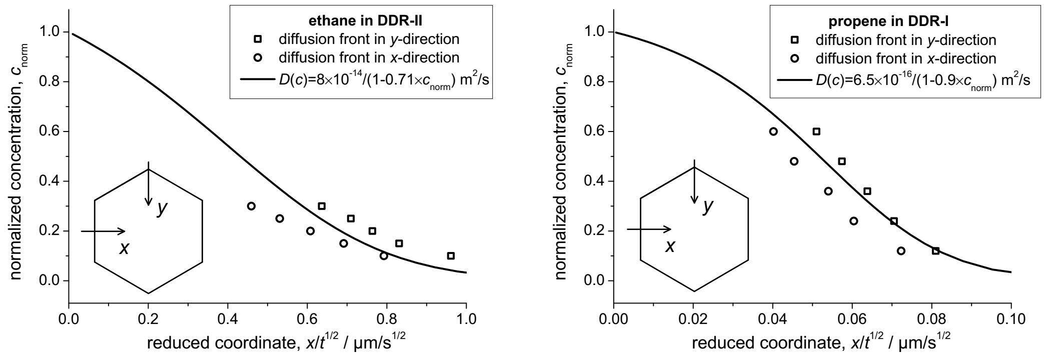

(a) ethane in DDR-II

(b) propene in DDR-I

Figure 29: Comparing the progress of diffusion fronts in DDR zeolites in x- and y-direction. Together with fig. 26d, for three different systems the apparent faster uptake in y-direction is found.

However, the here presented data do not indicate any diffusion anisotropy. As predicted by the structure of zeolite framework type DDR and confirmed by different ways of data analysis, cylindrical symmetry is found for these samples. This is fortified, in particular, by the application of center-line analysis in sec. 4.1.3. The difference at very short times can be explained to result from different surface-to-volume ratios at the vertices (y-direction) and the ridges (x-direction) of the crystal. For an ideal hexagonal prism, this factor is $1/\cos 30° = 2/\sqrt{3} \approx 1.15$, which is also quantitatively in reasonable good agreement with the experimental observation. Hence, the total flux through the crystal surface is slightly higher at the vertices, which leads to the apparent fast diffusion front in y-direction. The intracrystalline diffusion is, however, not found to reveal any anisotropic behavior. The diffusion fronts, changing from initially hexagonal shape to cylindrical symmetry at intermediate times, are presented in the appendix A.4.1.

4.2. Diffusion Study of Small Hydrocarbons

This section makes use of the former described methods of analyzing two-dimensional concentration profiles of cylindrical symmetry obtained by means of interference microscopy. As good agreement of all mathematical approaches could be shown in fig. 28, only the most convenient way of calculating diffusivities will be applied. In the following sections, three different topics are addressed: the comparison between three different DDR host materials (as introduced in tab. 5) using ethane as probe molecule in the subsequent sec. 4.2.1, the variation of different small hydrocarbons as sorbate species in DDR-II in sec. 4.2.2, and a brief summary and overview about diffusivities obtained by other methods in literature in sec. 4.2.3. The work presented here has in part been presented in ref. [115]. Furthermore, the single-component experiments will provide the basis for investigating binary mixtures in DDR zeolites by IFM in sec. 4.3.

4.2.1. Comparing three different DDR host materials

For this comparative study of different samples of DDR zeolites, we were kindly provided with three different samples of high-silica ZSM-58, notably varying in crystal size (tab. 5). The procedure of synthesis of the so-called DDR-I sample is described in ref. [115], whereas further details on the synthesis of DDR-II and DDR-III are proprietary. However, XRD experiments on all three samples confirmed their DDR structure. To reveal possible differences between these samples, ethane was chosen as a probe molecule in the investigations by means of interference microscopy. Due to its convenient uptake time of 10 to 30 minutes (depending on the crystal size), a larger number of adsorption-desorption cycles could be run and, nevertheless, an adequate number of concentration profiles were obtained in the short-time stage of the experiments.

As a very first result, all three samples provided homogeneous crystals of high quality. This concerns the crystal size, which deviates only by 1 to 2 µm, and also the uptake curves for ethane. The latter was found to coincide, within the crystals of a certain batch, with respect to the kinetics and to the overall (unnormalized) IFM signal, which is correlated to the equilibrium concentration multiplied by the crystal height. This proof of reproducibility is, in the following and especially when comparing different hydrocarbons, taken advantage of in the sense of having to perform other types of experiments only once.

One-dimensional concentration profiles of ethane in DDR-I, -II and -III, obtained from cuts in the x-direction of the two-dimensional IFM profiles, are shown in fig. 30. The shape of these profiles is in comparably good agreement. The scatter in fig. 30b and 30c is found to be slightly larger, which results from the speckled crystal surface and the small crystal size, respectively. The possibility of determining diffusivities is, however, unaffected.

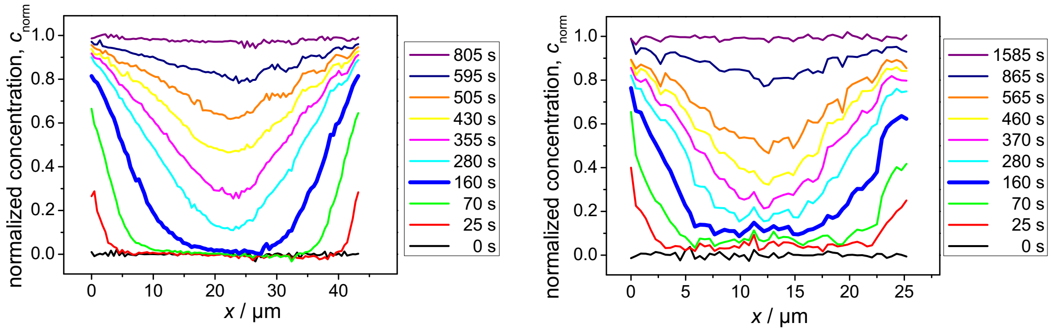

(a) DDR-I

(b) DDR-II

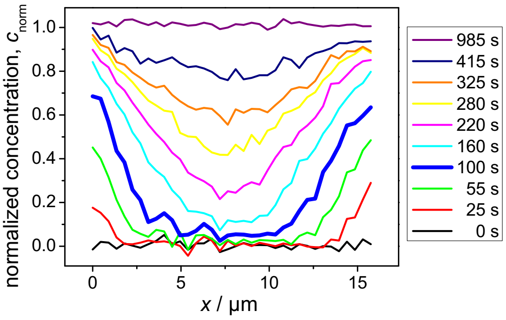

(c) DDR-III

Figure 30: One-dimensional concentration profiles of ethane in DDR-I, -II and -III, following a pressure increase from 0 to 210 mbar. Using the reported isotherm in ref. [35], for this pressure step, the equilibrium concentration is 3.50 molecules per unit cell.

According to the different approaches to derive information on the transport parameters (sec. 4.1), concentration-dependent intracrystalline diffusivities are obtained from these concentration profiles. Tab. 6 and its graphical presentation in fig. 31 provide an overview about these data. Again, no indications of significant surface barriers are found. The apparent slower increase of boundary concentrations in fig. 30b and 30c, which is usually an indication of transport resistances at the surface, can solely be related to the larger black areas resulting from tilted side faces for DDR-II and -III, compared to DDR-I (see fig. 22).

The main finding of the reported diffusivities for ethane in DDR-I, -II and -III is the observation that the absolute value of D for DDR-I is larger compared to the other samples by a factor of approximately two and three. However, the concentration dependence is found to be almost identical, as shown in the $D(c)$ plot in fig. 31.

sample		$\boldsymbol{D}_{\mathbf{c=0}}$ / m^{2}s^{-1}	$\boldsymbol{\lambda}$
DDR-I	(i)	1.8×10^{-13}	0.87
	(ii)	1.5×10^{-13}	0.95
	(iii)	1.6×10^{-13}	0.87
	(iv)	2.5×10^{-13}	0
DDR-II	(ii)	5.0×10^{-14}	0.67
	(iii)	6.1×10^{-14}	0.71
	(iv)	1.5×10^{-13}	0
DDR-III	(ii)	3.5×10^{-14}	0.80
	(iv)	6.3×10^{-14}	0

Table 6: Concentration-dependent diffusivities of ethane (0 to 210 mbar) in three different samples of zeolite DDR using the Fujita model $D(c) = \frac{D_{c=0}}{1-\lambda\cdot c}$ (eq. (19)). The values are obtained by (i) short-time analysis, (ii) center-line analysis, (iii) full-profile fitting and (iv) fitting of the integral uptake curve. The latter provides concentration-independent diffusivities ($\lambda = 0$).

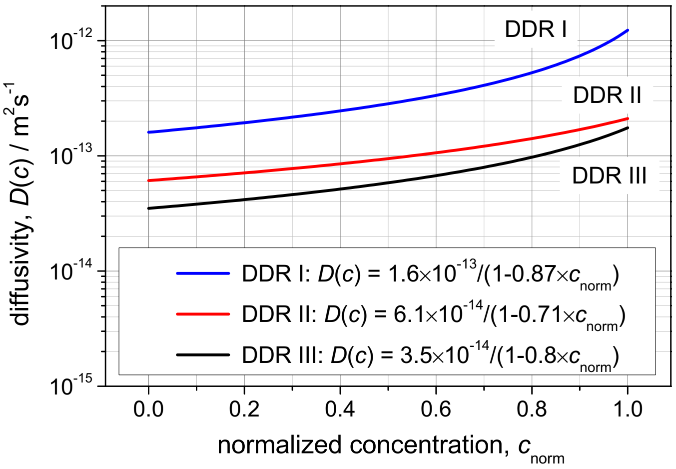

Figure 31: Concentration dependence of D for ethane in DDR-I, -II and -III, following the numbers given in tab. 6.

Besides the differences in the diffusivities, already the very shape of the concentration profiles in fig. 30 reveals distinct deviations regarding a certain detail, namely the presence or absence of an increase of concentration in the center part of the crystal before the diffusion fronts meet. For this purpose, $t_{1/2}$ is introduced as the time when the crystal has reached half of the equilibrium loading for the applied pressure step. It is known for particles of cylindrical symmetry that the first statistical moment of molecular uptake, M_1 [8,66,117], a common measure for the time constant of the sorption process, is

$$M_1 = \int_0^\infty \left(1 - \frac{m_t}{m_\infty}\right) \mathrm{d}t = \frac{R^2}{8D}. \tag{23}$$

From numerical calculations using eq. (15), the time $t_{1/2}$ can be found as

$$t_{1/2} \approx \frac{1}{2} M_1 = \frac{R^2}{16D}. \tag{24}$$

This time was chosen due to the fact that, at time $t_{1/2}$, the diffusion fronts have just not yet met in the crystal center. The theoretically obtained value for the concentration $c(r = 0, t_{\mathrm{exp.}})$, using eqs. (24) and (14), is 0.035. In tab. 7, the center concentrations at times $t_{\mathrm{exp.}}$, as close as possible to $t_{1/2}$, are given for the ethane uptake in DDR-I, -II and -III. For DDR-I, this number is, regarding the uncertainty of 0.01 to 0.02, in perfect agreement with the prediction. Hence, for this very sample, the assumption of no diffusion in axial direction is verified. However, in the case of DDR-II and DDR-III, the corresponding values are 0.12 and 0.06, respectively, which reveal a significant increase in the center concentration (bold blue profiles in figs. 30b and 30c, see also appendix A.4.2).

	calculated $t_{1/2}$	**$t_{\mathrm{exp.}}$**	**$c(r = 0,\ t_{\mathrm{exp.}})$**
DDR-I	169 s	160 s	0.02
DDR-II	152 s	160 s	0.12
DDR-III	99 s	100 s	0.06

Table 7: Tracing crystal imperfections in DDR-II and -III. From the concentration profiles given in fig. 30, the concentrations in the crystal center, $c(r = 0, t_{\mathrm{exp.}})$, is extracted at times $t_{\mathrm{exp.}}$. This is as close as possible to the calculated times $t_{1/2}$ at which the whole crystal has reached half of the equilibrium loading. The corresponding profiles are indicated in bold blue.

From this analysis, both samples DDR-II and DDR-III are suggested to allow mass transport also in axial directions, which, in the case of perfect crystals, should not occur. However, as the effect is rather small compared to the diffusion fronts running from the side faces to the inside, the impact on the overall uptake process is negligibly small. Thus, the samples can still be found to show cylindrical symmetry, justifying the mathematical treatment for obtaining diffusivities.

In fact, it is very well possible to relate both findings to each other: the decreased overall kinetics and the increasing center concentration at short times. If there are crystal imperfections, new pathways for diffusion (here in axial direction) may be formed while, at the same time, other windows might be blocked. Such counterintuitive behavior has been reported for MOF Zn(tbip) [52], which posses a large number of blocked entrances and, yet, notable options for the sorbate species to hop between the ideally linear channels, and also for LTA type zeolites [75], which reveal faster overall uptake after a post-synthesis treatment forming additional layers on top of the outer surface.

Observing discrepancies between diffusion coefficients for different samples of identical host structure is indeed not unusual. Even small deviations of the porous host material, which are not significant for structural analysis by XRD, are found to cause diffusivities to vary over orders of magnitude, e.g. in zeolite LTA [118] or MFI [119]. A factor of about three between $D_{c=0}$, as found for the comparison of the zeolite ZSM-58 samples DDR-I, -II and -III in this work, can, therefore, be referred to as quite moderate - especially regarding the dramatic change of sorbate mobilities about which shall be reported in the subsequent sec. 4.2.2.

4.2.2. Comparing different guest molecules

In this section, different small hydrocarbons are investigated with respect to their adsorption and desorption kinetics in the sample DDR-II. From tab. 1 on page 6 in the introduction about diffusion under confinement, the critical molecular diameters of methane, ethylene, ethane and propylene, are given as 0.34, 0.35, 0.37 and 0.43 nm, respectively. These diameters correspond to the smallest cylinders circumscribing the molecules favorable equilibrium conformation using an effective hydrogen diameter of 0.166 nm [35]. Having in mind the window diameter of the DDR eight-membered rings of 0.37 nm, diffusivities of the mentioned sorbate species are clearly expected to vary significantly.

(a) *Methane in DDR-II*

With the current setup of interference microscopy, the applicable gas phase pressures are limited and should not exceed ambient pressure, i.e. 1 bar. However, in this region, methane as a sorbate species in DDR zeolites is only weakly adsorbed at room temperature [108] and is, certainly, still in the Henry-regime (loading ∝ pressure). Together with an only small change of the refractive index caused by the comparably small methane molecule, the overall IFM signal is quite low and the concentration profiles are caused to show a certain degree of noise. One way to overcome this problem is to average over data points in the two-dimensional concentration profile which have the same distance r from the crystal center and, hence, from the symmetry axis. Following this approach, the IFM concentrations $c(x, y, t)$ are transformed to $c(r, t)$, with a notably higher signal-to-noise ratio. Fig. 25 in sec. 4.1.1 shows this way of data treatment, which, by fitting the thus derived concentration profiles with the ideal diffusion model in particles of cylindrical symmetry, eq. (14), also allows to obtain diffusion coefficients for this host-guest system. For methane in DDR-II, a value of $D = 0.96 \times 10^{-12}\,\mathrm{m^2s^{-1}}$ is found, which fits the experimental data for both adsorption and desorption.

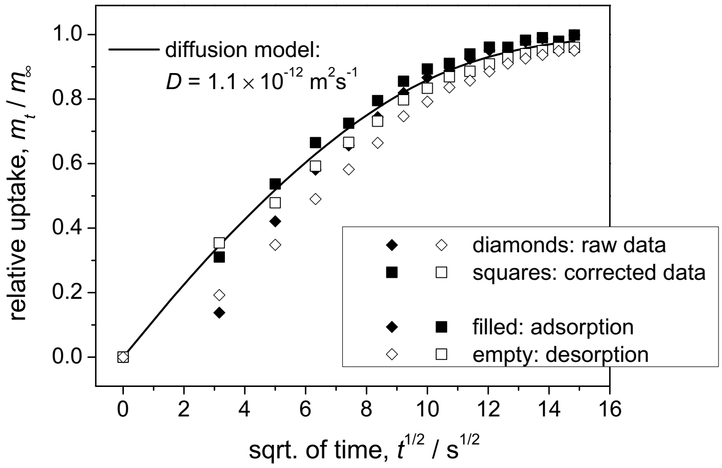

Figure 32: Integral uptake and release curves for methane in DDR-II following a pressure step from 0 to 800 mbar (or the corresponding one from 800 to 0 mbar for desorption). The corrected data (squares) are obtained from raw data (diamonds) by assuming that 20 % of the crystal volume is unseen by IFM and rapidly filled. Adsorption (filled symbols) and desorption (empty symbols) are found to coincide and confirm, thereby, that the diffusivity is independent of concentration.

These concentration profiles in the $c(r, t)$ form, however, exhibit two difficulties: (i) close to the crystal center, i.e. at $r \approx 0$, the number of data points to be averaged is very small, and (ii) at the outer areas of the crystal, i.e. at $r \approx R$, there are deviations from ideal cylindrical symmetry (due to the hexagonal crystal shape) and, in addition, unaccessible black areas close to the side faces (see fig. 22). Therefore, even with much smoother concentration profiles, fitting the $c(r, t)$ data is not expected to yield the most accurate D values. Both problems of this approach are overcome by, instead, taking the average over all available data points of the individual crystal under study, i.e. by following the integral uptake curve as shown in fig. 32. The outer shell of the crystal, which is unaccessible by means of IFM, is taken care of by the assumption that 20 % of the crystal, which are rapidly filled, are not comprised in the raw data. The thus obtained corrected data (squares) are in good agreement with the calculated solid line for the diffusion model (eq. (15)) using a diffusivity of $D = 1.1 \times 10^{-12}\,\mathrm{m^2s^{-1}}$. In this presentation of uptake against square root of time, the short-time approximation $\frac{m_t}{m_\infty} \propto \sqrt{t}$ [66] is confirmed.

The concentration-dependence of methane was already addressed by both previously described ways of processing the experimental data and found to be negligibly small. This is, additionally, suggested by the attempt of performing the center-line analysis as described in sec. 4.1.3. Here, the parameter λ of the Fujita model, determining the concentration dependence $D(c)$ as $D(c) = \frac{D_{c=0}}{1-\lambda\cdot c}$ (eq. (19)), was found to be approximately 0.1. This corresponds to an increase in D of about 10 %, which is, however, smaller than the expected uncertainty for the obtained diffusivity of $D_{c=0} = 6 \times 10^{-13}\,\mathrm{m^2s^{-1}}$. Indeed, the much more trustworthy numbers obtained from the fitting of averaged profiles and the comparison of the integral uptake curve to the diffusion model, $D = 0.96 \times 10^{-12}\,\mathrm{m^2s^{-1}}$ and $D = 1.1 \times 10^{-12}\,\mathrm{m^2s^{-1}}$, respectively, are in good agreement with data from literature (see tab. 8 in sec. 4.2.3).

(b) *Ethane in DDR-II*

In the previous sec. 4.2.1, ethane was applied to study and compare the three different DDR samples, among them DDR-II. The diffusivity was found to notably depend on the intracrystalline concentration. With an increase of loading from initially 0 to 3.5 molecules per unit cell [35], induced by a change of gas phase pressure from 0 to 210 mbar, the diffusivity raised by a factor of three to four. This behavior, higher sorbate mobilities at higher pore fillings, is well-known and reported for various nanoporous host-guest systems [8]. In addition, the present work revealed indications for crystal imperfection as mass transport in axial direction was observed which, in the ideal DDR structure, should not occur. However, the overall uptake of ethane in DDR-II is dominated by the regular diffusion pathways in the x-y-plane, with a limiting diffusivity of $D_{c=0} = 6 \times 10^{-14}\,\mathrm{m^2s^{-1}}$.

(c) *Ethylene in DDR-II*

When compared to ethane, ethylene reveals a slightly smaller critical molecular diameter due to its double bound and the thus resulting conformation. Even though this difference in the critical molecular diameter is only about 0.02 nm (see tab. 1), the effect on the mobility of the sorbate species is well detectable by IFM. The limiting diffusivity at low loadings, $D_{c=0}$ is by a factor of two smaller. As a most convenient (accurate and quick) approach, the center-line analysis is applied (fig. 33) and yields $D_{c=0} = 1 \times 10^{-13}\,\mathrm{m^2s^{-1}}/(1 - 0.8 \times c)$.

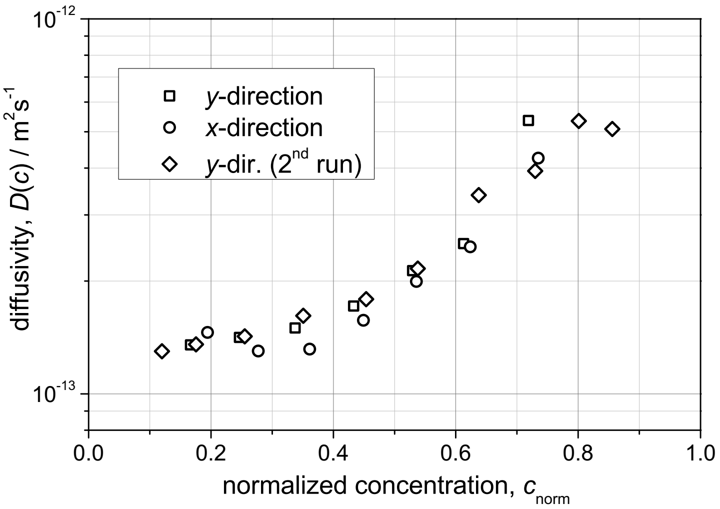

Figure 33: Concentration-dependent diffusivity $D(c)$ of ethylene in DDR-II obtained by center-line analysis (see sec. 4.1.3) after increasing the surrounding gas phase pressure from 0 to 210 mbar. The center-line analysis was performed in two perpendicular directions (x and y) and, as well, after a second run of the same experiment.

In addition to the well known increase of diffusivity with concentration, fig. 33 presents good agreement between the $D(c)$ values obtained in different directions perpendicular to each other, viz. x and y. This nicely demonstrates that the previously described deviations from ideal cylindrical symmetry (sec. 4.1.4) vanish when looking at the crystal center at mid times, rather than at the outer crystal areas at short times. Therefore, even in the case of hexagonally-shaped crystals, within the DDR host structure the diffusion pattern is clearly found to provide cylindrical symmetry. Hence, the application of the center-line calculation is justified.

As a second way of data processing, fitting the integral uptake and release curves was chosen. With eq. (15), unfortunately, the model is not capable of tracing a concentration dependence of the intracrystalline diffusivity. However, by comparing the values of adsorption and desorption, viz. 3.0 and $1.6 \times 10^{-13}\,\mathrm{m^2s^{-1}}$, respectively, also this method confirms the $D(c)$ relation. Both values are found to be in between $D_{c=0}$ and $D_{c=1}$ from center-line analysis. The kinetics, being slower for desorption than for adsorption, is reasonable, since the mass transport through the outer shell of the crystal is crucial. For desorption, this region has lower sorbate concentrations and, therefore, reduced mobilities and particle fluxes. In contrast, during adsorption, the outer crystal shell is rapidly filled to the equilibrium concentration, which allows higher guest mobilities and an overall faster uptake process.

This reasonable behavior of diffusivities, obtained from integral uptake and release curves, to lie in the range of concentration-depend values obtained by the other methods, was also found for different sorbate species and DDR samples in sec. 4.2.3.

(d) *Propylene in DDR-II*

The largest molecule considered in our diffusion studies with DDR-II was propylene, which, from the chosen way of calculating critical molecular diameter, has a size of 0.43 nm. This is already larger than the diameter of the DDR eight-membered ring windows with diameters of the elliptical pores of 0.36 nm × 0.44 nm. However, following literature reports on notable propylene uptake at even low pressures [120], also IFM experiments are performed. As the corresponding C3 alkane, propane, is not found to enter the DDR host system, there are attempts towards separation processes between these light olefins and paraffins [106, 107]. In fig. 34, one-dimensional IFM concentration profiles of propylene in DDR-II are shown.

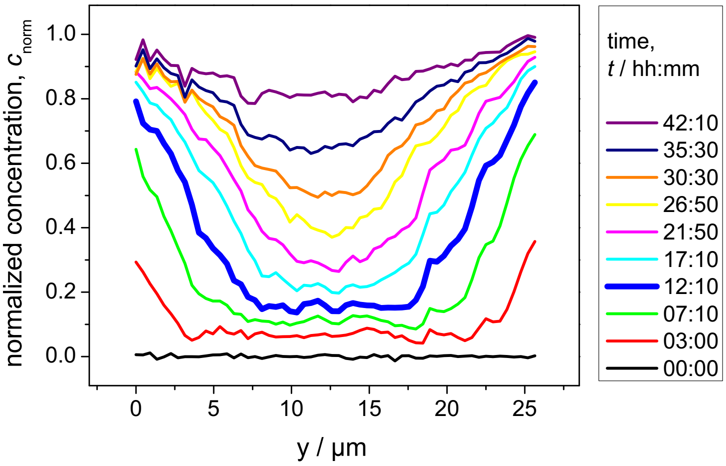

Figure 34: Concentration profiles of propylene uptake in DDR-II along y-direction. Corresponding to a pressure increase from 0 to 25 mbar, the loading raised to 3.46 molecules per unit cell [35]. The bold blue profile at t = 12 h represents approximately half of the overall equilibrium loading.

Also from this graph, the previously investigated crystal imperfections (see sec. 4.2.1) become immediately apparent: The bold blue profile, roughly taken at the time of half crystal filling $t_{1/2}$, reveals significant uptake in the crystal center ($r = 0$ at appr. $y = 13\,\mu\text{m}$) before the diffusion fronts from the side faces meet in this region. Here, the center concentration $c(r = 0, t_{\text{exp.}} \approx t_{1/2}) = 0.15$ is found to even exceed the value of 0.12 obtained for ethane in the same host material DDR-II (tab. 7).

Even though the overall uptake is quite strong (3.46 molecules per unit cell after increasing the pressure to 25 mbar as obtained from the isotherm reported in ref. [35]), the adsorption and desorption kinetics of propylene in DDR-II is dramatically slower compared to the previous sorbate species. From fitting the integral uptake and release curves, diffusivities of 1.0×10^{-15} and $3.0 \times 10^{-16}\,\mathrm{m^2s^{-1}}$, respectively, are found. Trying to determine concentration-dependent diffusivities by means of short-time or center-line analysis was omitted for this sample (but performed for DDR-I, see tab. 8), since these approaches shall be corrupted by the influence of mass transport in axial direction. The thus derived $D(c)$ values would not yield any accurate insight beyond the knowledge of D from the uptake and release curves.

4.2.3. Summarizing & comparing data with literature

To conclude this comparative study on the diffusivity of different small hydrocarbons in DDR zeolites, the previously collected data (together with additional experiments) are presented in fig. 35 and listed in tab. 8. While the former only contains experimental data using the sample DDR-II, the latter also shows diffusivities obtained from DDR-I. As found and discussed in sec. 4.2.1, there is a factor of about three between the two different samples. Regarding the large number of samples, sorbate species and methods of data analysis, not for every set of experiment all calculations were performed.

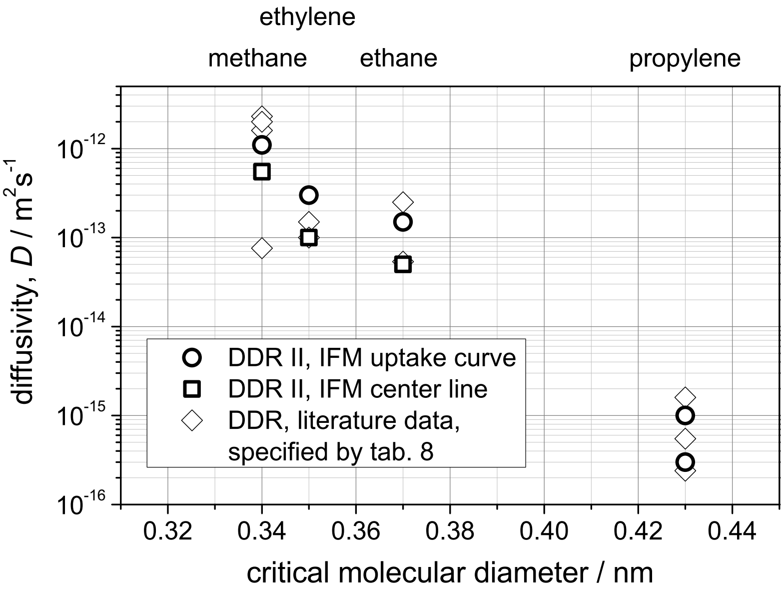

Figure 35: Comparison of diffusivities of different sorbate species in zeolite ZSM-58 of framework type DDR. References to literature data are given in tab. 8.

	DDR-I		**DDR-II**		**Literature**
	D_0 / m^2s^{-1}	λ	D_0 / m^2s^{-1}	λ	D_0 / m^2s^{-1}
Methane	(iv) 1.1×10^{-12}	0	(ii) 6×10^{-13}	0.1	2.3×10^{-12} ZLC [111] 1.7×10^{-12} FR [8] 2×10^{-12} MD [109] 1.6×10^{-12} NMR [121] 8×10^{-14} Membr. [108]
			(iii) 9.6×10^{-13}	0	
			(iv) 1.1×10^{-12}	0	
Ethylene	(ii) 2.6×10^{-13}	0.57	(ii) 1.0×10^{-13}	0.80	1.0×10^{-13} ZLC [116] 1.5×10^{-13} NMR [121]
	(iv) 3.3×10^{-13}	0	(iv) 1.6×10^{-13}	0	
	(iv) 5.1×10^{-13}	0	(iv) 3.0×10^{-13}	0	
Ethane	(i) 1.8×10^{-13}	0.87	(ii) 5.0×10^{-14}	0.67	2.5×10^{-13} ZLC [116]
	(ii) 1.5×10^{-13}	0.95	(iii) 6.1×10^{-14}	0.71	
	(iii) 1.6×10^{-13}	0.87	(iv) 1.5×10^{-13}	0	
	(iv) 2.5×10^{-13}	0			
Propylene	(i) 6.5×10^{-16}	0.9	(iv) 3.0×10^{-16}	0	5.0×10^{-16} Grav. [120] 0.2 to 1.6×10^{-15} Breakthrough [107]
	(iv) 1.4×10^{-15}	0	(iv) 1.0×10^{-15}	0	

Table 8: Comparing diffusivities of different sorbate species in DDR-I and DDR-II obtained from IFM experiments (this work) and various literature data. The variety of experimental methods include zero length column (ZLC), frequency response (FR), molecular dynamics simulation (MD), (pulsed field gradient) nuclear magnetic resonance (NMR), membrane permeation (Membr.), gravimetric uptake (Grav.) and breakthrough experiments. The IFM data were derived by (i) short time analysis, (ii) center-line analysis, (iii) full-profile fitting and (iv) fitting of the integral uptake curve. Where two diffusivities for integral uptake curve fitting are given, the higher value corresponds to the adsorption step, the slower one to desorption.

The large number of experimental data on the diffusivities of small hydrocarbons in DDR zeolites (fig. 35 and tab. 8) allows four conclusions to be drawn:

(a) Crystals of cylindrical symmetry have shown to provide new ways of determining transport parameters of adsorption and desorption processes from the two-dimensional concentration profiles obtained by means of interference microscopy. After their introduction in sec. 4.1, these different methods of data processing are found to be in good agreement for the investigated systems of small hydrocarbons in DDR-I, -II and -III.

(b) The finding of differences between the three different samples with respect to the diffusivity of ethane was shown in sec. 4.2.1. Besides having slower uptake and release kinetics, the samples DDR-II and -III were found to reveal mass transport in axial directions. Both can be discussed to result from crystal imperfections, which, in principle, may simultaneously block certain diffusion pathways (in the x-y-plane causing lower D values) and open new ones (in observation direction, leading to an increase of $c(r = 0)$ before the diffusion fronts met in the crystal center). Such differences for the same material being synthesized in different labs with different synthesis conditions are not surprising. With a factor of about three between the diffusivity of ethane in DDR-I and DDR-II/-III, this effect is comparably small.

(c) A much more pronounced variation of uptake and release kinetics was found by changing the sorbate species in sec. 4.2.2. Here, methane, ethane, ethylene and propylene were applied to study adsorption and desorption in DDR zeolites. By exceeding the theoretical window diameter of the DDR framework, an overall variation of the diffusivity by more than three orders of magnitude is observed.

(d) Finally, a detailed comparison of diffusivities reported in literature by using many different experimental and computational methods were found to be in good agreement with the IFM data of this work. In fact, except for the data of membrane permeation (reporting notably lower diffusivities), the differences were only about a factor of three, which is, as mentioned, just the difference between materials of varying origin. Therefore, in contrast to many other nanoporous host systems, which reveal significant differences when measured by different techniques [8], zeolites of framework type DDR provide a coherent picture of intracrystalline diffusion. However, it is only micro-imaging by interference microscopy that allows to follow a range of more than three orders of magnitude in D, as well as yielding direct access to the transport parameter by using the fundamental equations of mass transport.

4.3. Mixture Experiments: Retrieving Two-Component Data

So far, uptake and release kinetics of sorbate molecules in microporous zeolites of framework type DDR have been investigated. However, except for gas storage, all applications of micro- and mesoporous materials deal with mixtures of at least two different components. Therefore, the question of mixture diffusion is of common interest. Especially the mutual interaction and influence of different species inside of the porous matrix is by far not trivial. Different components will most likely act competitively regarding the available intracrystalline adsorption space (in the case of DDR zeolites the large cages) and might also mutually influence their diffusivities. When applied to binary mixtures, micro-imaging by IR microscopy has already proven to yield important new insights into these interactions. To distinguish between the component of the sorbate phase, IRM follows the change of different IR bands for different molecules, if necessary by using a deuterated component. This has already been shown for mixtures of linear and branched alkanes in silicalite-1 [19, 122] and is going to be further exploited in ongoing work [44].

Even if the temporal and spatial resolution of interference microscopy is notably better (10 s and 0.5 µm compared to 120 s and 2.7 µm for IRM), the overall IFM signal is just the sum of both components' effect on the local change of the refractive index of the host-guest system. There is no trivial way of distinguishing between the different sorbate species and, therefore, to obtain local concentrations $c_1(x, y, t)$ and $c_2(x, y, t)$. For the first time, the present work shows a certain scenario, where this problem can be overcome by differentiating two components by the large differences in their diffusivities. The mixture to be addressed in the sample DDR-II is ethane and CO_2. The procedure includes an in-detail investigation on the single-component adsorption of ethane and CO_2, separately adsorbed in DDR-II (sec. 4.3.1), the application of *ideal adsorbed solution theory* (IAST) to the binary mixture of both (sec. 4.3.2) and, finally, the determination of local concentrations $c_1(x, y, t)$ and $c_2(x, y, t)$ from the IFM profile of the change of the optical path length in observation direction (sec. 4.3.3). With this procedure (being limited to certain mixtures), some additional experimental data on the binary adsorption of methane and CO_2 by IRM is presented in sec. 4.3.4. The results of this work are presented in the publication [123].

4.3.1. Single component experiments compared to literature

The first step towards the analysis of binary mixtures in nanoporous materials by means of interference microscopy is a detailed study of the single-component adsorption. It is essential to obtain the factor of proportionality between the intracrystalline particle concentration of the individual species and the thus caused change of refractive index and the change of phase difference, the latter being measured from the interference pictures. This relation, as introduced by eq. (3) on page 10, is now used with the well-defined factor of proportionality k_i, where i indicates either ethane or CO_2:

$$\Delta(\Delta\varphi^{(L)}(t)) = k_i\,\Delta c_i(t). \tag{25}$$

In eq. (25), the material properties of zeolite ZSM-58 are already taken care of. With no significant mass transport in observation direction, the integral over local concentrations $\Delta c(x, y, z, t)$ may be transferred to the averaged concentration $\Delta c_i(t)$ of the sorbate species i.

To obtain the values k_i, two steps are needed: For the single crystal under study, a sequence of smaller pressure steps has to be performed by IFM. This *isotherm* (in units of the change of phase difference, i.e. in rad) is then, as the second step, correlated with an isotherm of the same host-guest system at equal temperature, which is in the case of ethane and CO_2 available from different publications [108, 121]. Fig. 36 pictures this procedure, yielding $k_{\mathrm{ethane}} = 8.08\,\mathrm{rad/(mol/kg)}$ and $k_{\mathrm{CO_2}} = 5.07\,\mathrm{rad/(mol/kg)}$ as factors of proportionality between the IFM signal and local concentration. This allows, by following eq. (25), the determination of true concentrations from the two-dimensional IFM concentration profiles.

However, certain sources for uncertainties have to be considered. As an important cross-check, several other single crystals of the DDR-II sample have been tested. With only a few percent deviation, the results were in good agreement, which allows to use the k values also for different crystals of this sample. An additional uncertainty arises from this comparison with literature isotherms, as the applied materials do not have the same origin. The deviations of sorption properties are, however, usually not as pronounced as it is the case for diffusivities and transport resistances. Thus, we may assume for the different DDR samples to show identical sorption behavior.

Regarding a binary mixture of ethane and CO_2, in first-order approximation we may assume the refractive index (and, hence, the IFM signal) to change with increasing loading of the sorbate species as

$$\Delta(\Delta\varphi^{(L)}(t)) = k_{\mathrm{ethane}}\,\Delta c_{\mathrm{ethane}}(t) + k_{\mathrm{CO_2}}\,\Delta c_{\mathrm{CO_2}}(t). \tag{26}$$

This is an important first step towards the determination of local concentrations $c_{\mathrm{ethane}}(t)$ and $c_{\mathrm{CO_2}}(t)$ from the IFM concentration profiles. However, so far, it is still impossible to obtain two unknown quantities out of just one measured variable.

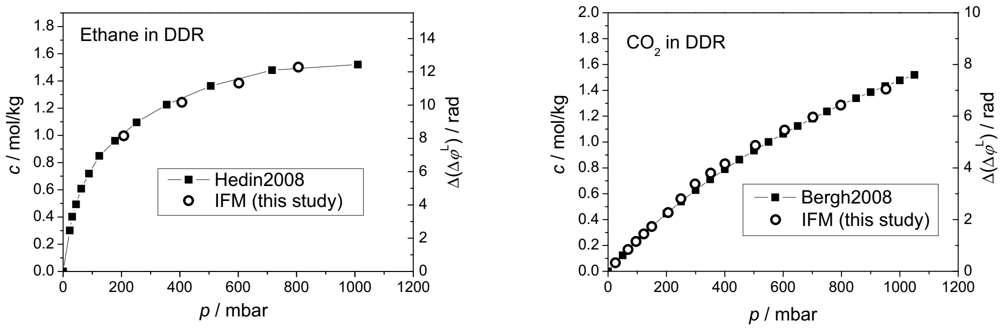

(a) ethane isotherms

(b) CO_2 isotherms

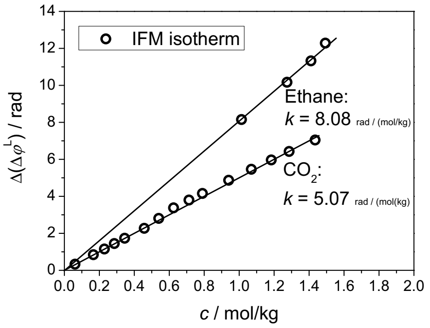

(c) determination of k_i

Figure 36: For ethane (a) and CO_2 (b) in DDR at room temperature, the IFM isotherms are compared with and scaled to the literature isotherms reported in refs. [121] and [108], respectively. In (c), the IFM signal at pressure p is plotted against the concentration c (from literature isotherms) at this pressure, yielding the desired k values as the slope of the linear regression.

4.3.2. IAST predictions and IFM results for binary mixtures

The second step in the analysis of binary mixture adsorption by means of interference microscopy is the application of the so-called *ideal adsorbed solution theory* (IAST). This theory, developed by Myers and Prausnitz in 1965 [124], is still considered as the most useful general approach to address binary mixtures [36]. IAST allows to calculate mixture isotherms, i.e. partial loadings of the components as well as the total loading, depending on the gas phase pressures. These loadings are numerically calculated, with the single-component isotherms as input parameters. In the present work, the procedure of ref. [36] is followed, which is based on the spreading pressure π obtained by integrating the Gibbs isotherm. Using a self-created short *Mathematica*-script, from the two single-component isotherm parameters and the given partial pressures in the binary mixtures, the individual intracrystalline concentrations can easily be calculated. In the sense of IAST, solutions are ideally adsorbed when there is no interaction of the different sorbate species except for those interactions being present also in the single-component adsorbed phase. In ref. [125], for DDR zeolites, for the loadings here considered, good agreement of the IAST predictions to grand canonical monte carlo simulations is shown.

	mixture	p_{total}	p_i (mbar)	
	CO_2 : ethane	(mbar)	CO_2	ethane
(1)	1:1	396	202	194
(2)	2:1	575	384	191
(3)	3:1	796	601	195

Table 9: Settings of three different ethane-CO_2 mixtures in DDR. The partial pressure of ethane is kept constant, while the amount of CO_2 varies for the three uptake experiments performed.

However, the most important feature of the binary mixture of ethane and CO_2 in DDR zeolites is not the applicability of IAST, but the large difference in uptake rates. As reported in this study and in literature [116], for ethane it is found $D_{\text{ethane}} = 1.5 \times 10^{-13}\,\text{m}^2\text{s}^{-1}$. In contrast, CO_2 is at least three orders of magnitude faster, and, thus, much too fast to be observed within the initial 10 s of the first IFM concentration profile. From NMR experiments, the diffusivity is known to be approximately $D_{CO_2} = 7 \times 10^{-10}\,\text{m}^2\text{s}^{-1}$ [112].

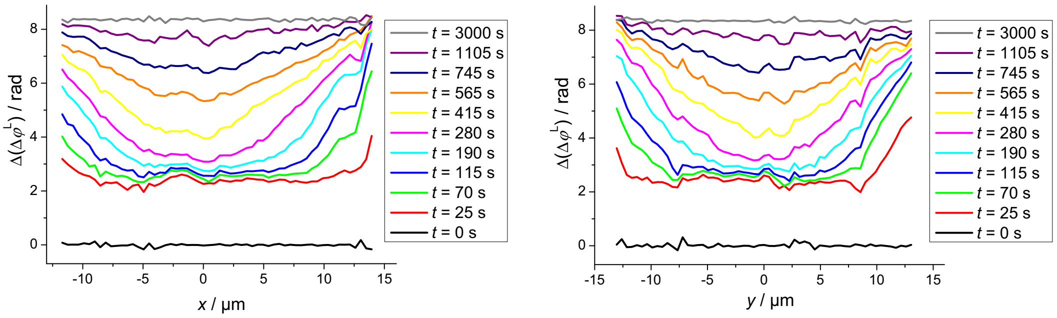

(a) (b)

Figure 37: Profiles in x- and y-direction ((a) and (b)) following the adsorption of a binary mixture, consisting of CO_2 and ethane in the ratio of 1:1 in the gas phase (experiment (1) in tab. 9). The total pressure is about 400 mbar.

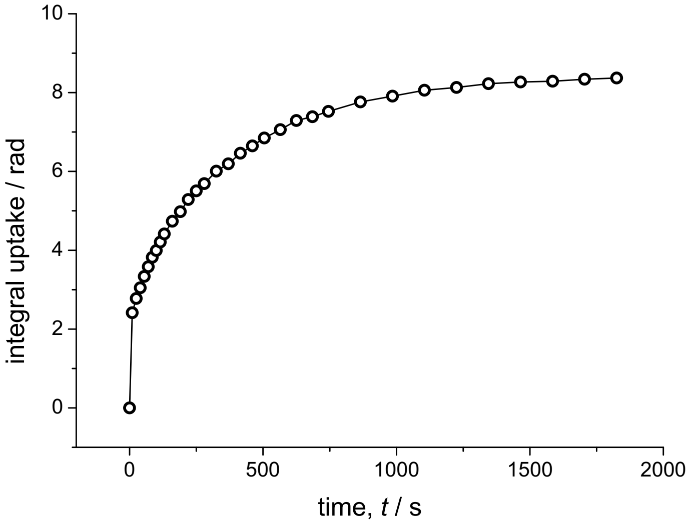

Figure 38: Uptake curve for mixture adsorption of CO_2 and ethane, corresponding to the IFM profiles shown in fig. 37.

Fig. 37 shows the IFM profiles of the 1:1 mixture of ethane and CO_2 in x- and y-direction. For the purpose of correlating the IFM signal to intracrystalline concentrations, the profiles are given in their unnormalized form, i.e. in rad. Both sorbate species cause an increase of this IFM signal proportionally to their local concentrations, as given by eq. (26). The integral uptake curve of this experiment is presented as fig. 37. Both images show the experimental data of experiment (1) in tab. 9. Two other gas phase compositions with the same partial pressure of ethane but a higher amount of CO_2 are also studied.

The experimental finding of this first mixture experiment is a very fast and steep increase of the IFM signal at the first profile measured. The averaged height of this increase, as seen in the uptake curve in fig. 38, is about 2.3 rad. In the profiles of fig. 37, this jump is represented by the red line taken 25 s after the adsorption of the mixture is initiated. The origin of this first change in the IFM signal is clearly correlated to a homogeneous distribution of sorbate molecules throughout the whole crystal, rather than just an increase of concentration at the crystal side faces. The obvious explanation is that CO_2 is rapidly equilibrating throughout the whole crystal, long before the first profile is measured. From the previously mentioned diffusivity of about $D_{CO_2} = 7 \times 10^{-10}\,m^2s^{-1}$ and by using eq. (23), a time constant of less than 0.1 s can be estimated. The profiles following after this first increase (and as well the corresponding data points in the uptake curve) are suggested to result from ethane molecules entering the crystal on top of the already present CO_2.

A strong confirmation of this explanation about the CO_2 molecules rapidly equilibrating can be found in tab. 10. Here, the intensity or height of the first increase of homogeneous CO_2 concentration is found to perfectly coincide with the value one would obtain for a single-component CO_2 uptake of the same (partial) pressure p_{CO_2} as applied in the mixture. This agreement is obtained for all three mixture experiments, in which the first increase of CO_2 increases with increasing CO_2 partial pressure. This prediction for CO_2 uptake is simply the value of the single component isotherm (ref. [108]) at pressure p_{CO_2} multiplied by the k_{CO_2} factor from fig. 36c.

	$\boldsymbol{p_{CO_2}}$	**CO_2: prediction**		**CO_2: exp.** (rad)
	mbar	mol/kg	rad	1st jump of ads. profiles
(1)	202	0.450	2.3	2.3
(2)	384	0.765	3.9	4.0
(3)	601	1.065	5.4	5.6

Table 10: Analyzing the initial, very fast CO_2 uptake. For the three mixture experiments (1), (2) and (3), as introduced in tab. 9, the measured fast CO_2 uptake (last column) is compared with predictions for single-component adsorption of the same (partial) pressure of CO_2. The correlation of intracrystalline concentration (mol/kg) and IFM signal (rad) for the CO_2 prediction is based on eq. (25) using k_{CO_2} obtained in fig. 36.

In principle, this demonstrates how two different sorbate species can be distinguished when there is difference of a several orders of magnitude between their uptake rates: The fast component is rapidly equilibrating and the slower one will follow a common adsorption behavior, with a diffusion front running from the side faces to the center of the DDR crystal. However, the true transient concentration profiles, separated for both components, will not be obtained by simply assuming the CO_2 concentration to be constant and the ethane concentration to be correlated to all of the IFM signal beyond the first step. Clearly, as soon as ethane molecules enter the porous matrix, part of the previously adsorbed CO_2 will be pushed out. Finally, an equilibrium conformation will be reached with, most probably, a somewhat lower CO_2 fraction than estimated from the first adsorption step.

Now, further analysis is benefiting from IAST calculations: From the single-component adsorption isotherms for CO_2 and ethane (i.e. the dual-side Langmuir parameters of these isotherms) [108, 121], the expected equilibrium concentrations for CO_2 and ethane are obtained, together with the total loading. These numbers are then transfered from concentrations in mol/kg to an expected IFM signal intensity in rad, again by using the k factors of fig. 36c. Together with experimental IFM values for the overall adsorption and desorption equilibrium signal and the height of the initial fast decrease during desorption experiments, the IAST predictions are given in tab. 11.

	IAST equilibrium prediction						**IFM experimental**		
	CO_2		ethane		total		Ads	Des (1^{st} jump & eq.)	
	mol/kg	rad	mol/kg	rad	mol/kg	rad	rad	rad	rad
(1)	0.22	1.12	0.94	7.60	1.16	8.71	8.4	1.2	7.9
(2)	0.42	2.13	0.85	6.87	1.27	9.00	8.9	2.0	8.6
(3)	0.62	3.14	0.79	6.38	1.42	9.53	9.7	3.2	9.8

Table 11: IAST predictions and IFM results for mixture adsorption in DDR zeolites. Using the partial pressures of ethane and CO_2 of the three experiments (1), (2) and (3), tab. 9, the IAST model is applied to calculate equilibrium concentrations in mol/kg, and, by following eqs. (25) and (26), the IFM signal to be expected. The experimental IFM data are shown to the right, including the overall values for adsorption and desorption equilibrium and the fast first jump during desorption (next-to-last column).

From the large number of data given in tab. 11, two pairs of columns should be compared: First, the IAST prediction for CO_2 (calculated to IFM signal intensity in rad), second column, is found to perfectly coincide with the next-to-last column of IFM experiments, showing the values of the rapid first desorption step. Clearly, from the agreement of these data for all three experiments, we are able to correlate the first desorption step to the whole CO_2 fraction rapidly leaving the crystal, just as it is the case for the adsorption process. In addition, the IAST seems to well predict this CO_2 fraction in the equilibrium. The second pair of columns to be compared is the IAST prediction on the total loading and the correlated estimation on the IFM signal, and the experimental data on the IFM adsorption signal. Again, with good agreement and deviations below 5 %, this fortifies the IAST to be well predicting the equilibrium concentrations of this binary mixture in DDR zeolites.

4.3.3. Determining individual components' local concentrations

Finally, with a brief approach to extend the IAST calculations, true transient concentration profiles, separated for the two components ethane and CO_2, can be obtained. The high spatial and temporal resolutions of interference microscopy will be preserved, allowing further analysis of the mass transport of this binary mixture.

The second equation, which is needed for solving eq. (26) and obtaining the concentration of the two components, will be derived from the observation of CO_2 being significantly faster than ethane. Especially when compared to the time interval needed to obtain an IFM profile (typically 10 to 15 s), CO_2 is referred to be equilibrated. Therefore, the more generally obtained relation of intracrystalline concentration c and partial pressures in the gas phase p, namely

$$c_{\mathrm{CO_2}} = c_{\mathrm{CO_2}}(p_{\mathrm{CO_2}}, p_{\mathrm{ethane}}), \tag{27}$$

can be slightly modified to

$$c_{\mathrm{CO_2}} = c_{\mathrm{CO_2}}(p_{\mathrm{CO_2}}, c_{\mathrm{ethane}}). \tag{28}$$

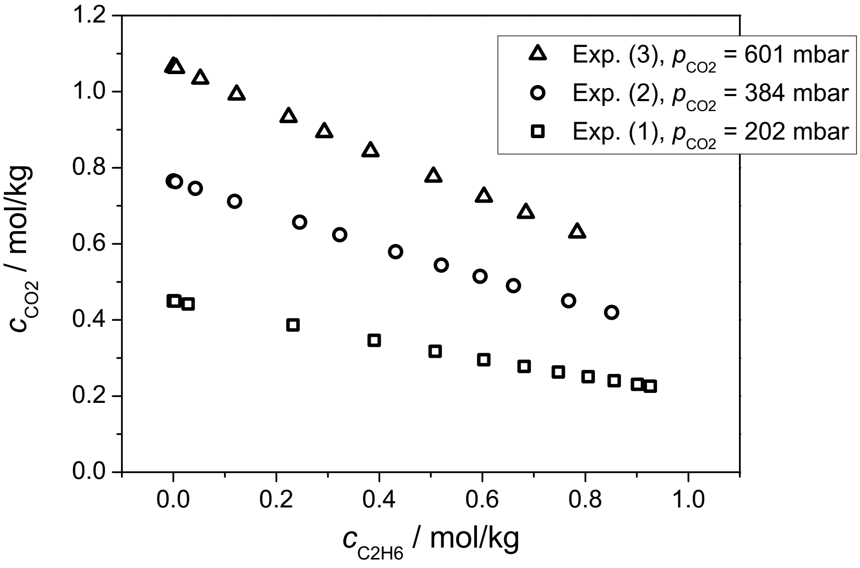

Figure 39: Dependence of $c_{\mathrm{CO_2}}$ on c_{ethane} in an adsorbed binary mixture in DDR zeolites obtained by numerical IAST calculations. The partial pressure of CO_2 is kept constant (at the values measured during experiments (1), (2) and (3), see tab. 9). The partial pressure of ethane increases from 0 to the value measured in the experiments. By doing so, the CO_2 concentration is found to decrease, starting from the concentration one would obtain for the single-component CO_2 adsorption. The end points for each experiment (highest c_{ethane}, lowest $c_{\mathrm{CO_2}}$) corresponds to the final equilibrium of the system as described in tab. 11.

Eq. (28) states that the local concentration of CO_2, $c_{\mathrm{CO_2}}$, is a function of the gas phase pressure of CO_2, $p_{\mathrm{CO_2}}$, and the local concentration of ethane, c_{ethane}.

Due to the difference in D of three orders of magnitude, the adsorbed CO_2 molecules do not *feel* the gas phase pressure of ethane, but, instead, form an (quasi-) equilibrium with the local concentration of ethane molecules (if already present). This still follows the concept of IAST, in which the spreading pressure π is kept constant. By setting the partial pressure of CO_2, p_{CO_2}, to be constant and only varying the partial pressure of ethane, p_{ethane}, numerical calculations of IAST allow to determine the dependence of eq. 28.

Fig. 39 presents the thus derived data. As expected, with increasing ethane concentration, CO_2 will be partly pushed out of the host system. With respect to eq. (28), this process is most reasonably found to show proportionality, i.e. the more ethane is present in the zeolite, the more CO_2 is pushed out. These data may now be fitted as

$$c_{CO_2} = A - B \times c_{\text{ethane}}, \tag{29}$$

where A is nothing else than the single-component concentration of CO_2 at the gas phase pressure of p_{CO_2}, and B the slope of this linear regression, denoting the ratio of overall CO_2 decrease and ethane increase for the individual experiment. By inserting eq. (29) into eq. (26), the intracrystalline concentration of ethane (and via eq. (29) also the one of CO_2) can immediately be obtained. The outcome of this concept is shown by fig. 40, which presents the intracrystalline concentration profiles of the two mixture components obtained from the IFM profile in fig. 37a.

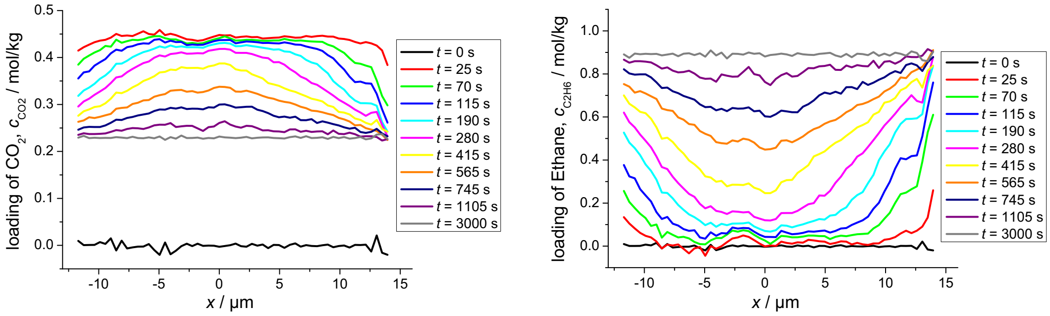

(a) CO_2 (b) ethane

Figure 40: Transient concentration profiles separated for the two mixture components, CO_2 and ethane. By combining eqs. (29) and (26) and using the parameters (k_i, A, B) obtained from single-component isotherms and IAST calculations, the two-component profiles could be retrieved from the IFM profile (fig. 37a) of experiment (1).

For the first time, such two-component data could be derived from an interference microscopy experiment of a binary mixture being adsorbed in a zeolite crystal. Fig. 40a demonstrates how the CO_2 concentration is rapidly increasing to the maximum of about 4.4 mol/kg at $t = 25$ s. Afterwards, as ethane enters the crystal from the side faces, CO_2 is seen to be pushed out again.

The integral uptake curve of this mixture adsorption can be obtained in two different ways: As eq. (29) exhibits a linear dependence of c_{CO_2} and c_{ethane}, it is possible to use the untreated uptake curve in fig. 38 and divide each data point into two values for ethane and CO_2. Alternatively, the concentration profiles of fig. 40 could be integrated (or averaged) over the whole two-dimensional crystal surface. Both procedures will lead to the graph shown in fig. 41.

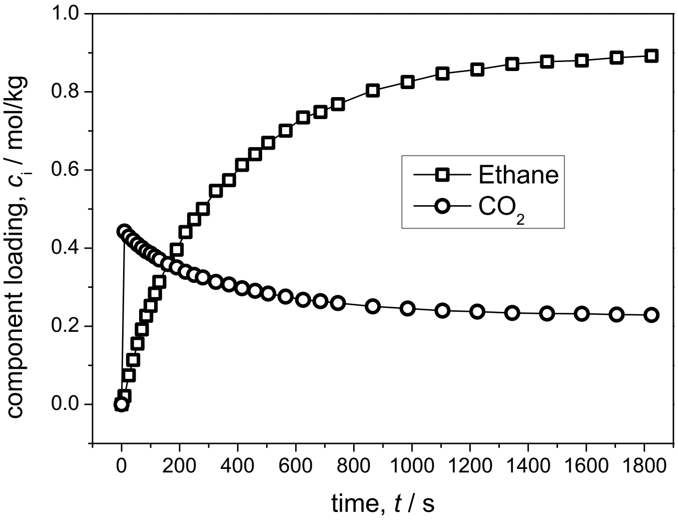

Figure 41: Uptake curve of two components from binary mixture adsorption. On the basis of the raw IFM uptake curve (fig. 38) or the already separated concentration profiles (fig. 40), these single-component loadings of CO_2 and ethane are derived. The graph shows the data of experiment (1) in tab. 9, i.e. a 1:1 mixture of CO_2 and ethane at a total pressure of about 400 mbar.

The uptake curve of the two different mixture components (fig. 41) shows the exponential-like behavior of ethane, and the already described process for CO_2. The latter follows a sharp increase to a value corresponding to the single-component loading of the same (partial) pressure of CO_2 and is afterwards found to decrease again. With the same treatment of experimental IFM data for all three considered mixtures, it is now possible to compare the kinetics of ethane depending on the presence of CO_2. The profiles and uptake curves for the experiments (2) and (3) are given in the appendix A.4.3.

In fig. 42, only the ethane fraction of the overall IFM signal are plotted and compared to the single-component experiment of the same ethane pressure. Regarding the fact that there are a few new sources of uncertainties introduced by the determination of the ethane fraction in the mixture experiments, the agreement of all four graphs can be referred to be very good. In fact, when using the diffusion model for a particle of cylindrical symmetry to fit these uptake curves (eq. (15)), within small deviations of about 10 to 20 %, the curves yield a diffusivity of about $D_{\text{ethane}} = 1.2 \times 10^{-13}\,\text{m}^2\text{s}^{-1}$.

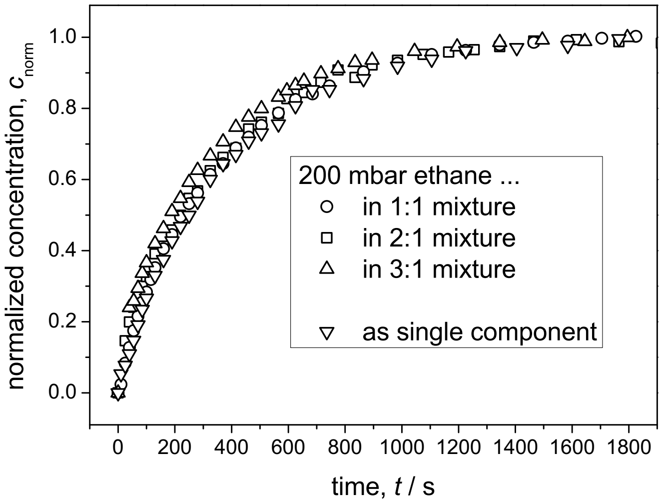

Figure 42: Comparison of ethane kinetics with varying presence of CO_2. Three mixture experiments (with equal partial pressure of ethane but increasing partial pressure of CO_2), see tab. 9, and the single component ethane uptake are listed.

This finding of an ethane diffusivity being unaffected by the amount of CO_2 present in the DDR zeolite, is also supported by ZLC experiments [116]. The discussion of this publication, especially that CO_2 and ethane are non-competitively adsorbed in DDR zeolites, is fortified by the present IFM investigations on this binary mixture.

However, the wealth of the intracrystalline concentration profiles separated for both components (fig. 40) can be even further exploited. From these profiles, particle fluces may be determined and, hence, the diffusion matrix (corresponding to the diffusion coefficient in single-component uptake) is accessible by a direct experimental approach. This is part of ongoing work and will be further investigated.

4.3.4. Complementary methane measurements

As a complementary measurement, mixtures of methane and CO_2 were investigated by means of IR microscopy. Even though the IR device provides a poorer temporal resolution when the focal plane array detector is applied to obtain spatially resolved profiles, in its integral mode, the IRM is notably faster compared to IFM. IR microscopy in the integral mode means that only a single element detector is used. It is focused on a single DDR crystal and follows the change of the corresponding IR bands after increasing the gas phase from vacuum to a well-defined ratio of methane and CO_2. The experimental conditions and IRM uptake curves of these experiments are shown in tab. 12 and fig. 43, respectively.

	gas mixture	$\boldsymbol{p}_{\textbf{total}}$	$\boldsymbol{p_i}$ (mbar)		$\boldsymbol{c}_{\textbf{total}}$	$\boldsymbol{c_i}$ (mol/kg)	
	$CO_2 : CH_4$	(mbar)	CO_2	CH_4	(mol/kg)	CO_2	CH_4
(1)	0:1	800	0	800	0.39	0	0.39
(2)	1:3.5	500	110	390	0.43	0.24	0.19
(3)	1:2	400	136	264	0.43	0.30	0.13

Table 12: Settings of three IRM experiments with different methane-CO_2 mixtures in DDR. The first, (1), corresponds to the single-component uptake of methane. In (2) and (3), additionally, CO_2 is present in the gas phase. The total loading, c_{total}, is kept constant.

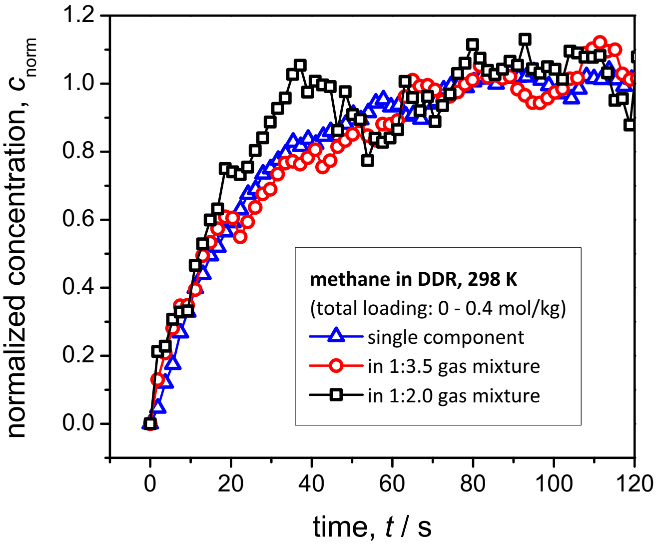

Figure 43: IRM uptake curve for mixture adsorption of CO_2 and methane. Blue, red and black symbols correspond to experiments (1), (2) and (3) of tab. 12, respectively.

So far, the results for IR measurements with methane and CO_2 do not reveal a significant enhancement of diffusivities, which is reported in ref. [111]. The approximate diffusivity of methane is, for this set of experiments, $D_{\text{methane}} = 2 \times 10^{-12}\,\text{m}^2\text{s}^{-1}$. For experiment (3), there might be indications of a tendency towards faster uptake, but due to the low loadings of methane in this pressure range, the increased noise does not allow an accurate quantitative analysis.

This short insertion of IR uptake experiments was chosen for two reasons: First, this gas mixture of methane and CO_2 is of greater interest in terms of industrial applications compared to the model system of ethane and CO_2 addressed before by means of interference microscopy. As both, methane and CO_2, are the major components of natural gas reservoirs, separation is a key question. In principle, separation can be done by microporous materials such as DDR zeolites, that is why the CO_2-methane-DDR system is investigated in literature [109–112]. Unfortunately, the current setup of interference microscopy is not capable of obtaining concentration profiles faster than every 10 s. Assuming the difference in diffusivities of methane and CO_2 to be still large enough (there are at lease two orders of magnitude in between), with a faster recording every 0.5 s, the previously described separation of the two components local concentration should as well be possible. Suggestions on how to modify the IFM setup are already in discussion and, as also other system would benefit, this will clearly be in the focus of future work.

5. Summary

The aim of this thesis was the application of recently established micro-imaging by interference microscopy to monitor transient, intracrystalline concentration profiles of high spatial and temporal resolution. This experimental basis allowed the in-depth study of mass transport phenomena in nanoporous materials. Even though the present work is of fundamental character, the relevance of several addressed topics to large-scale applications is unquestionable. This especially concerns surface barriers, deviations from perfect crystallographic structure and mixture experiments.

The experimental setup of interference microscopy has not seen any significant modifications in the course of this study. However, many of the computational tools to analyze, correct and process the experimental data were either newly-created or notably improved. Only these self-written algorithms enabled the high picture quality of e.g. the phase transition of benzene in silicalite-1. In addition, the efficiency in data treatment, achieved by automated computer programs, allowed the large number of experiments with DDR zeolites to be performed and evaluated with varying both samples and sorbate species.

Zeolite ZSM-5 (MFI)

Two different types of silicalite-1 samples, the all-silica form of ZSM-5 with framework type MFI, were investigated. For the first time, trying to identify diffusion anisotropy between x- and y-direction, crystals of the rounded-boat morphology could be measured from three different observation directions. However, even by using long, rod-like sorbate molecules, for which a significant difference of D_x and D_y is predicted due to the preference of straight channels rather than the zig-zag ones, no indications of such behavior were obtained. The conclusion of this set of experiments is that, also in the case of rounded-boat shaped silicalite-1, a twinned structure of the individual crystal has to be expected. Only by 90° rotated subunits, the finding of equal diffusivities in x- and y-direction can be explained.

Following the uptake of isobutane in silicalite-1 crystals of the coffin-like shape, an in-depth study of surface permeabilities, i.e. transport resistances at the outer crystal surface, was carried out. It is certainly one of the major strengths of interference microscopy that, by carefully investigating the increase of the surface or boundary concentration, surface permeabilities may quantitatively be analyzed. In the present case, a peculiar increase of surface barriers, which have previously been described to arise from residual water molecules forming impenetrable surface layers, was further examined. The calculated surface permeabilities were found to decrease by more than two orders of magnitude. However, with these surface permeabilities being ideally constant after an exposure of the crystal to a mild water atmosphere, the nature of surface changes in this system has to be reconsidered. Nevertheless, as surface barriers are crucial for many applications of nanoporous materials, the strong benefits of diffusion measurements by interference microscopy are emphasized.

In another case study, phase transitions of benzene in silicalite-1 were investigated. There are reports on both changes of the sorbate phase and shifts of the zeolite framework, especially its symmetry, available in literature for higher loadings of benzene above the threshold of four molecules per unit cell. The fact that the subunits of the MFI crystals under study are mutually rotated by 90° and that IFM is primarily sensitive to the optical density rather than to the concentration has provided us with the unique option to record the spatial-temporal dependence of phase transitions in nanoporous host-guest systems.

Zeolite ZSM-58 (DDR)

Zeolite ZSM-58 of framework type DDR has never before been investigated by micro-imaging techniques. Owing to the cylindrical symmetry of the crystals, which ideally do not allow any mass transport in axial direction, new ways of determining diffusivities were theoretically described and checked by interference microscopic uptake and release experiments. Reasonably good agreement could be observed for all approaches, including short-time analysis following the Boltzmann-Matano model, center-line analysis at intermediate times, numerical calculations for full profile fitting applying the solutions of the diffusion equation and fitting of the uptake and release curves to the diffusion model. Except for the latter technique, these methods of data processing yield concentration-dependent diffusivities, which, for the investigated systems, were found to follow the Fujita model.

The thus derived tools to analyze two-dimensional concentration profiles were then applied to study differences between three different samples of zeolite ZSM-58 and, as well, between different sorbate species. This yields a factor of about three between the diffusivities of ethane in the DDR specimens, which may result from different ways of zeolite synthesis or post-treatment. Two out of three samples revealed measurable uptake in observation direction. Together with slower uptake and release of guest molecules, these crystals are strongly suggested to be deviating from ideal structure. Crystal imperfections are, in this sense, at the same time responsible for mass transport in axial direction and transport resistances in the common diffusion pathways. The comparison of different sorbate species revealed differences of more than three orders of magnitude in their diffusivity. A strong correlation to the critical molecular diameter was found and, hence, a coherent picture of diffusion in DDR zeolites is presented.

Finally, on the basis of these single-component experiments, also the uptake and release of a binary mixture was studied by interference and IR microscopy. The former is, due to the working principle of following changes in the refractive index of the host-guest system, unable to distinguish between different sorbate species. However, by using the *ideal adsorbed solution theory* and isotherms reported in literature, in the case of CO_2 and ethane the two-component data could be retrieved. This was made possible by the huge difference of their diffusivities by more than three orders of magnitude. This new approach yielded local concentrations, separated for CO_2 and ethane, with the preserved high spatial and temporal resolution. In this mixture, ethane was not found to be influenced by the presence of CO_2.

Conclusions

This work demonstrates the remarkable insights of micro-imaging by interference microscopy into mass transport in nanoporous materials. Several case studies, applying two different types of zeolites, are shown and described with new findings, unattainable by other methods. This particularly concerns the direct and simultaneous recording of surface permeabilities and diffusivities, the observation of phase transitions and the adsorption of binary mixtures. Especially the latter field will be in the focus of future work: The two-dimensional profiles of local concentrations, separately available for both components, may yield the elements of the diffusion matrix, the equivalent to the diffusion coefficient in binary systems.

Like a magnifying glass, interference microscopy allows to directly follow intracrystalline concentrations. Regarding the numerous applications of nanoporous materials in chemical industry and irrespective of the broad variety of other techniques applied to investigate the processes involved, IFM is found to notably contribute to the understanding of diffusion and host-guest interactions.

References

[1] R. Brown. *Phil. Mag.* **4** (1828) 161–173.

[2] A. Fick. *Ann.Phys. Chem.* **94** (1855) 59–86.

[3] J. Dalton. *A new system of chemical philosophy.* London (1808).

[4] A. Einstein. *Ann. Phys.* **17** (1905) 549–560.

[5] A. Einstein. *Ann. Phys.* **19** (1906) 371–381.

[6] M. Smoluchowski. *Ann. Phys.* **21** (1906) 756–780.

[7] R. M. Barrer. *J. Chem. Soc.* (1948) 2158–2163.

[8] J. Kärger, D. M. Ruthven and D. N. Theodorou. *Diffusion in Nanoporous Materials.* Wiley-VCH (2012).

[9] S. Brunauer, P. Emmett and E. Teller. *Journal of the American Chemical Society* **60** (1938) 309–319.

[10] S. Lowell, J. E. Shields, M. A. Thomas and M. Thommes. *Characterization of Porous Solids and Powders: Surface Area, Pore Size and Density.* Springer (2004).

[11] M. Thommes. *Chemie Ingenieur Technik* **82** (2010) 1059–1073.

[12] J. Kärger. *Leipzig, Einstein, Diffusion.* Leipziger Universitätsverlag (2007).

[13] G. Vogl. *Wandern ohne Ziel.* Springer (2007).

[14] D. Brockmann, L. Hufnagel and T. Geisel. *Nature* **439** (2006) 462–465.

[15] D. Brockmann, V. David and A. M. Gallardo. In *Diffusion Fundamentals III.* Leipziger Universitätsverlag (2009).

[16] International bill tracking system "where's george?".
URL `http://www.wheresgeorge.com`

[17] L. Karwacki, M. H. F. Kox, D. A. M. deWinter, M. R. Drury, J. D. Meeldijk, E. Stavitski, W. Schmidt, M. Mertens, P. Cubillas, N. John, A. Chan, N. Kahn, S. R. Bare, M. Anderson, J. Kornatowski and B. M.Weckhuysen. *Nature Materials* **8** (2009) 959–965.

[18] H. Karge and W. Niessen. *Catal. Today* **8** (1991) 451–465.

[19] C. Chmelik and J. Kärger. *Chem. Soc. Rev.* **39** (2010) 4864–4884.

[20] U. Schemmert, J. Kärger, C. Krause, R. Rakoczy and J. Weitkamp. *Europhys. Lett.* **46** (1999) 204–210.

[21] U. Schemmert, J. Kärger and J. Weitkamp. *Microporous and Mesoporous Materials* **32** (1999) 101–110.

[22] U. Schemmert. *Interferenzmikroskopische Untersuchungen zur Moleküldiffusion in mikroporösen Materialien.* Ph.D. thesis, Universität Leipzig (2001).

[23] A. v. Cronstedt. *Akad. Handl. Stockholm* **17** (1756) 120–123.

[24] H. Li, M. Eddaoudi, M. O'Keeffe and O. M. Yaghi. *Nature* **402** (1999) 276–279.

[25] E. W. Thiele. *Ind. Eng. Chem.* **31** (1939) 916–920.

[26] M. Bastos-Neto, C. Patzschke, M. Lange, J. Möllmer, A. Möller, S. Fichtner, C. Schrage, D. Lässig, J. Lincke, R. Staudt, H. Krautscheid and R. Gläser. *Energy & Environmental Science* **8** (2012) 8294–8303.

[27] R. M. Barrer. *Diffusion in Polymers*, pages 165–217. Academic Press, London (1968).

[28] International zeolite association: Database of zeolite structures.
URL http://www.iza-structure.org/databases/

[29] S. Vasenkov, W. Böhlmann, P. Galvosas, O. Geier, H. Liu and J. Kärger. *J. Phys. Chem. B* **105** (2001) 5922–5927.

[30] S. Vasenkov and J. Kärger. *Microporous and Mesoporous Materials* **55** (2002) 139–145.

[31] D. M. Ruthven and S. Brandani. *Membrane Science and Technology* **6** (2000) 187–212.

[32] L. V. Rees and L. Song. *Membrane Science and Technology* **6** (2000) 139–186.

[33] L. Song and L. V. Rees. *Adsorption and Diffusion*, chapter Frequency response measurements of diffusion in microporous materials, pages 235–276. Springer (2008).

[34] F. Hibbe, V. R. R. Marthala, C. Chmelik, J. Weitkamp and J. Kärger. *J. Chem. Phys.* **135** (2011) 184201.

[35] W. Zhu, F. Kapteijn, J. A. Moulijn, M. C. den Exter and J. C. Jansen. *Langmuir* **16** (2000) 3322–3329.

[36] D. M. Ruthven. *Mol Sieves* **7** (2008) 1–43.

[37] D. Ruthven, R. Derrah and K. Loughlin. *Canadian Journal of Chemistry* **51** (1973) 3514–3519.

[38] H. J. V. Tyrrell and K. R. Harris. *Diffusion in Liquids.* Butterworth, London (1984).

[39] D. Ambrosini, D. Paoletti and N. Rashidnia. *Opt. Laser Eng.* **46** (2008) 852–864.

[40] H. Mehrer. *Diffusion in Solids.* Springer (2007).

[41] P. Callaghan. *Principles of NMR Microscopy.* Clarendon Press, Oxford (1991).

[42] R. Kimmich. *NMR Tomography, Diffusometry, Relaxometry.* Springer (1997).

[43] J. Kärger and W. Heink. *J. Magn. Reson.* **51** (1983) 1–7.

[44] T. Titze. *Bridging between micro- and macroscopic diffusion measurements by IR imaging.* Ph.D. thesis, University of Leipzig (in preparation).

[45] A. Lauerer. *Charakterisierung der Diffusion und Reaktion von Gastmolekülen in nanoporösen Materialien mittels Micro-Imaging.* Ph.D. thesis, University of Leipzig (in preparation).

[46] P. Kortunov, S. Vasenkov, C. Chmelik, J. Kärger, D. Ruthven and J. Wloch. *Chem. Mater.* **16** (2004) 3552–3558.

[47] P. Kortunov, C. Chmelik, J. Kärger, R. Rakoczy, D. Ruthven, Y. Traa, S. Vasenkov and J. Weitkamp. *Adsorption* **11** (2005) 235–244.

[48] P. Kortunov. *Rate Controlling Processes of Diffusion in Nanoporous Materials.* Ph.D. thesis, Universität Leipzig (2006).

[49] D. Tzoulaki, L. Heinke, W. Schmidt, U. Wilczok and J. Kärger. *Angew. Chem. Int. Ed.* **47** (2008) 3954–3957.

[50] D. Tzoulaki, W. Schmidt, U. Wilczok and J. Kärger. *Microporous and Mesoporous Materials* **110** (2008) 72–76.

[51] D. Tzoulaki. *Diffusion Studies on Microporous Materials by Interference Microscopy.* Ph.D. thesis, Universität Leipzig (2009).

[52] F. Hibbe, C. Chmelik, L. Heinke, S. Pramanik, J. Li, D. M. Ruthven, D. Tzoulaki and J. Kärger. *Journal of the American Chemical Society* **133** (2011) 2804–2807.

[53] F. Hibbe. *Micro Imaging Employed to Study Diffusion and Surface Permeation in Porous Materials.* Ph.D. thesis, University of Leipzig (2012).

[54] T. Binder, C. Chmelik, L. Heinke, F. Hibbe, J. Kärger, T. Titze and D. Tzoulaki. In *Diffusion Fundamentals III* (2009) pages 205–221.

[55] C. Chmelik, L. Heinke, R. Valiullin and J. Kärger. *Chemie Ingenieur Technik* **82** (2010) 779–804.

[56] G. T. Kokotailo, S. L. Lawton, D. H. Olson and W. M. Meier. *Nature* **272** (1978) 437–438.

[57] E. M. Flanigen, J. M. Bennett, R. W. Grose, J. P. Cohen, R. L. Patton, R. M. Kirchner and J. V. Smith. *Nature* **271** (1978) 512–516.

[58] J. Kärger. *J. Phys. Chem.* **95** (1991) 5558–5560.

[59] S. Fritzsche and J. Kärger. *J. Phys. Chem. B* **107** (2003) 3515–3521.

[60] L. Gueudré, T. Binder, C. Chmelik, F. Hibbe, D. M. Ruthven and J. Kärger. *Materials* **5** (2012) 721–740.

[61] C. Weidenthaler, R. X. Fischer, R. D. Shannon and O. Medenbach. *J. Phys. Chem.* **98** (1994) 12687–12694.

[62] O. Geier, S. Vasenkov, E. Lehmann, J. Kärger, U. Schemmert, R. A. Rakoczy and J. Weitkamp. *J. Phys. Chem. B* **105** (2001) 10217–10222.

[63] W. Schmidt, U. Wilczok, C. Weidenthaler, O. Medenbach, R. Goddard, G. Buth and A. Cepak. *J. Phys. Chem. B* **111** (2007) 13538–13543.

[64] C. Chmelik, A. Varma, L. Heinke, D. Shah, J. Kärger, F. Kremer, U. Wilczok and W. Schmidt. *Chem. Mater.* **19** (2007) 6012–6019.

[65] C. Shao, X. Li, S. Qiu, F.-S. Xiao and O. Terasaki. *Microporous and Mesoporous Materials* **39** (2000) 117–123.

[66] J. Crank. *The Mathematics of Diffusion.* Oxford University Press (1975).

[67] L. Heinke. *Mass Transfer in Nanoporous Materials: A Detailed Analysis of Transient Concentration Profiles.* Ph.D. thesis, Universität Leipzig (2009).

[68] L. Heinke and J. Kärger. *Physical Review Letters* **106** (2011) 1–4.

[69] C. Chmelik, F. Hibbe, D. Tzoulaki, L. Heinke, J. Caro, J. Li and J. Kärger. *Microporous and Mesoporous Materials* **129** (2010) 340–344.

[70] H. Fujita. *Textile Research Journal* **22** (1952) 757.

[71] L. Gueudré, N. Bats and E. Jolimaître. *Microporous and Mesoporous Materials* **147** (2012) 310–317.

[72] L. Zhang, C. Chmelik, A. N. C. van Laak, J. Kärger, P. E. de Jongh and K. P. de Jong. *Chem. Commun.* **42** (2009) 6424–6426.

[73] D. Tzoulaki, L. Heinke, H. Lim, J. Li, D. Olson, J. Caro, R. Krishna, C. Chmelik and J. Kärger. *Angewandte Chemie* **48** (2009) 3525–3528.

[74] A. F. Combariza and G. Sastre. *J. Phys. Chem. C* **115** (2011) 13751–13758.

[75] T. Binder, Z. Adem, C. B. Krause, M. Krutyeva, A. Huang, J. Caro and J. Kärger. *Microporous and Mesoporous Materials* **146** (2011) 151–157.

[76] S. J. Reitmeier, O. C. Gobin, A. Jentys and J. A. Lercher. *J. Phys. Chem. C* **113** (2009) 15355–15363.

[77] O. C. Gobin, S. J. Reitmeier, A. Jentys and J. A. Lercher. *J. Phys. Chem. C* **115** (2011) 1171–1179.

[78] D. Tzoulaki, L. Heinke, M. Castro, P. Cubillas, M. W. Anderson, W. Zhou, P. A. Wright and J. Kärger. *Journal of the American Chemical Society* **132** (2010) 11665–11670.

[79] P. V. Kortunov, L. Heinke, M. Arnold, Y. Nedellec, D. J. Jones, J. Caro and J. Kärger. *Journal of the American Chemical Society* **129** (2007) 8041–8047.

[80] R. Krishna and J. van Baten. *Chemical Engineering Journal* **140** (2008) 614–620.

[81] D. W. F. Brilman, W. P. M. van Swaaij and G. F. Versteeg. *J. Chem. Eng. Data* **46** (2001) 1130–1135.

[82] C. Gücüyener, J. van den Bergh, J. Gascon and F. Kapteijn. *Journal of the American Chemical Society* **132** (2010) 17704–17706.

[83] J. van den Bergh, C. Gücüyener, E. A. Pidko, E. J. M. Hensen, J. Gascon and F. Kapteijn. *Chemistry - A European Journal* **17** (2011) 8832–8840.

[84] A. Boutin, S. Couck, F.-X. Coudert, P. Serra-Crespo, J. Gascon, F. Kapteijn, A. H. Fuchs and J. F. Denayer. *Microporous and Mesoporous Materials* **140** (2011) 108–113.

[85] P. Serra-Crespo, E. Stavitski, F. Kapteijn, and J. Gascon. *RSC Advances* **2** (2012) 5051–5053.

[86] E. L. Wu, S. L. Lawton, D. H. Olson, A. C. Rohrman and G. T. Kokotailo. *The Journal of Physical Chemistry* **83** (1979) 2777–2781.

[87] H. van Koningsveld, F. Tuinstra, H. van Bekkum and J. C. Jansen. *Acta Cryst.* **B45** (1989) 423–431.

[88] C. G. Pope. *J. Phys. Chem.* **90** (1986) 835–837.

[89] F. Schüth. *J. Phys. Chem.* **96** (1992) 7493–7496.

[90] J. Caro, M. Noack, J. Richter-Mendau, F. Marlow, D. Petersohn, M. Griepentrog and J. Kornatowski. *Journal of Physical Chemistry* **97** (1993) 13685–13690.

[91] C.-K. Lee and A. S. T. Chiang. *J. Chem. Soc. Faraday Trans.* **92** (1996) 3445–3451.

[92] B. Mentzen and F. Lefebvre. *Materials Research Bulletin* **32** (1997) 813–820.

[93] L. Song and L. V. Rees. *Microporous and Mesoporous Materials* **35** (2000) 301–314.

[94] S. Sorenson, J. Smyth, M. Kocirik, A. Zikanova, R. Noble and J. Falconer. *Ind. Eng. Chem. Res.* **47** (2008) 9611–9616.

[95] O. Gobin, S. Reitmeier, A. Jentys and J. Lercher. *Microporous and Mesoporous Materials* **125** (2009) 3–10.

[96] R. Q. Snurr, A. T. Bell and D. N. Theodorou. *J. Phys. Chem.* **97** (1993) 13742–13752.

[97] H. Haken and C. Wolf. *Molekülphysik und Quantenchemie.* Springer (2006).

[98] L. Song, Z.-L. Sun, H.-Y. Ban, M. Dai and L. V. C. Rees. *Phys. Chem. Chem. Phys.* **6** (2004) 4722–4731.

[99] J. Kärger, T. Binder, C. Chmelik, F. Hibbe, H. Krautscheid, R. Krishna and J. Weitkamp. *Nature Materials* **submitted** (2013).

[100] H. Gies. *Zeitschrift für Kristallographie* **175** (1986) 93–104.

[101] E. Valyocsik (1987). US patent 4,698,217.

[102] S. Ernst and J. Weitkamp. *Chem.-Ing.-Tech.* **63** (1991) 748–750.

[103] A. J. Huth, J. M. Stueve and V. V. Guliants. *Journal of Membrane Science* **403** (2012) 236–249.

[104] D. M. Ruthven. *Chemie Ingenieur Technik* **83** (2011) 44–52.

[105] T. Tomita, K. Nakayama and H. Sakai. *Microporous and Mesoporous Materials* **68** (2004) 71–75.

[106] D. M. Ruthven and S. C. Reyes. *Microporous and Mesoporous Materials* **104** (2007) 59–66.

[107] J. Gascon, W. Blom, A. van Miltenburg, A. Ferreira, R. Berger and F. Kapteijn. *Microporous and Mesoporous Materials* **115** (2008) 585–593.

[108] J. van den Bergh, W. Zhu, J. Gascon, J. Moulijn and F. Kapteijn. *Journal of Membrane Science* **316** (2008) 35–45.

[109] S. E. Jee and D. S. Sholl. *Journal of the American Chemical Society* **131** (2009) 7896–7904.

[110] R. Krishna, J. van Baten, E. García-Pérez and S. Calero. *Chemical Physics Letters* **429** (2006) 219–224.

[111] A. Vidoni and D. Ruthven. *Microporous and Mesoporous Materials* **159** (2012) 57–65.

[112] B.-T. L. Bleken, K. P. Lillerud, T. Splith, A.-K. Pusch and F. Stallmach. *Microporous and Mesoporous Materials* **submitted** (2013).

[113] Y. Kumita, J. Gascon, E. Stavitski, J. A. Moulijn and F. Kapteijn. *Applied Catalysis A General* **391** (2011) 234–243.

[114] T. Binder, F. Hibbe, C. Chmelik, J. Kärger, A. Martinez-Joaristi, J. Gascon, F. Kapteijn and D. Ruthven. *Journal of Chemical Physics* **137** (2012) 164704.

[115] T. Binder, C. Chmelik, J. Kärger, A. Martinez-Joaristi, J. Gascon, F. Kapteijn and D. Ruthven. *Microporous and Mesoporous Materials* **accepted** (2013).

[116] A. Vidoni and D. M. Ruthven. *Ind. Eng. Chem. Res.* **51** (2012) 1383–1390.

[117] R. Barrer. *Zeolites and Clay Minerals as Sorbents and Molecular Sieves.* Academic Press, London (1978).

[118] D. M. Ruthven. *Microporous and Mesoporous Materials* **162** (2012) 69–79.

[119] H. Jobic. *Journal of Molecular Catalysis A: Chemical* **158** (2000) 135–142.

[120] D. H. Olson, M. A. Camblor, L. A. Villaescusa and G. H. Kuehl. *Microporous and Mesoporous Materials* **67** (2004) 27–33.

[121] N. Hedin, G. J. DeMartin, W. J. Roth, K. G. Strohmaier and S. C. Reyes. *Microporous and Mesoporous Materials* **109** (2008) 327–334.

[122] C. Chmelik, L. Heinke, J. van Baten and R. Krishna. *Microporous and Mesoporous Materials* **125** (2009) 11–16.

[123] T. Binder, C. Chmelik, J. Kärger and D. M. Ruthven. *Ind. Eng. Chem. Res.* **submitted** (2013).

[124] A. L. Myers and J. M. Prausnitz. *AIChE J.* **11** (1965) 121–127.

[125] R. Krishna and J. van Baten. *Chemical Physics Letters* **446** (2007) 344–349.

List of Figures

Picture Credits

Except for the following declarations, all figures, graphs and pictures of this work are self-created sketches or formatted experimental data. Figs. 1 and 5 are drawn and produced using "3D jmol" at the webpage of the structure commission of the international zeolite association [28]. The SEM pictures of zeolite ZSM-5 (fig. 7) and ZSM-58 (fig. 22) were kindly allocated by the provider of the corresponding materials.

List of Tables

A. Appendix

The appendix provides supporting material to several sections of this work. This includes, in particular, additional graphs and calculations on topics and experiments being only briefly mentioned in the main sections.

A.3.1. Orientation-dependent guest diffusion

In sec. 3.1, silicalite-1 crystals of the rounded-boat shape were measured in different observation directions. The given numbers for the diffusivity and surface permeability of 4-methyl-2-pentyne (tab. 2 on page 17) are based on the experimental data of fig. 44.

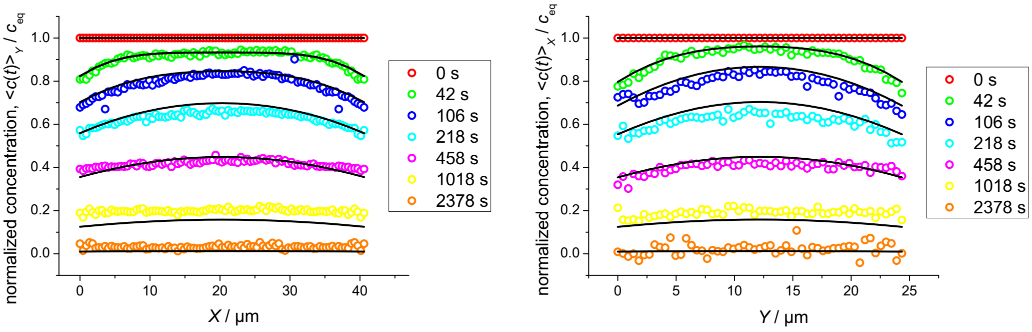

(a) (b)

Figure 44: Concentration profiles of 4-methyl-2-pentyne in X- and Y-direction ((a) and (b)), following the desorption process from 1 to 0 mbar. The black lines indicate the best fits to the experimental data using numerical calculations for the solution of the diffusion equation. The diffusivities and surface permeabilities are found to coincide in both directions, see tab. 2.

A.3.2. Surface barriers of zeolite silicalite-1

In sec. 3.2, growing surface barriers of silicalite-1 crystals were reported. As an additional presentation, fig. 45 illustrates the dramatic change not only in terms of increasing equilibration times (160 s compared to 3000 s), but also in the profile shape: Curved profiles with high surface concentrations indicate a diffusion-limited process (fig. 45a), while very flat profiles with slowly increasing surface concentrations reveal notable surface barriers (fig. 45b). The profiles were obtained from the second and fourth experiment of fig. 12b on page 21.

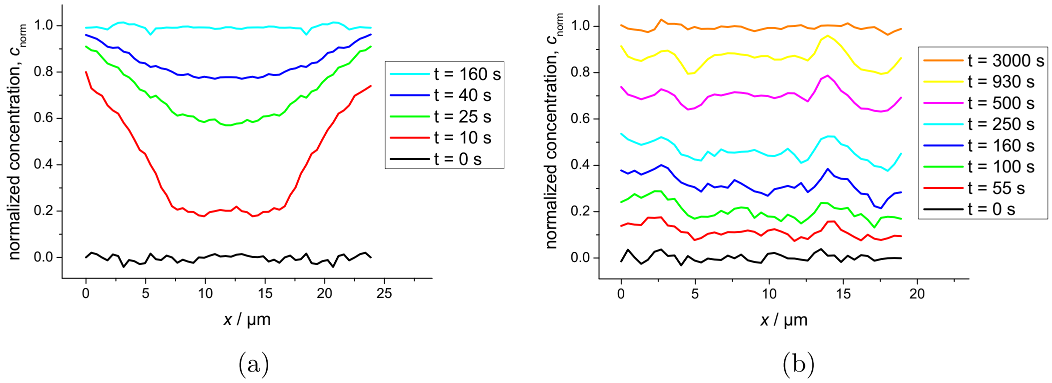

(a) (b)

Figure 45: Concentration profiles of isobutane (iC4) in silicalite-1. The adsorption experiments (following a pressure increase from 0 to 0.2 mbar) were performed only a few hours after activation (a) and several days later (b).

The discussion on the nature of the observed surface barriers in sec. 3.2 is correlated to the presence of impurities in the gas phase causing the formation of a surface layer, which acts as an additional transport resistance. To exclude that this effect results from impurities of the probe gas (here: isobutane), the following fig. 46 is presented: The time constants τ of isobutane adsorption is obtained from an exponential fit of the uptake curves. The increase of τ is larger after experiment 3, 5 and 7, where the probe rested, for several hours, under vacuum. When several adsorption-desorption cycles are performed (e.g. experiments 1, 2 and 3), there is almost no change in the uptake kinetics. Therefore, the probe gas is hindering, rather than enhancing the formation of this surface barrier.

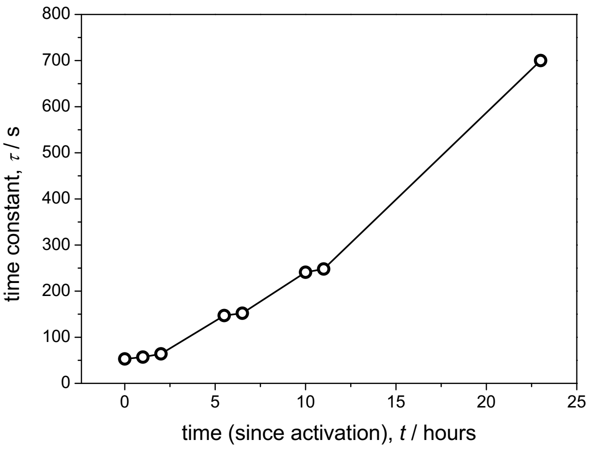

Figure 46: Time constants τ of several adsorption processes at different times t after activation.

A.3.3. Phase transition of benzene in silicalite-1

Tab. 4 in sec. 3.3 listed the refractive indices $n_\perp$ and $n_\parallel$ for a highly ordered benzene phase. These numbers were estimated by the Clausius-Mossotti relation, which correlates the microscopic, molecular polarizability α with the macroscopic permittivity ε:

$$\frac{\varepsilon_r - 1}{\varepsilon_r + 2} = \frac{N_A\,\varrho\,\alpha}{3\,M_m\,\varepsilon_0}, \tag{30}$$

where ε_r denotes the relative permittivity, $N_A = 6.0 \times 10^{23}\,\mathrm{mol}$ the Avogadro constant, $\varrho = 880\,\mathrm{kg\,m^{-3}}$ the mass density of benzene, α the molecular polarizability, $M_m = 78.1\,\mathrm{g\,mol^{-1}}$ the molar mass and $\varepsilon_0 = 8.85\,\mathrm{A\,s\,V^{-1}\,m^{-1}}$ the permittivity of a vacuum. Eq. (30) can be solved for ε_r, which allows the determination of $n_\perp$ and $n_\parallel$ from the literature values of $\alpha_\perp$ and $\alpha_\parallel$ [97]:

$$\varepsilon_r = n^2 = \frac{3\,N_A\,\varrho\,\alpha}{3M_m\,\varepsilon_0 - N_A\,\varrho\,\alpha}\ . \tag{31}$$

The large increase of the diffusivity of benzene in silicalite-1, as presented in fig. 21 on page 33, has also been confirmed by IRM measurements as shown in fig. 47.

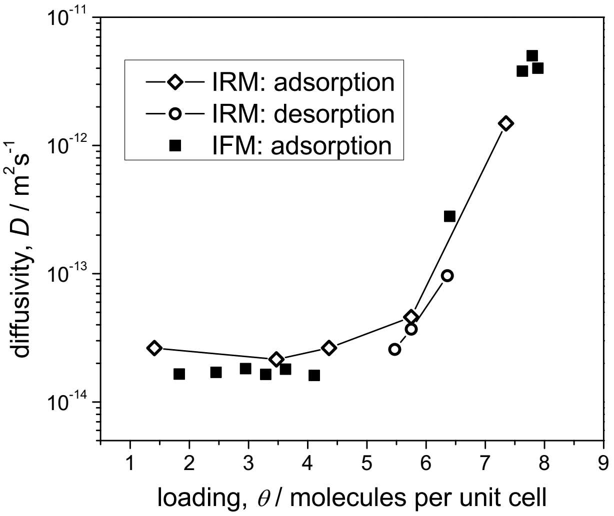

Figure 47: Diffusivities of benzene in silicalite-1 at different loadings obtained by interference microscopy (IFM, full symbols) and IR microscopy (IRM, open symbols).

A.4.1. Concentration profiles of cylindrical symmetry

Due to the hexagonal crystal shape, deviations from cylindrical symmetry for the concentration profiles in DDR zeolites were discussed in sec. 4.1.4. Fig. 48 shows the two-dimensional concentration maps of ethane in DDR-I at two different times, after the gas phase pressure was increased from 0 to 230 mbar. The diffusion front is of hexagonal shape at $t = 70$ s and of cylindrical shape at $t = 160$ s. This justifies the short-time approach (where the scenario is almost like diffusion into a semi-infinite medium) and the center-line analysis at intermediate times (assuming cylindrical symmetry).

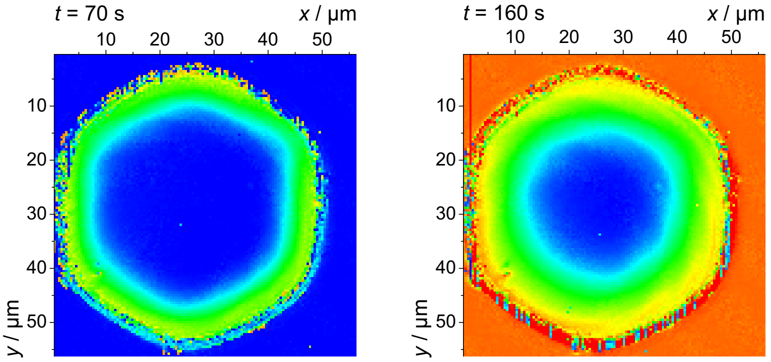

Figure 48: Two-dimensional concentration maps of ethane in DDR-I at different times t after the gas phase pressure was increased from 0 to 230 mbar. The background color has no physical meaning.

A.4.2. Comparison of different DDR zeolites

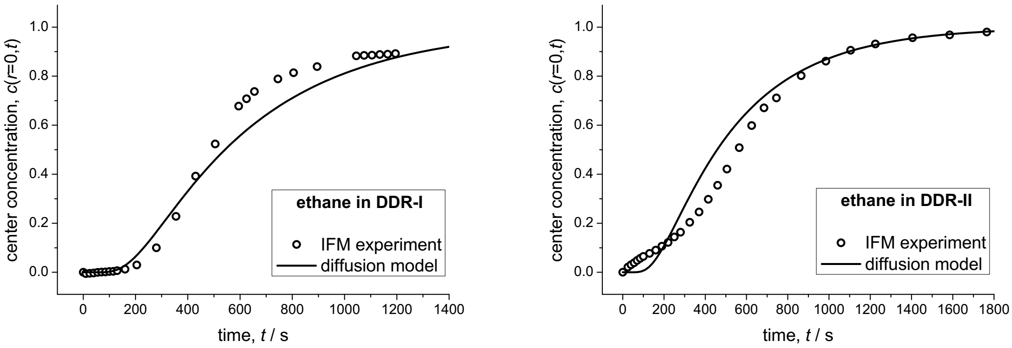

Figure 49: Increase of center concentration $c(r = 0, t)$ for ethane in DDR-I (left) and DDR-II (right) showing agreement at short times in the former system and notable deviation from ideal behavior in the latter case. The solid lines are obtained from the solution of the diffusion equation as given by eq. (14), using D and R from tabs. 5 and 6.

Differences of the three investigated samples of DDR zeolites were studied in sec. 4.2.1. Notable deviations were observed for the concentration in the crystal center, $c(r = 0, t)$, which is shown in fig. 49 for DDR-I and DDR-II. In an ideal crystal (no mass transport in axial direction), this center concentration is expected to be almost constant before the diffusion fronts meet. For DDR-II, this is clearly not the case: Already at short times there is a notable increase of $c(r = 0, t)$.

A.4.3. Binary mixtures in DDR zeolites

In sec. 4.3, investigations on binary mixtures in DDR zeolites were presented. For the experiments (2) and (3) of tab. 9, figs. 50 and 51 show the untreated IFM profiles, as well as the profiles and uptake curves after separation of the two components.

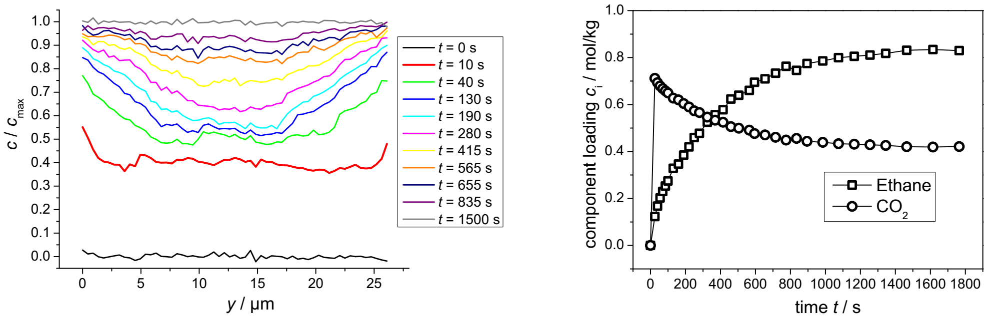

(a) untreated IFM profiles
(b) separated uptake curves

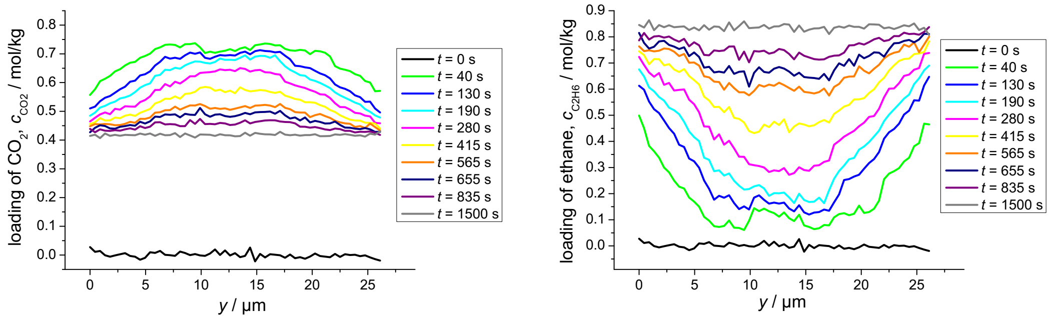

(c) separated profiles: CO_2
(d) separated profiles: ethane

Figure 50: Profiles of experiment (2), see tab. 9, before and after separation of the contributions of the two components to the IFM signal. The total pressure was about 600 mbar with a CO_2-to-ethane ratio of 2:1.

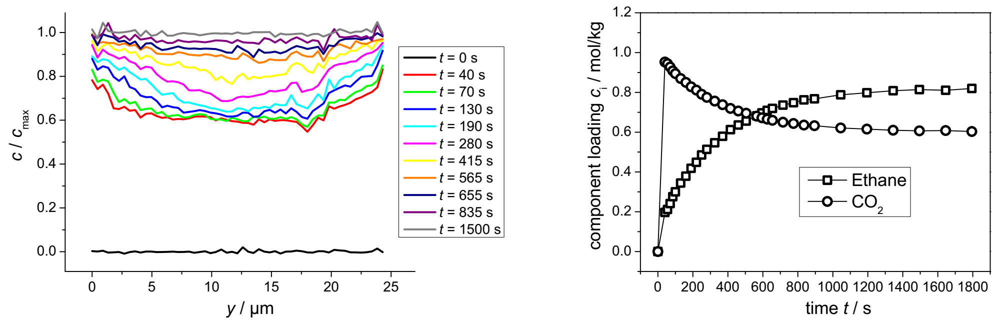

(a) untreated IFM profiles

(b) separated uptake curves

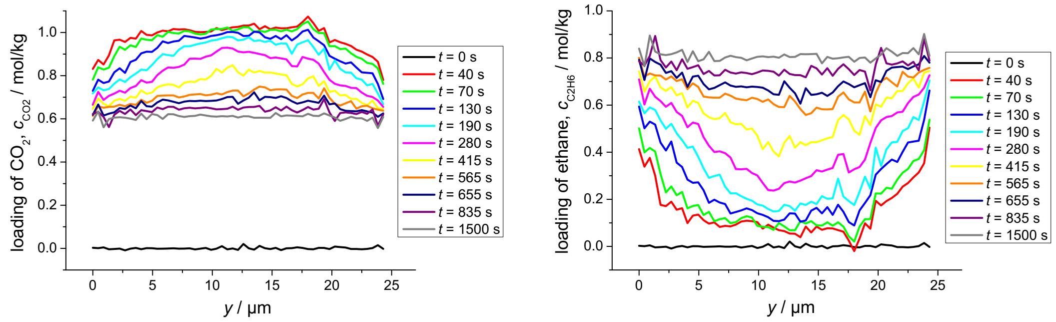

(c) separated profiles: CO_2

(d) separated profiles: ethane

Figure 51: Profiles of experiment (3), see tab. 9, before and after separation of the contributions of the two components to the IFM signal. The total pressure was about 800 mbar with a CO_2-to-ethane ratio of 3:1.

Publications

[Binder09] **T. Binder**, C. Chmelik, L. Heinke, F. Hibbe, J. Kärger, T. Titze and D. Tzoulaki. The Wealth of Information from Transient Guest Profiles. In *Diffusion Fundamentals III* (2009) pages 205–221. url:http://www.diffusion-fundamentals.org **11** (2009) 16.

[Binder11] **T. Binder**, Z. Adem, C. B. Krause, M. Krutyeva, A. Huang, J. Caro and J. Kärger. Surface permeability on zeolite NaCaA enhanced by layer deposition. *Microporous and Mesoporous Materials* **146** (2011) 151–157. doi:10.1016/j.micromeso.2011.04.037.

[Binder12] **T. Binder**, F. Hibbe, C. Chmelik, J. Kärger, A. Martinez-Joaristi, J. Gascon, F. Kapteijn and D. Ruthven. Micro-imaging of transient guest profiles in nanoporous host systems of cylindrical symmetry. *Journal of Chemical Physics* **137** (2012) 164704. doi:10.1063/1.4762849.

[Gueudré12] L. Gueudré, **T. Binder**, C. Chmelik, F. Hibbe, D. M. Ruthven and J. Kärger. Micro-Imaging by Interference Microscopy: A Case Study of Orientation-Dependent Guest Diffusion in MFI-Type Zeolite Host Crystals. *Materials* **5** (2012) 721–740. doi:10.3390/ma5040721.

[Binder13a] **T. Binder**, C. Chmelik, J. Kärger, A. Martinez-Joaristi, J. Gascon, F. Kapteijn and D. Ruthven. A Diffusion Study of Small Hydrocarbons in DDR Zeolites by Micro-Imaging. *Microporous and Mesoporous Materials* **accepted** (2013). doi:10.1016/j.micromeso.2013.06.038.

[Binder13b] **T. Binder**, C. Chmelik, J. Kärger and D. M. Ruthven. Micro-imaging of transient intracrystalline concentration profiles during two-component uptake of light hydrocarbon - carbon dioxide mixtures by DDR-type zeolites. *Ind. Eng. Chem. Res.* **submitted** (2013).

[Kärger13] J. Kärger, **T. Binder**, C. Chmelik, F. Hibbe, H. Krautscheid, R. Krishna and J. Weitkamp. Microimaging of Transient Guest Profiles in Nanoporous Materials. *Nature Materials* **submitted** (2013).

Within the chapters of this work, the author's publication are cited as [54], [75], [114], [60], [115], [123] and [99], following the chronological order of this list of publications.

Acknowledgment

It is my pleasure to thank all people who supported me during the last years and especially during the last months of preparing this thesis. I gratefully acknowledge the help of my Ph.D. supervisor Prof. Dr. Jörg Kärger for continuously encouraging and promoting me, which, certainly, was of most importance in times of difficulties. In particular, this includes issues beyond the scientific work.

I would like to cordially thank Dr. Christian Chmelik and Prof. Dr. Douglas M. Ruthven for numerous stimulating discussions, and inspiring and constructive input. Furthermore, I appreciate previous work on the experimental setup carried out by Ulf Schemmert, Pavel Kortunov and Despina Tzoulaki. I am much obliged for the cooperative and helpful working atmosphere in the group of Interface Physics and I would like to thank all current and former colleagues, especially Florian Hibbe, Tobias Titze and Alexander Lauerer from the shared office.

For the material synthesis and discussions on the experimental results, I am indebted to Prof. Dr. Freek Kapteijn, Dr. Alberto Martinez-Joaristi and to Dr. Wolfgang Schmidt. In addition, I would like to thank Prof. Dr. Harald Krautscheid and Dr. Florian Kettner for the XRD investigations on silicalite-1 framework changes.

Finally, I feel deeply grateful for the support of my friends, family and, in particular, my parents. As a most inspiring personality and character, I thank Jörg Schiffner, sensei, for teaching the principle of *Jita Kyouei* to young kids, teenagers and adults. For many truly amazing experiences and looking forward to many more adventures to come, I am in deep gratitude to *hurricane* Irene.

Erklärung zur Selbständigkeit

Hiermit erkläre ich, dass ich die vorliegende Arbeit selbständig und ohne unzulässige Hilfe oder Benutzung anderer als der angegebenen Hilfsmittel angefertigt habe. Ich versichere, dass Dritte von mir weder unmittelbar noch mittelbar geldwerte Leistungen für Arbeiten erhalten haben, die im Zusammenhang mit dem Inhalt der vorliegenden Dissertation stehen, und dass die vorgelegte Arbeit weder im Inland noch im Ausland in gleicher oder ähnlicher Form einer anderen Prüfungsbehörde zum Zwecke einer Dissertation oder eines anderen Prüfungsverfahrens vorgelegt und in ihrer Gesamtheit noch nicht veröffentlicht wurde. Alles aus anderen Quellen oder von anderen Personen übernommene Material, das in der Arbeit verwendet wurde oder auf das direkt Bezug genommen wird, wurde als solches kenntlich gemacht. Insbesondere wurden alle Personen genannt, die direkt an der Entstehung der vorliegenden Arbeit beteiligt waren.
Es haben keine erfolglosen Promotionsversuche stattgefunden.

Die Promotionsordnung der Fakultät für Physik und Geowissenschaften der Universität Leipzig, in der aktuell gültigen Version vom 03. März 2010, wird anerkannt.

Leipzig, den 03. 07. 2013

Tomas Binder